Studying ice particle growth processes in mixed-phase clouds using spectral polarimetric radar measurements

Pfitzenmaier, Lukas

DOI
10.4233/uuid:18c61a8d-2256-4b2d-878f-0406e272e982

Publication date
2018

Document Version
Final published version

Citation (APA)
Pfitzenmaier, L. (2018). *Studying ice particle growth processes in mixed-phase clouds using spectral polarimetric radar measurements.* [Dissertation (TU Delft), Delft University of Technology]. https://doi.org/10.4233/uuid:18c61a8d-2256-4b2d-878f-0406e272e982

STUDYING ICE PARTICLE GROWTH PROCESSES IN MIXED-PHASE CLOUDS USING SPECTRAL POLARIMETRIC RADAR MEASUREMENTS

STUDYING ICE PARTICLE GROWTH PROCESSES IN MIXED-PHASE CLOUDS USING SPECTRAL POLARIMETRIC RADAR MEASUREMENTS

Proefschrift

ter verkrijging van de graad van doctor
aan de Technische Universiteit Delft,
op gezag van de Rector Magnificus prof. dr. ir. T.H.J.J. van der Hagen,
voorzitter van het College voor Promoties,
in het openbaar te verdedigen op maandag 12 februari 2018 om 10:00 uur

door

Lukas PFITZENMAIER

Master of Scienc in Meteorology,
Universität Leipzig, Leipzig, Deutschland,
geboren in Stuttgart, Deutschland.

Dit proefschrift is goedgekeurd door de

promotor: Prof. Dr. ir. H.W.J. Russchenberg

Samenstelling promotiecommissie:

Rector Magnificus,	voorzitter
Prof. Dr. H.J.W. Russchenberg,	Technische Universiteit Delft
Onafhankelijke leden:	
Dr. U. Wandinger,	Leibniz Institute for Tropospheric Research, Leipzig, Germany
Prof. Dr. S. Crewell	University of Cologne, Cologne, Germany
Prof. Dr. P. Kollias	Stony Brook University, Stony Brook (NY), USA
Prof. Dr. A. P. Siebesma	Technische Universiteit Delft, Delft, The Netherlands
Prof. Dr. H. J. J. J. Jonker	Technische Universiteit Delft, Delft, The Netherlands
Overige leden:	
Dr. Y. Dufournet,	Sky-Echo, Rotterdam, The Netherlands

Dr. Yann Dufournet en Christine M. H. Unal hebben in belangrijke mate aan de totstandkoming van het proefschrift bijgedragen.

Keywords: cloud physics, spectral radar measurements, radar polarimetry, ice particle growth processes, mixed phase clouds

ISBN 978-94-6186-884-8
Dissertation at Delft University of Technology
Studying ice particle growth processes in mixed-phase clouds using spectral polarimetric radar measurements

An electronic version of this dissertation is available at
http://repository.tudelft.nl/.

CONTENTS

ABSTRACT

Clouds are a prominent part of the Earth hydrological cycle. In the mid-latitudes, the ice phase of clouds is highly involved in the formation of precipitation. The ice particles in the clouds fall to earth either as snow flakes, in the winter month, or melting crystals that become rain drops. An efficient growth process is the interaction of ice crystals and supercooled liquid water droplets in so called mixed-phase clouds. Mixed phase cloud systems contain both - ice crystals and super cooled cloud droplets - in the same volume of air. The interaction of ice and liquid phase leads to an enhanced growth of ice crystals and, therefore, enhances the amount of precipitation. However, such processes are still not fully understood. This work shows that such complex microphysical processes in mixed-phase clouds can be observed using state of the art ground based radar techniques. Analyzing spectral polarimetric radar data, different signatures of particle growth processes can be identified.

The results presented are based on measurements obtained with the Transportable Atmospheric Radar (TARA) during the ACCEPT campaign (Analysis of the Composition of Clouds with Extended Polarization Techniques), in autumn 2014, Cabauw, the Netherlands. TARA is an S-band radar profiler that has full Doppler and spectral polarimetric measurement capabilities. TARAs unique three-beam configuration is also able to retrieve the full 3-D velocity vector. Because the high temporal and spatial resolutions and its configurations TARA can capture the complexity of cloud dynamics and microphysical variabilities involved in mixed-phase cloud systems.

A new retrieval technique was applied to several case studies to qualitatively analyze ice particle growth processes within mixed phase cloud systems. These results demonstrate that using radar data re-arranged along fall streak, the interpretation of Doppler spectra and polarization parameters can improve. Based on synergetic measurements obtained during the ACCEPT campaign it was possible to detect possible to detect supercooled liquid water layers within the cloud system and relate them to TARA observations. Therefore, it was possible to even identify different growth processes, like particle riming, generation of the new particles, and particle diffusional growth within the TARA measurements. This demonstrates, that in order to observe ice particle growth processes within complex systems adequate radar technology and state of the art retrieval algorithms are required. Moreover, the ice particle growth processes within cloud systems can be linked directly to the increased rain intensities using along fall streak rearranged radar data.

The last objective of the thesis is the extension of the spectral polarimetric measurement capabilities of TARA and the estimate of the differential phase and the specific differential phase in the spectral domain. These two parameters are frequently used to improve rain estimation, hydrometeor classifications and, currently, more and more to improve microphysical process understanding, e.g. the onset of the aggregation of ice particles. So far, the parameters are used only as integrated moments. Nevertheless,

the work demonstrates that further work has to be done to completely understand the microphysical information of these spectral resolved parameters.

Overall, this work demonstrates that spectral polarimetric radar data can be used to improve the microphysical process understanding. The presented work also shows that spectral polarimetric radar data can be used to estimate quantitative microphysical properties related to ice particle growth.

SAMENVATTING

Wolken spelen een belangrijke rol in de hydrologische cyclus van de aarde. Voor de gematigde breedtegraden speelt de ijsfase in wolken een sleutelrol voor de vorming van neerslag. De ijsdeeltjes in de wolken vallen richting het aardoppervlak als sneeuw in de wintermaanden of smelten onderweg en vormen zo regendruppels. Een efficiënt en belangrijk onderliggend groeiproces in zogenaamde gemengde wolken is de interactie tussen ijskristallen en onderkoeld vloeibaar water. De interactie tussen ijs en de vloeibare fase leidt tot een vergrootte groeisnelheid van het ijskristal en vervolgens tot een toenemende hoeveelheid neerslag. Echter, de onderliggende processen worden niet volledig begrepen. Dit proefschrift toont aan dat, gebruikmakend van de nieuwste radartechnieken, deze complexe microfyische processen in de gemengde wolken kunnen worden geobserveerd: door het analyseren van spectraal-polarimetrische radardata kunnen verschillende ijskristallen worden geïdentificeerd. De resultaten gepresenteerd in dit werk zijn verkregen met de Transportable Atmospheric Radar (TARA) gedurende de periode van de ACCEPT campagne (Analysis of the Composition of Clouds with Extended Polarization Techniques), in de herfst van 2014, Cabauw, Nederland. TARA is een S-band radar die in staat is om volledige Doppler en polarimetrische metingen te doen. TARA's unieke drie-bundel configuratie biedt tevens de mogelijkheid om drie-dimensionale snelheidscomponenten te verkrijgen. Vanwege de hoge resolutie in zowel de tijd als de ruimte is het mogelijk om met TARA de complexiteit van de microfysische parameters van de gemengde wolken in kaart te brengen. De nieuwe techniek is toegepast onder verschillende scenario's om de deeltjesvorming in gemengde wolken kwantitatief te analyseren. De resultaten tonen aan dat het begrip van de microfysische processen verbeterd kan worden door gebruik te maken van Dopplerspectra en polarisatieparameters als deze gerangschikt zijn volgens de zgn valstrepen van neerslag uit de wolk. Het is mogelijk gebleken om lagen van onderkoeld vloeibaar water te detecteren door gebruik te maken van synergetische metingen die zijn gedaan met TARA tijdens de ACCEPT-campagne. De signatuur van het groeiproces in de radardata is gerelateerd en vergeleken met de aanwezigheid van onderkoeld vloeibaar water. Daarbij was het zelfs mogelijk om verschillende groeiprocessen te identificeren zoals riming, generatie van nieuwe deeltjes en diffusie. Tevens bleek het mogelijk de toename van de neerslagintensiteit direct te relateren aan de groei van de ijsdeeltjes. Het laatste doel van dit proefschrift is om de meetmogelijkheden van de TARA-radar uit te breiden en een afschatting te maken van de differentiële fase in het spectrale domein. Deze parameter wordt vaak gebruikt voor schattingen van de regenintensitieit, hydro-meteorologische classificaties te maken als ook voor het verbeteren van het begrip van de relevante microfysische processen. Samenvattend, dit proefschrift toont aan dat spectraal-polarimetrische radardata gebruikt kan worden om ons begrip van de microfysische processen in gemengde wolken te vergroten. Het herschikken van de spectrale data tegen de gemeten valstrepen verbetert de verkregen resultaten. Het werk laat tevens zien dat spectraal-polarimetrische radar data

kan worden gebruikt om een kwantitatieve schatting te doen van microfysische eigenschappen die betrekking hebben op de groei van ijsdeeltjes.

(Thanks to A. van Hooft for the translation)

1

INTRODUCTION

1.1. MOTIVATION

Clouds are one of the main components of the Earth's atmosphere and an essential part of the climate system. Covering up to 75% of the globe, clouds have a significant influence in the radiation budget of the Earth [1]. Having an albedo up to 80%, clouds scatter a large part of the solar radiation back into space [2]. The radiative impact of clouds is known to be one of the biggest uncertainties in climate prediction simulations [3]. One factor influencing the radiative transfer simulations is the variety of ice particle shapes that are present in clouds. Therefore, one way to reduce the uncertainties in the simulations is to improve the parameterizations of ice particle shapes [4]. Besides their effect on radiation clouds are responsible for a large part of the energy and water transport within the hydrological cycle [5, 6]. Clouds receive most of their moisture from the oceans and release it as liquid and solid precipitation over land. The analysis of longterm satellite and rain gauge observations reveals a mean annual precipitation rate of approximately 2.6 mm d^{-1} [7–9].

In the ice phase not only solid precipitation such as snow, graupel and hail is formed. The ice phase also initiates the formation of rain. Based on satellite data, Mülmenstädt *et al.* [10] could show that cold clouds are the major source for liquid precipitation over land. A detailed assessment for a mid-latitudes site in Germany showed that the ice phase was involved in the precipitation formation process up to 97 % [11]. Even though ice clouds have an important role in the atmospheric system, many processes related to ice clouds and the formation of precipitation are not yet fully understood. For example, the development of the various crystal shapes as a function of temperature and supersaturation is not yet fully understood [12]. While the primary shape of ice crystals follows a clear function of temperature and humidity in the temperature range from 0°C to −20°C for ice crystals formed at lower temperatures mixtures of crystal types occur [13]. The study by Mülmenstädt *et al.* [10] analyzing the contribution of ice, mixed-phase, and liquid clouds to the total precipitation amount using satellite observations. They found that in an observed column mixed phase clouds were involved in 30 − 50% of the precipitation formation process. Mixed phase clouds are cloud systems in which ice crystals

and supercooled liquid water droplets coexist in the same volume of air at temperatures below 0°C [6, 14]. However, there are also different definitions for mixed-phase clouds present in literature, e.g. de Boer *et al.* [15] used a definition, excluding frozen particles that precipitate out of regions where super cooled droplets were present. In this study such hydrometeors are included and a cloud system is defined as mixed phase if it contains super cooled liquid water droplets below 0°C or when it is above the melting layer, respectively.

The coexistence of ice crystals and supercooled liquid water droplets has often been observed by in situ measurements and remote sensing observations [15–20]. In situ observation also showed that super-cooled droplets coexistences with ice crystals is very thin layers as a result such areas called supercooled liquid layers [18, 30–32]. As illustrated in Figure 1.1, the interaction of ice crystals and the layer of supercooled liquid droplets leads to a faster and denser ice particle growth [21–25]. Because of this enhanced growth, the ice particles have the tendency to fall out faster as precipitation from the cloud compared to particle in a pure ice cloud [15, 26]. Also, precipitation produced by mixed-phase clouds leads to more intense precipitation compared to liquid or pure ice clouds [27–29]. In mixed-phase clouds, the ice particle growth is due to three processes.

- The *first* process is the diffusional growth of ice crystals. The process describes the phoneme that ice crystals growth by up-take of water molecules from the moist air.

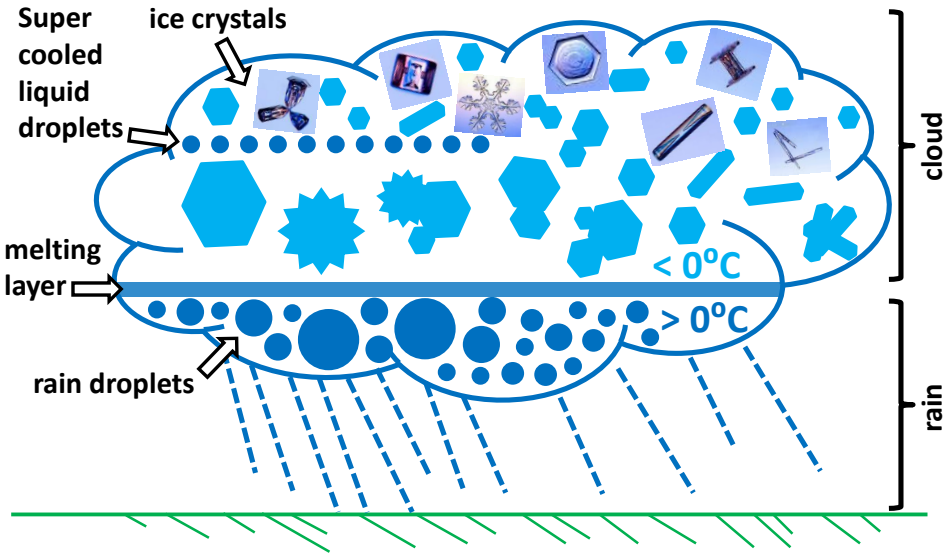

Figure 1.1: Sketch of a raining cloud system. On the upper left a mixed-phase cloud is shown (dark blue circles indicate a layer of supercooled liquid droplets). On the upper left the cloud contains no supercooled liquid in the cloud. When ice crystals fall through the layer of supercooled liquid they interact leading to a fast growth of the ice crystals (ice crystals are represented by the light blue symbols and photos). The larger ice crystals produce more rain after melting (rain indicated by dotted strips below the cloud).

Below 0°C, the water vapor saturation pressure of solid ice crystals is lower than the one of liquid water. In areas with supercooled liquid water presence ice crystal processes are most effective and termed Wegener-Bergeron-Findeisen process [22, 24]. Because of the difference in water vapor saturation pressure the ice crystals can grow very fast at the expense of supercooled liquid droplets which provide a continues and high supply of water molecules.

- The *second* process is the riming of ice crystals [14, 21, 25]. While falling through a layer of supercooled liquid water drops ice particles gain mass by collecting the supercooled droplets.

- The *third* process is the aggregation of ice crystals [6, 33]. This process describes the collision of ice crystals with each other. This process is the main growth process of ice crystals in pure ice clouds. Therefore, aggregation is also present under mixed-phase condition. Because of the involvement of the other two mentioned processes, the aggregation efficiency can be increase under mixed phase condition [34]

The spatial range of such microphysical processes is in the order of micrometers. Thus, this range is far below the grid size of weather prediction or climate models, and therefore, these processes have to be parametrized [23, 26, 35]. Especially their representation in climate modes needs improvements [36]. Therefore it is no surprise that the IPCC [37][1] reports a large uncertainty related to the representation of the ice phase in the models. As already mentioned one reason is the large variety in the size, shape and density of ice crystals in raining cloud systems. This is also sketched in Figure 1.1 where the large variation of pristine ice crystal types is illustrated by symbols and photographs of ice crystals near top of the cloud [13, 21]. Another reason is related to the growth processes of these ice crystals. These processes can differ depending on the involved pristine ice crystals and if they happen in cloud regions with supercooled liquid or not. The sketch illustrates the differences between a mixed phase cloud system including a layer of supercooled liquid droplets. Under mixed phase cloud conditions particles expected to grow to larger and denser ice particles as during ice conditions. Therefore, under mixed phase conditions the corresponding raindrops are bigger and the rain intensity is higher compared to a pure ice cloud [14]. The interaction processes between the liquid phase and the ice phase are characterized by a strong complexity and the small scales they are happening. Therefore, most weather or climate models parametrize the effect of these processes. They typically distinguish only a few hydrometeor classes, e.g. cloud ice, snow and perhaps graupel, and parametrize their interaction with only one moment of the particle size distribution, typically the mass mixing ratio.

Such parameterizations do not resolve single processes and take only one moment of the available particle habits into account ,e.g. particle size. Recently developed two moment schemes or full bin microphysical models still have large computational costs [38, 39].

[1] IPCC is the acronym for for Intergovernmental Panel on Climate Change

1

Observations are needed to improve the understanding of microphysical processes and model parameterizations related to ice particles. Nevertheless, such observations are still a challenge because of the variety of involved hydrometeors (size range and variety of shapes) and their differences in phases [6, 13, 14, 40]. Due to the high costs and safety problems because of potential icing of the air plane under mixed phase conditions in situ measurements of mixed-phase clouds are limited [18, 19]. To partly close the observational gap of microphysical cloud processes ground based remote sensing techniques show a large potential [23]. First, remote sensing techniques have strong potential because the temporal and spatial resolution of the instruments are high enough to measure the signatures of such processes. Second, the information content of the measured parameters can be increased using the synergy of different sensors. An example for such a combination of sensors is the detection of supercooled liquid water layers within cloud systems by a combination of radar[2] and lidar[3] measurements [15, 16]. With sadditional constraints by lidar, radar data can be analyzed more precisely. Another example is the combination of radar frequencies to retrieve ice particle size profiles [41]. However, by the use of instrumental synergy the differences between the measurement principles have to be taken into account which are the used frequencies/wavelength and resolutions of the instruments. Otherwise, the sensors might observe different cloud parts or hydrometeor sizes. This leads to differences in the observations which can cause large errors in the retrieval algorithms.

Nevertheless, the radar technique is unique in terms of cloud observations. Radars operating in the microwave part of the electromagnetic spectrum have the ability to penetrate optical thick cloud systems, even if they rain [42]. Radar measurements are used in multiple ways to study microphysical processes or retrieve microphysical properties. For this purpose measurements can be performed at different wavelength and scanning geometries. New approaches consider the use of polarimetric radar measurements, the combination of different radar frequencies, and the analysis of spectral radar data mainly from vertical pointing radar systems. Because, some polarimetric radar variables are elevation dependent they can only be obtained by scanning radar systems [43, 44]. Polarimetric radar variables[4] give information about the shape, the orientation, and the concentration if the measured hydrometeor have the same orientation. Such information can be used to estimate precipitation rates [45], classify hydrometeors types [46], or to find the dominate shapes of ice particle crystals in cirrus clouds [47]. The combination of different radar frequencies[5] is also used retrieve hydrometeor microphysical properties based on the differential attenuation of the hydrometeors that is different in the different radar frequencies [48]. A way to analyze changes of the hydrometeor size distribution present in the radar sampling volume are analyses of spectral radar data. The Doppler velocity corresponds to the reflectivity weighted mean fall velocity of the hydrometeors if no vertical air motion is present. Nowadays, radar are not only able to observe the mean Doppler velocity but also the full Doppler spectrum. Using the rela-

[2] RADAR is the acronym for Radio Detection And Ranging

[3] LIDAR is the acronym for Light Detection And Ranging

[4] Polarimetric radar variables are linear depolarization ratio, L_{DR}, differential reflectivity, Z_{DR} and specific differential phase shift K_{DP}

[5] Currently, the combination of 94 GHz, 35 GHz and 10 GHz is preferred, corresponding to W-, K_a-, and X-band domain

tion with fall velocity it is possible to separate modes in a Doppler spectrum and relate these to particle modes of particle size distribution that are measure [49]. Even higher moments of Doppler spectrum, e.g., Doppler spectrum skewness and kurtosis, are use to separate particle population from each other [50]. Currently, there is a trend to make use of the different measurement techniques in combination which is possible due to the larger availability and technical innovation of radar sensors in respect to spectral and polarimetric capabilities. Therefore, it is now possible, to extend our capabilities to retrieve microphysical processes and to analyze microphysical processes using radar remote sensing.

The following paragraph gives an overview on state-of-the-art radar techniques that allow an improved understanding of ice microphysical processes in clouds.

Myagkov *et al.* [51] retrieves the shape of pristine ice particles generated in liquid layer topped mixed phase clouds based on a combination of a vertical pointing and a RHI[6] scanning K_a-band radar. Combining the polarimetric measurements of the radar a quantitative estimation of ice particle shapes was done which are in agreement with the ice particle shapes found in the laboratory experiments. Stein *et al.* [41] retrieves the size of snow aggregates using simultaneous measurements of three radars operated at 3 GHz, 35 GHz, and 94 GHz. The method is based on the differences in backscattered power at each of the radar frequencies and physical modeling of different aggregation processes. The work of Kneifel *et al.* [52, 53] shows that radar triple-frequency measurements have the potential to separate snow particles. Recent results show that the observed clusters in the "triple frequency space" are closely connected to different snow crystal structures. Another way to analyze cloud microphysics is to analyze the measurements of the radar Doppler spectrum. The shape and the number of modes in the spectrum can be used to detect supercooled liquid water in the cloud system Luke *et al.* [31]. Their detection algorithm can detect the particle mode in the Doppler spectrum that is caused by supercooled liquid water droplets. The modes of the Doppler spectrum can also be used to identify ice particle growth. Kalesse *et al.* [25] studied Doppler spectra along a fall streak rearranged to analyze a riming case. Findings of her analysis are used to initialize a 1-D microphysical bin model. The model was able to simulate the riming process, however, more measurement information is needed to bring the results of the model closer to the data analysis. Oue *et al.* [54, 55] analyzed spectra of polarimetric radar measurements to study different ice particle shapes. Scattering calculations of polarimetric radar variables are used to validate the findings of the data analyses. Therefore, signatures of different ice particle shapes were identified in the measured spectra. Moisseev *et al.* [56] uses polarimetric measurements of a C-band radar and Doppler spectra measurements of a vertical pointing radar to study the onset of aggregation in winter storms. In a comparison with simulations they found that early stage aggregates have to be oblate and the number concentration higher than expected to produce the measured features. Grazioli *et al.* [57] studied also the growth of ice particles during snowfall events in the European Alps using an X-band radar. The identification of the different particle growth processes was based on a hydrometeor classification algorithm making use of polarimetric radar variables. A validation of that algorithm was performed with in situ observations. Dufournet and Russchenberg [58], Dufournet [59] explored the full capabilities of spectral

[6] RHI is the acronym for Range Hight Indication scans

radar measurements (Doppler and differential reflectivity spectra) to study ice microphysics using a profiling precipitation radar. The developed algorithm can classify the dominant ice crystal type in the measured cloud system above the melting layer.

The latter studies are the first attempts to exploit the unique capabilities of the TU Delft operated TARA[7] radar instrument which will be the main asset of this PhD study.

[7] TARA is the acronym for Transportable Atmospheric Radar

1.2. OVERVIEW OF THIS STUDY

The aim of this study is to improve the understanding of ice particle growth processes within mixed-phase clouds using spectral polarimetric radar observations. In that context, the study investigates four **key questions**:

I How can ice particle growth processes in mixed-phase cloud conditions be studied the best way using spectral polarimetric measurements of the TARA radar (S-band radar profiler)?

II Can the different ice particle growth processes be distinguished based on their signatures in the Doppler spectra and spectral polarimetric domain?

III Can particles that have grown under mixed phase conditions be related to an increase in the observed rain intensity?

IV Can the set of spectral polarimetric variables of the TARA radar be extended (processing of differential phase shift and specific differential phase shift in spectral domain) and which information can these parameters provide on ice particle microphysical processes?

The doctoral thesis is built around three *Publication manuscripts* (one published, one submitted to a journal and one in preparation) which are presented in the Chapters 2, 3 and 4, respectively. It has to be mentioned that the original manuscripts have not been modified, therefore, they can be read independently. The papers are structured in a way that they answer the **key questions** listed above. The structure of the thesis is described in more detail below.

Key question I is addressed in *Publication 1* (Chapter 2). In this Chapter, a retrieval technique to rearrange radar spectra along particle fall streaks is presented. Based on the rearranged spectral radar data, studying of microphysical processes of a single particle population can be performed from the cloud top towards the cloud bottom and the rain patterns.

Key questions II and **III** are addressed in *Publication 2* (Chapter 3). In this *Publication* spectral polarimetric radar data and moments rearranged along fall streaks are used to analyze ice particle growth within a precipitating cloud system. The application of the developed retrieval technique improves the quantitative analysis of radar measurements. The observed signatures from the TARA radar are compared against parallel measurements by a vertical pointing cloud radar and radiosonde profiles. Therefore, signatures of ice particle growth processes are identified and related to supercooled liquid layer presence in the cloud system. Based on the fall streak technique, the enhanced particle growth in mixed phase conditions could also be related to an increase in the rain patterns.

The context of **Key question IV** that is presented in Chapter 4, was developed during the data analysis of *Publication 2*. Former studies discussed the potential to combine Z_{DR} and K_{DP} to detect the onset of ice crystal aggregation in a cloud. This raises the question, if it is possible to observe such signatures in the spectral domain of these parameters, too. Because volume integrated radar variables are weighted towards large particles polarimetric signatures caused by small ice crystals are suppressed, for example,

at the onset of an aggregation process. To analyze these parameters in spectral domain would be a way to investigate that phenomenon and improve the process understanding, too. The *Manuscript of Publication 3* shows the first attempt of processing spectral differential phase and specific differential phase in and analyzes the observed spectral structures. An overall summary of the key findings is given in Conclusions and Outlook, Chapter 5. In the context of this Chapter, an outlook for future work concerning TARA as a sensor as well as using spectral polarimetric radar variables.

REFERENCES

[1] D. Wylie, D. L. Jackson, W. P. Menzel, and J. J. Bates, *Trends in Global Cloud Cover in Two Decades of HIRS Observations,* Journal of Climate **18**, 3021 (2005), http://dx.doi.org/10.1175/JCLI3461.1 .

[2] Y. Liu, W. Wu, M. P. Jensen, and T. Toto, *Relationship between cloud radiative forcing, cloud fraction and cloud albedo, and new surface-based approach for determining cloud albedo,* Atmospheric Chemistry and Physics **11**, 7155 (2011).

[3] S. Solomon, D. Qin, M. Manning, Z. Chen, M. Marquis, K. B. Averyt, M. Tignor, and H. L. Miller, eds., *Contribution of Working Group I to the Fourth Assessment Report of the Intergovernmental Panel on Climate Change* (Cambridge University Press, Cambridge, United Kingdom and New York, NY, USA, 2007).

[4] J. M. Comstock, R. D'Entremont, D. Deslover, G. G. Mace, S. Y. Matrosov, S. A. McFarlane, P. Minnis, D. Mitchell, K. Sassen, M. D. Shupe, D. D. Turner, and Z. Wang, *An Intercomparison of Microphysical Retrieval Algorithms for Upper-Tropospheric Ice Clouds,* Bulletin of the American Meteorological Society **88**, 191 (2007).

[5] M. T. Chahine, *The hydrological cycle and its influence on climate,* nature **359**, 373 (1992).

[6] H. R. Pruppacher and D. J. Klett, *Microphysics of Clouds and Precipitation* (Springer, 1996) p. 976.

[7] P. Xie and P. A. Arkin, *Global Precipitation: A 17-Year Monthly Analysis Based on Gauge Observations, Satellite Estimates, and Numerical Model Outputs,* Bulletin of the American Meteorological Society **78**, 2539 (1997), http://dx.doi.org/10.1175/1520-0477(1997)078<2539:GPAYMA>2.0.CO;2 .

[8] M. Chen, P. Xie, J. E. Janowiak, and P. A. Arkin, *Global land precipitation: A 50-yr monthly analysis based on gauge observations,* Journal of Hydrometeorology **3**, 249 (2002), http://dx.doi.org/10.1175/1525-7541(2002)003<0249:GLPAYM>2.0.CO;2 .

[9] R. F. Adler, G. J. Huffman, Chang, R. Alfred Ferraro, P.-P. Xie, J. Janowiak, B. Rudolf, U. Schneider, S. Curtis, D. Bolvin, A. Gruber, J. Susskind, P. Arkin, and E. Nelkin, *The version-2 global precipitation climatology project (gpcp) monthly precipitation analysis (1979–present),* Journal of Hydrometeorology **4**, 1147 (2003), http://dx.doi.org/10.1175/1525-7541(2003)004<1147:TVGPCP>2.0.CO;2 .

[10] J. Mülmenstädt, O. Sourdeval, J. Delanoë, and J. Quaas, *Frequency of occurrence of rain from liquid-, mixed-, and ice-phase clouds derived from A-Train satellite retrievals,* Geophysical Research Letters **42**, 6502 (2015).

[11] U. Löhnert, J. H. Schween, C. Acquistapace, K. Ebell, M. Maahn, M. Barrera-Verdejo, A. Hirsikko, B. Bohn, A. Knaps, E. O'Connor, C. Simmer, A. Wahner, and S. Crewell, *JOYCE: Jülich Observatory for Cloud Evolution,* Bulletin of the American Meteorological Society **96**, 1157 (2015), http://dx.doi.org/10.1175/BAMS-D-14-00105.1 .

[12] K. G. Libbrecht, *The physics of snow crystals,* Reports on Progress in Physics **68**, 855 (2005).

[13] M. P. Bailey and J. Hallett, *A Comprehensive Habit Diagram for Atmospheric Ice Crystals: Confirmation from the Laboratory, AIRS II, and Other Field Studies,* Journal of Atmospheric Sciences **66**, 2888 (2009).

[14] D. Lamb and J. Verlinde, *Physics and Chemistry of Clouds*, edited by geïllustreerd, 1 (Cambridge University Press, 2011) p. 600.

[15] G. de Boer, E. W. Eloranta, and M. D. Shupe, *Arctic Mixed-Phase Stratiform Cloud Properties from Multiple Years of Surface-Based Measurements at Two High-Latitude Locations,* Journal of Atmospheric Sciences **66**, 2874 (2009).

[16] K. Sassen, *Deep Orographic Cloud Structure and Composition Derived from Comprehensive Remote Sensing Measurements.* Journal of Applied Meteorology **23**, 568 (1984).

[17] R. M. Rauber, *Characteristics of Cloud Ice and Precipitation during Wintertime Storms over the Mountains of Northern Colorado.* Journal of Applied Meteorology **26**, 488 (1987).

[18] R. J. Hogan, P. R. Field, A. J. Illingworth, R. J. Cotton, and T. W. Choularton, *Properties of embedded convection in warm-frontal mixed-phase cloud from aircraft and polarimetric radar,* Quarterly Journal of the Royal Meteorological Society **128**, 451 (2002).

[19] P. R. Field, R. J. Hogan, P. R. A. Brown, A. J. Illingworth, T. W. Choularton, P. H. Kaye, E. Hirst, and R. Greenaway, *Simultaneous radar and aircraft observations of mixed-phase cloud at the 100 m scale,* Quarterly Journal of the Royal Meteorological Society **130**, 1877 (2004).

[20] M. D. Shupe, *Clouds at Arctic Atmospheric Observatories. Part II: Thermodynamic Phase Characteristics,* Journal of Applied Meteorology and Climatology **50**, 645 (2011), http://dx.doi.org/10.1175/2010JAMC2468.1 .

[21] N. Fukuta and T. Takahashi, *The Growth of Atmospheric Ice Crystals: A Summary of Findings in Vertical Supercooled Cloud Tunnel Studies.* Journal of Atmospheric Sciences **56**, 1963 (1999).

[22] A. Korolev, *Limitations of the Wegener Bergeron Findeisen Mechanism in the Evolution of Mixed-Phase Clouds,* Journal of Atmospheric Sciences **64**, 3372 (2007).

[23] M. D. Shupe, J. S. Daniel, G. de Boer, E. W. Eloranta, P. Kollias, C. N. Long, E. P. Luke, D. D. Turner, and J. Verlinde, *A Focus On Mixed-Phase Clouds,* Bulletin of the American Meteorological Society **89**, 1549 (2008).

[24] W. Findeisen, E. Volken, A. M. Giesche, and S. Brönnimann, *Colloidal meteorological processes in the formation of precipitation,* Meteorologische Zeitschrift **24**, 443 (2015).

[25] H. Kalesse, W. Szyrmer, S. Kneifel, P. Kollias, and E. Luke, *Fingerprints of a riming event on cloud radar doppler spectra: observations and modeling,* Atmospheric Chemistry and Physics **16**, 2997 (2016).

[26] J. Fan, S. Ghan, M. Ovchinnikov, X. Liu, P. J. Rasch, and A. Korolev, *Representation of Arctic mixed-phase clouds and the Wegener-Bergeron-Findeisen process in climate models: Perspectives from a cloud-resolving study,* Journal of Geophysical Research (Atmospheres) **116**, D00T07 (2011).

[27] F. Niu and Z. Li, *Systematic variations of cloud top temperature and precipitation rate with aerosols over the global tropics,* Atmospheric Chemistry and Physics **12**, 8491 (2012).

[28] S. E. Yuter and R. A. Houze, *Microphysical modes of precipitation growth determined by S-band vertically pointing radar in orographic precipitation during MAP,* Quarterly Journal of the Royal Meteorological Society **129**, 455 (2003).

[29] M. R. Kumjian, S. A. Rutledge, R. M. Rasmussen, P. C. Kennedy, and M. Dixon, *High-Resolution Polarimetric Radar Observations of Snow-Generating Cells,* Journal of Applied Meteorology and Climatology **53**, 1636 (2014).

[30] A. V. Korolev, G. A. Isaac, S. G. Cober, J. W. Strapp, and J. Hallett, *Microphysical characterization of mixed-phase clouds,* Quarterly Journal of the Royal Meteorological Society **129**, 39 (2003).

[31] E. P. Luke, P. Kollias, and M. D. Shupe, *Detection of supercooled liquid in mixed-phase clouds using radar Doppler spectra,* Journal of Geophysical Research (Atmospheres) **115**, D19201 (2010).

[32] H. Kalesse, G. de Boer, A. Solomon, M. Oue, M. Ahlgrimm, D. Zhang, M. D. Shupe, E. Luke, and A. Protat, *Understanding Rapid Changes in Phase Partitioning between Cloud Liquid and Ice in Stratiform Mixed-Phase Clouds: An Arctic Case Study,* Monthly Weather Review **144**, 4805 (2016).

[33] C. D. Westbrook, R. J. Hogan, A. J. Illingworth, and E. J. O'Connor, *Theory and observations of ice particle evolution in cirrus using Doppler radar: Evidence for aggregation,* grl **34**, L02824 (2007), physics/0608144 .

[34] P. V. Hobbs, S. Chang, and J. D. Locatelli, *The dimensions and aggregation of ice crystals in natural clouds,* jgr **79**, 2199 (1974).

[35] G. Thompson, R. M. Rasmussen, and K. Manning, *Explicit Forecasts of Winter Precipitation Using an Improved Bulk Microphysics Scheme. Part I: Description and Sensitivity Analysis,* Monthly Weather Review **132**, 519 (2004).

[36] J.-L. Li, D. E. Waliser, J. H. Jiang, D. L. Wu, W. Read, J. W. Waters, A. M. Tompkins, L. J. Donner, J.-D. Chern, W.-K. Tao, R. Atlas, Y. Gu, K. N. Liou, A. Del Genio, M. Khairoutdinov, and A. Gettelman, *Comparisons of EOS MLS cloud ice measurements with ECMWF analyses and GCM simulations: Initial results,* grl **32**, L18710 (2005).

[37] IPCC, *Index,* in *Climate Change 2013: The Physical Science Basis. Contribution of Working Group I to the Fifth Assessment Report of the Intergovernmental Panel on Climate Change*, edited by T. Stocker, D. Qin, G.-K. Plattner, M. Tignor, S. Allen, J. Boschung, A. Nauels, Y. Xia, V. Bex, and P. Midgley (Cambridge University Press, Cambridge, United Kingdom and New York, NY, USA, 2013) Book section Index, p. 1523–1535.

[38] B. H. Lynn, A. P. Khain, J. Dudhia, D. Rosenfeld, A. Pokrovsky, and A. Seifert, *Spectral (Bin) Microphysics Coupled with a Mesoscale Model (MM5). Part I: Model Description and First Results,* Monthly Weather Review **133**, 44 (2005).

[39] A. Seifert and K. D. Beheng, *A two-moment cloud microphysics parameterization for mixed-phase clouds. Part 2: Maritime vs. continental deep convective storms,* Meteorology and Atmospheric Physics **92**, 67 (2006).

[40] N. L. Miles, J. Verlinde, and E. E. Clothiaux, *Cloud droplet size distributions in low-level stratiform clouds,* Journal of Atmospheric Sciences **57**, 295 (2000).

[41] T. H. M. Stein, C. D. Westbrook, and J. C. Nicol, *Fractal geometry of aggregate snowflakes revealed by triple-wavelength radar measurements,* grl **42**, 176 (2015).

[42] P. Kollias, E. E. Clothiaux, M. A. Miller, B. A. Albrecht, G. L. Stephens, and T. P. Ackerman, *Millimeter-Wavelength Radars: New Frontier in Atmospheric Cloud and Precipitation Research,* Bulletin of the American Meteorological Society **88**, 1608 (2007).

[43] S. Y. Matrosov, *Theoretical Study of Radar Polarization Parameters Obtained from Cirrus Clouds.* Journal of Atmospheric Sciences **48**, 1062 (1991).

[44] R. F. Reinking, S. Y. Matrosov, R. A. Kropfli, and B. W. Bartram, *Evaluation of a 45*deg *Slant Quasi-Linear Radar Polarization State for Distinguishing Drizzle Droplets, Pristine Ice Crystals, and Less Regular Ice Particles,* Journal of Atmospheric and Oceanic Technology **19**, 296 (2002).

[45] V. N. Bringi and V. Chandrasekar, *Polarimetric Doppler Weather Radar, by V. N. Bringi and V. Chandrasekar, pp. 662. ISBN 0521623847. Cambridge, UK: Cambridge University Press, October 2001.* (2001) p. 662.

[46] J. M. Straka, D. S. Zrnic, and A. V. Ryzhkov, *Bulk Hydrometeor Classification and Quantification Using Polarimetric Radar Data: Synthesis of Relations.* Journal of Applied Meteorology **39**, 1341 (2000).

[47] S. Y. Matrosov, R. F. Reinking, R. A. Kropfli, B. E. Martner, and B. W. Bartram, *On the Use of Radar Depolarization Ratios for Estimating Shapes of Ice Hydrometeors in Winter Clouds.* Journal of Applied Meteorology **40**, 479 (2001).

[48] S. Kneifel, M. S. Kulie, and R. Bennartz, *A triple-frequency approach to retrieve microphysical snowfall parameters,* Journal of Geophysical Research (Atmospheres) **116**, D11203 (2011).

[49] P. Kollias, J. RéMillard, E. Luke, and W. Szyrmer, *Cloud radar Doppler spectra in drizzling stratiform clouds: 1. Forward modeling and remote sensing applications,* Journal of Geophysical Research (Atmospheres) **116**, D13201 (2011).

[50] C. Acquistapace, S. Kneifel, U. Löhnert, P. Kollias, M. Maahn, and M. Bauer-Pfundstein, *Optimizing observations of drizzle onset with millimeter-wavelength radars,* Atmospheric Measurement Techniques Discussions **2016**, 1 (2016).

[51] A. Myagkov, P. Seifert, U. Wandinger, J. Bühl, and R. Engelmann, *Relationship between temperature and apparent shape of pristine ice crystals derived from polarimetric cloud radar observations during the ACCEPT campaign,* Atmospheric Measurement Techniques **9**, 3739 (2016).

[52] S. Kneifel, A. Lerber, J. Tiira, D. Moisseev, P. Kollias, and J. Leinonen, *Observed relations between snowfall microphysics and triple-frequency radar measurements,* Journal of Geophysical Research (Atmospheres) **120**, 6034 (2015).

[53] S. Kneifel, P. Kollias, A. Battaglia, J. Leinonen, M. Maahn, H. Kalesse, and F. Tridon, *First observations of triple-frequency radar Doppler spectra in snowfall: Interpretation and applications,* grl **43**, 2225 (2016).

[54] M. Oue, M. R. Kumjian, Y. Lu, J. Verlinde, K. Aydin, and E. E. Clothiaux, *Linear Depolarization Ratios of Columnar Ice Crystals in a Deep Precipitating System over the Arctic Observed by Zenith-Pointing Ka-Band Doppler Radar,* Journal of Applied Meteorology and Climatology **54**, 1060 (2015).

[55] M. Oue, M. R. Kumjian, Y. Lu, Z. Jiang, E. E. Clothiaux, J. Verlinde, and K. Aydin, *X-Band Polarimetric and Ka-Band Doppler Spectral Radar Observations of a Graupel-Producing Arctic Mixed-Phase Cloud,* Journal of Applied Meteorology and Climatology **54**, 1335 (2015).

[56] D. N. Moisseev, S. Lautaportti, J. Tyynela, and S. Lim, *Dual-polarization radar signatures in snowstorms: Role of snowflake aggregation,* Journal of Geophysical Research (Atmospheres) **120**, 12 (2015).

[57] J. Grazioli, G. Lloyd, L. Panziera, C. R. Hoyle, P. J. Connolly, J. Henneberger, and A. Berne, *Polarimetric radar and in situ observations of riming and snowfall microphysics during CLACE 2014,* Atmospheric Chemistry & Physics **15**, 13787 (2015).

[58] Y. Dufournet and H. W. J. Russchenberg, *Towards the improvement of cloud microphysical retrievals using simultaneous Doppler and polarimetric radar measurements,* Atmospheric Measurement Techniques **4**, 2163 (2011).

[59] Y. Dufournet, *Ice crystal properties retrieval ususing radar spectral polarimetric measurements within ice – mixed-phase clouds*, Ph.D. thesis, Technische Universiteit Delft (2010).

2

Retrieving Fall Streaks within Cloud Systems using Doppler Radar

Abstract: Interaction of the ice crystals with super-cooled liquid droplets in mixed-phase clouds leads to an enhanced growth of the ice particles. However, such processes are still not clearly understood although they are important processes for precipitation formation in mid-latitudes. To better understand how ice particles grow within such clouds, changes of microphysical parameters of a particle population falling through the cloud have to be analyzed. The Transportable Atmospheric Radar (TARA) can retrieve the full 3-D Doppler velocity vector based on a unique three-beam configuration. Using the derived wind information, a new fall streak retrieval technique is proposed so that microphysical changes along those streaks can be studied. The method is based on Doppler measurements only. The shown examples measured during the ACCEPT campaign (Analysis of the Composition of Clouds with Extended Polarization Techniques) demonstrate that the retrieval is able to capture the fall streaks within different cloud systems. These fall streaks can be used to study changes in a single particle population from its generation (at cloud top) till its disintegration. In this study fall streaks are analyzed using radar moments or Doppler spectra. Synergetic measurements with other instruments during ACCEPT allow the detection of liquid layers within the clouds. The estimated microphysical information is used here to get a better understanding of the influence of super-cooled liquid layers on ice crystal growth. This technique offers a new perspective for cloud microphysical studies.

2.1. INTRODUCTION

Measuring clouds to understand the involved ice particle growth processes [1, 2] is still a challenge because of the small temporal and spatial scales involved. Ground-based radar measurements are widely used for such observations [1, 3]. Nowadays their advanced capabilities make the observation and study of microphysical processes within cloud and precipitation systems possible.

One approach improving the understanding of cloud particle growth processes is following a population of particles from their generation through their different stages of development till they evaporate or fall as precipitation on the ground [4].

This can be done by tracking fall streak structures within radar measurements [2, 5, 6]. Yuter and Houze [6] defined a fall streak signature as a manifestation of an inhomogeneity in the microphysical structure of a cloud system. To be observed, the relative size and number of precipitation particles within the fall streak need to be sufficient such that their radar reflectivity stands out as a local maximum from the immediate background reflectivities. Such fall streak structures are visible in radar reflectivity range height indicator scans (RHI) or time-height plots, when the thermodynamical conditions in so-called generating cells lead to a continuous and homogeneous production of particles [4, 7]. Figure 2.1 depicts such a fall streak structure (dark blue area from top to bottom), with the particles being generated near cloud top [8, 9].

Following the generating level concept, Marshall [8] and Browne [10] were the first to analyze and later retrieve the shape and structure of a fall streak within radar measurements; that is similar to the one featured in Figure 2.1 a). By varying the input parameters of the fall streak calculation, some analysis of the particle population was also performed. Marshall [8] related the broadening in fall streaks to the size sorting of the crystals depending on some size-fall speed relationships. The width of fall streak was then correlated to the size range of the particle size distribution of the analyzed particle population. Independent from Marshall [8] the same microphysical relations were found by Browne [10]. The predominant influence on the fall streak shape was found to be the horizontal wind structure within the cloud system [5, 8]. This was shown by Marshall and Gunn [5] where they demonstrated that slope changes in fall streaks are related to changes in the horizontal wind field within the cloud system.

To be able to analyze particle growth processes using fall streak signatures some assumptions have to be made. First of all, it is assumed that particles generate continuously and homogeneously within the generating cell. Second, the dynamical and microphysical conditions of the cloud system are homogeneous and stable over time. In such a way, it is possible to translate fall streak signatures based on Eulerian observations provided by the 2D time plot of the radar, to Lagrangian based 'pseudo' particle trajectory. Figure 2.1 a) shows the same fall streak signature at two different times obtained by profiling radars, located in the line of wind direction with known distance Δx_{radars}. Because dynamical and microphysical properties of the cloud system are constant during the analysis, the visible structure remains the same in these cases. Therefore, it is possible to retrieve the trajectory of the particle population A (dashed black line). Falling through the cloud system, the particles are displaced according to the shear in horizontal wind fields (indicated with red arrows). The horizontal wind shear also causes the slope of the fall streak patterns. If no wind shear within the system is present the fall streaks follow a

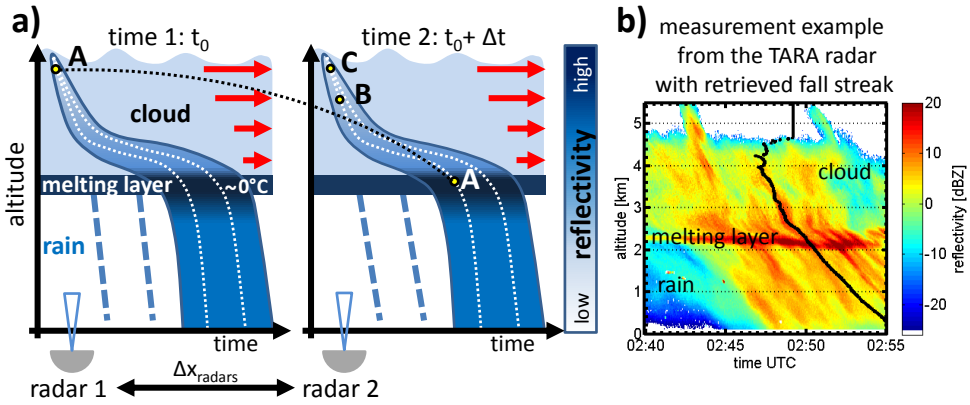

Figure 2.1: a) theoretical sketch of radar reflectivity time-height plots of observed fall streak signatures within a precipitating cloud system. The sketch shows observations taken by two different profiling radars (radar 1 and 2) that are measured at different places (distance Δx_{radar} along the wind direction). Due to the assumption of a horizontal cloud both radars observe similar structures. The red arrows indicate the strength of the horizontal wind field (horizontal wind shear). A, B, and C represent different particle populations. Due to the assumed homogeneity in the cloud, fall streaks represent the microphysical evolution of particle populations. The presented algorithm retrieves fall streaks following the microphysical processes evolution of the particle population indicated by the white dotted lines. The trajectory of the particle population A (black dotted line) can be indicated, knowing the wind fields and distance between the radars. b) shows an example reflectivity time height plot of observed fall streak signatures with the TARA radar during the ACCEPT campaign on the 16^{th} October 2014. The black line shows an example of a retrieved fall streak compatible to the white dotted lines.

straight vertical line from cloud top to bottom. Then also no broadening of the fall streak is visible. The broadening is caused by size sorting of the particles due to their individual fall speeds while falling through the cloud and adapting to the changes of the dynamical conditions [5]. Further, we want to point out that for the same assumed wind shear the visible fall streak slopes in RHI scans are reversed compared to the ones in Figure 2.1, see Mittermaier *et al.* [11] Figure 1. If a constant generation cell at cloud top is assumed, analyses of microphysical changes of the same particle population are possible by examining the different features of the fall streak signatures [8, 10].

Marshall and Gunn [5] linked the fall streak in clouds to observed microphysical changes in precipitation pattern. This was the first attempt to correlate precipitation patterns with the ice particle growth found in the cloud aloft. This approach was followed by Yuter and Houze [6] and Mittermaier *et al.* [11] to link precipitation pattern to the particle formation processes aloft. Mittermaier *et al.* [11] used the fall streak structures to improve the forecast of precipitation patterns at the ground. This was also considered for improving the validation of the rain estimates with rain gauges at ground level so that the fit between precipitation peaks in the radar data and rain gauges can be enhanced. Other microphysical studies have been performed where different particle populations and their different microphysical processes were tracked along the streak. Yuter and Houze [6] focused on the link of particle formation and resulting rain intensity, while Kalesse *et al.* [2] focused on riming processes within winter precipitation. Observation results of both studies were compared to 1D column models to see if the models

are able to reproduce the observations. In both cases, the models were able to reproduce the processes, although Kalesse *et al.* [2] stressed that more observations are needed to minimize the initialization settings of the model. The fall streak concept was also used to create inhomogeneity in modeled cirrus cloud field, Hogan and Kew [12]. This was done to find out what influence those inhomogeneities in clouds have on radiative transfer simulations. The result is that 3D effects can significantly affect the radiation budget and within global climate models a parametrization adjustment might be useful. All these papers point out the potential and the possibilities of using fall streaks for further microphysical analysis. It is, however, worth stressing out that all applications rely on additional wind information, a chosen relation between particle size and fall velocity, and an assumption on the generation level height. Because of a lack of horizontal wind field information, analysis of fall streaks is limited to situations where dynamical conditions are simple and stable over time [2, 5, 8].

In this paper, a novel definition of fall streaks based on particle dynamic rather than on microphysical contrast is used. The shape of the fall streak is, indeed, mainly influenced by the cloud dynamic, that does not necessarily have to follow an enhanced or outstanding reflectivity pattern (i.e. homogeneous cloud conditions). To represent fall streaks for different cloud situations, we base our definition on the path of a particle population obtained from the observation of its own motion. If the exact cloud dynamic is known, it is possible to retrieve fall streaks according to the individual particle motions for each time step of the radar measurement, as seen by the white dotted lines in Figure 2.1 a). Note that because of this definition features like the width of the fall streak patterns cannot be taken into account. Following the concept based on individual particle motions, the definition aims at the microphysical process understanding of the tracked particle population falling through the cloud system rather than analyzing the size sorting of the near cloud top generated particles.

In this paper, we introduce an automatic fall streak retrieval based on single Doppler measurements, taken with the TU Delft operated Transportable Atmospheric RAdar (TARA). From this radar, the full 3D wind vector per sampling volume can be retrieved, thanks to its three-beam configuration [13]. Furthermore, the high resolution of 3D wind information provided by TARA makes it possible to retrieve fall streaks at high temporal resolution, offering more insights on the growth processes occurring in complex, local and inhomogeneous cloud conditions. A better representation of the diversity of the fall streaks within a selected time frame is, in this way, achieved. Finally, fall streaks are retrieved based on measurements of a single instrument so that fewer assumptions for the algorithm, compared to previous techniques, are required. After introducing the data and the radar system in Section 2.2, the paper gives an overview of the proposed retrieval technique in Section 2.3. The limitations and requirements of the retrieval are discussed in Section 2.4, and Section 2.5 shows preliminary retrieval results.

2.2. DATA SET AND INSTRUMENT

2.2.1. TARA AND ACCEPT CAMPAIGN DATA SET

Results and retrieval developments are based on measurements performed with the TARA radar [14]. TARA is a frequency modulated continuous wave (FM-CW) S-band radar pro-

filer that has Doppler and fully polarimetric capabilities.

Table 2.1: Specifications of TARA during the ACCEPT campaign. HH = horizontal transmit and horizontal receive. VV = vertical transmit and vertical receive. HV = vertical transmit and horizontal receive.

Radar		
Type	FM-CW	
Central frequency	3.298 GHz	S-band
Transmitted power	100 W	Automatic decrease by step of 10 dB in case of receiver saturation (moderate to extrem precipitation)
Signal generation		
Sweep time	0.5 ms	
No. of range bins	512	
Range resolution	30 m	Height resolution is 21.2 m
Time resolution	2.56 s	
Polarimetry		
Polarisation	VV HV HH	Main beam only (single receiver channel)
Measurement cycle	VV HV HH OB1 OB2	Main beam + 2 offset beams
Doppler		
No. Doppler bins	512	
Doppler resolution	0.036 $m\,s^{-1}$	
Max. unambiguous velocity	$\pm 9.1\ m\,s^{-1}$	
Max. velocity main beam	$\pm 45.5\ m\,s^{-1}$	After spectral polarimetric dealiasing [15]
Max. velocity offset beams	$\pm 45.5\ m\,s^{-1}$	After spectral dealiasing
Antennas		
Beam width	2.1°	
Gain	38.8 dB	
Near field	≤ 200 m	
Beams	Elevation	Azimuth related to the North
Main beam	45°	246.5°
Offset beam 1	60°	246.5°
Offset beam 2	43.1°	267.3°
Clutter suppression		
Hardware	Antennas	Low side lobes
Processing	Doppler spectrum	Spectral polarimetry (main beam)

Data measured during the ACCEPT campaign (Analysis of the Composition of Clouds with Extended Polarization Techniques) is used to illustrate the fall streak algorithm. The measurements were performed from October to November 2014 at the Cabauw Experimental Site for Atmospheric Research (CESAR), the Netherlands. The TARA radar was measuring collocated with an extended setup of the Leipzig Aerosol and Cloud Remote Observation System (LACROS) [16]. The aim of ACCEPT is to understand the microphysical processes involved in mixed phase clouds at high resolution. One focus is to improve the understanding of ice crystal formation at the top of single layer mixed-phase clouds [17]. A second focus is to improve the understanding of ice particle growth when ice crystals fall through such liquid layers embedded within the cloud systems.

To observe the variety in size, shape, and the different phases of the involved hydrometeors a synergy of instruments was used. The TARA radar measured in parallel with the vertically pointing Ka-band cloud radar Mira [18] to obtain ice crystal information within the cloud being probed. Adding a high-frequency radar (Mira, 35.5 GHz) is particularly useful to detect small ice crystals near the cloud top. To retrieve liquid layer signatures within clouds [19], collocated measurements from the portable aerosol Raman Lidar (Polly^{XT}; [20]) were used. The method is based on a threshold for the depolarization ratio and the backscatter coefficient. Liquid layers are assumed to be composed of densely populated small spherical liquid water droplets. In that case, the depolarization ratio is close to zero, and the backscattering coefficient is large.

2.2.2. USE OF TARA AS WIND PROFILER: THE WIND RETRIEVAL

The 3D wind field can be retrieved because of the unique three-beam configuration of the TARA radar [13]. Using the Doppler spectra information of the three beams, main beam, and two offset beams, the horizontal wind velocity vd_h, the vertical Doppler velocity vd_V, and the wind direction ϕ_W can be retrieved with a minimal temporal resolution of 2.56 s. Table 4.1 lists more technical details about the specifications of the TARA radar during ACCEPT campaign.

2.3. THE FALL STREAK RETRIEVAL TECHNIQUE

The aim of the algorithm is to retrieve and analyze the microphysical evolution along fall streaks of a particle population from the particle generation till they reach the bottom of the cloud system.

In comparison with the common definition of fall streaks based on microphysical contrast, it can be seen that the fall streaks retrieved with the new method follow in some cases the enhanced reflectivity filaments (0249 and 0250 at 3 km in Figure 2.1 b)). Consistency is therefore found between the two definitions when reflectivity contrast is observed.

As previously mentioned, the retrieval is based on the directly measured 3D wind information (vertical Doppler velocity vd_V, horizontal wind velocity vd_h, and wind direction ϕ_W) obtained with the TARA radar. From a starting time t_0 (Figure 2.2), the goal is to estimate the number of time bins needed (subtracted or added) to reconstruct the fall streak from a bottom-up approach. Figure 2.3 shows the flow chart of the fall streak retrieval algorithm. The time displacement at the height z is given in Equation 2.1. It

consists of two terms:

$$\Delta t(z) = \sum_{z_0}^{z} \Delta t_\alpha(z_i) + \sum_{z_0}^{z} \Delta t_{dyn}(z_i), \tag{2.1}$$

where z_0 is the lowest height considered for the fall streak retrieval and z_i is a height of the fall streak between z_0 and z. The first term is the displacement time related to the antenna elevation, Δt_α. The second term is the displacement time due to the cloud system dynamics, Δt_{dyn}. Schematic concepts of both terms, elevation contribution and cloud dynamical part, are shown in Figure 2.4 (for a list of the most frequently used variables of the algorithm, see Table 2.2).

2.3.1. STEP 1: SCALING OF THE WIND PROFILES

Because measurements with the TARA radar profiler are performed under a fixed antenna elevation $\alpha = 45°$ and azimuth $\phi_T = 246.5°$ (measured clockwise from the North), the absolute horizontal wind has to be scaled to the line of sight. Using this scaled wind information, the scaling of the horizontal wind velocity along the azimuth direction of TARA vd_H is calculated

$$vd_H = -\cos(\phi_T - \phi_W)\, vd_h. \tag{2.2}$$

Here vd_h is the retrieved horizontal wind velocity component, ϕ_W is the retrieved wind direction, and ϕ_T the azimuth of the radar antenna.

2.3.2. STEP 2: RETRIEVING THE START TIME OF THE AVERAGING WINDOW

The focus of the retrieval algorithm is to obtain the fall streak structure within the cloud. In case of a raining system the cloud is defined as the part above the melting layer. Otherwise the retrieval starts at the radar detected cloud bottom, see examples in Figure 2.2. The higher variability of the wind in the cloud compared to the precipitation part of the cloud system makes it necessary to average the wind to get homogeneous wind profiles.

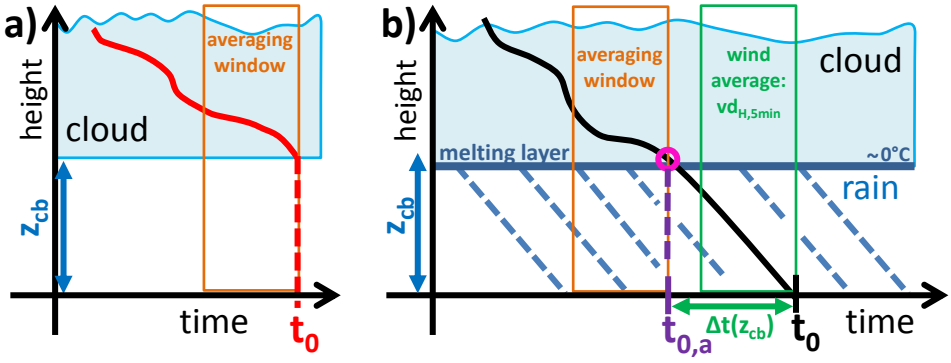

Figure 2.2: Schematics of how the retrieval estimates the best start time for the fall streak retrieval a) for a stratiform cloud and b) a precipitating cloud case. In a) the retrieval does not adjust the averaging time window. For a raining case the algorithm adjusts the position of the averaging window. Therefore $\Delta t(z_{cb})$ is calculated in Equation 2.3 using a fixed z_{cb} and the averaged wind profile $vd_{H,5min}$.

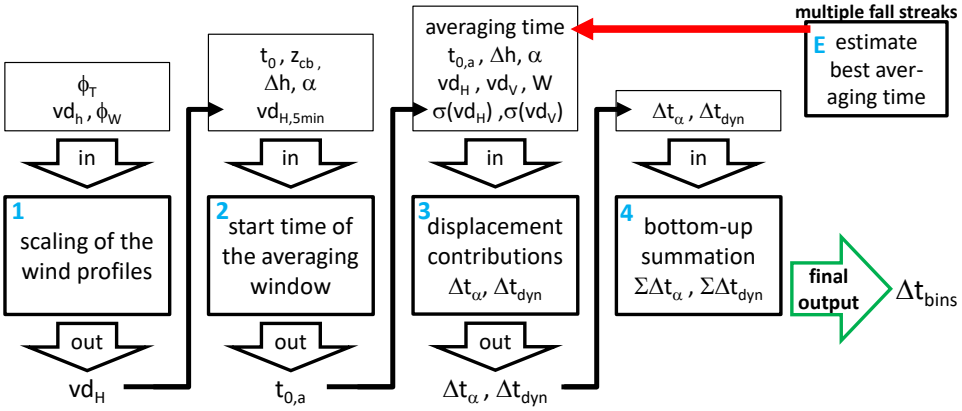

Figure 2.3: Flow chart of the fall streak retrieval algorithm. Boxes 1 to 4 show the general retrieval routines with the needed input and output variables for each step. Box E deals with the estimation of the best averaging window within a fixed time frame to retrieve multiple fall streaks.

To do so the averaging window can be optimized in terms of location as well as in terms of averaging time.

To get the best representation of the cloud dynamics the averaging window has to be shifted to the cloud region of interest. The reference for the averaging is where the fall streak is expected to be in the cloud. Figure 2.2 shows the two possible scenarios that are considered in the retrieval. In case of a non precipitating cloud the lowest height bin that can be trusted in the cloud is defined (Figure 2.2 a). To avoid any cloud boundary issues like turbulence or evaporation effects, the start point can be also set a few height bins above the detected cloud base. In case of rain the first height bin above the melting layer and the corresponding time shift $t_{0,a}$ with respect to t_0 has to be retrieved, see example in Figure 2.2 b). This is done using the following equation:

$$\Delta t(z_{cb}) = t_0 - t_{0,a} = \sum_{z_0}^{z_{cb}} \Delta t_\alpha(z_i) = \sum_{z_0}^{z_{cb}} \frac{\Delta x}{vd_{H,5\,min}(z_i)}. \tag{2.3}$$

where $\Delta t(z_{cb})$ is the time shift at cloud base height z_{cb} and $\Delta x = \frac{\Delta h}{\tan\alpha}$ a fixed horizontal distance (Figure 2.4 and Equation 2.4). The cloud base or melting layer height z_{cb} is currently estimated manually and set above the visible melting layer signatures of the reflectivity.

The start point of the averaging window is obtained by defining the intersection of z_{cb} with a first order approximation fall streak calculated below the cloud using a five minute averaged horizontal Doppler velocity profile, $vd_{H,5\,min}$. 5 minutes are chosen according to Unal [21] to create a homogeneous wind profile within the rain.

As seen in Figure 2.5 a) that shows the summation of Δt_α (black) and Δt_{dyn} (blue) (Section 2.3 2.3.5), Δt_α is the dominating term in rain. Δt_α therefore can be taken as a first fall streak approximation in the rain without pre-computation of dynamics required. The displacement time Δt_{dyn} is important in the cloud part above 2.3 km. The melting process of particles can be clearly identified by the velocity increase in the vd_V profile in

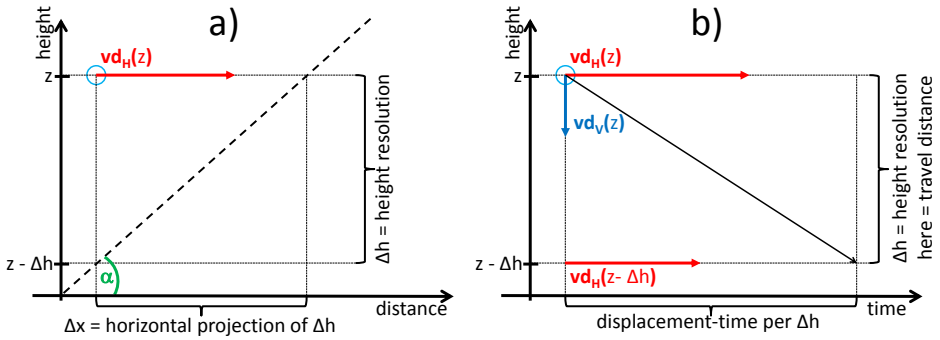

Figure 2.4: Sketches a) and b) illustrate the basic concept behind the calculation of Δt_α a) and Δt_{dyn} b), respectively. vd_H indicates horizontal Doppler velocity (red), vd_V is vertical Doppler velocity (blue). α is the radar elevation (green) and Δh the radar height resolution.

Figure 2.5 b). Using this setup with a fixed and known cloud base or melting layer height, respectively, the starting point of the averaging can be estimated automatically.

2.3.3. STEP 3: ELEVATION CONTRIBUTION

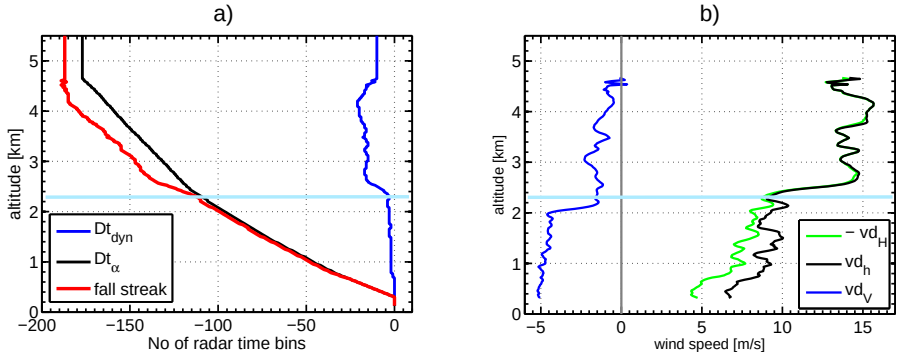

Figure 2.5: Profiles of the two parts of the fall streak retrieval a) and the corresponding wind profiles b). a) shows the summed up dynamical contribution $\sum_{z_0}^{z} \Delta t_{dyn}$ (blue) and elevation contribution $\sum_{z_0}^{z} \Delta t_\alpha$ (black) as a function of TARA time bins with respect to t_0. The resulting fall-streak is given in red. b) shows averaged wind and mean Doppler velocity profiles. vd_h (black) is the horizontal wind speed while in green $-vd_H$ the corresponding horizontal Doppler velocity is shown ($-vd_H$ for a better comparison, Doppler velocity include wind direction information; negative: wind towards the radar), and vd_V is the vertical Doppler velocity profile (blue). The light blue lines indicate the melting layer height of the cloud.

The displacement time $\Delta t_\alpha(z)$ due to the antenna elevation is a function of the averaged horizontal Doppler velocity $vd_H(z)$. This velocity is assumed to be constant within the radar height bin Δh. So that $\Delta t_\alpha(z)$ can be calculated:

$$\Delta t_\alpha(z) = \frac{\Delta x}{vd_H(z)} \tag{2.4}$$

Equation 2.4 relates the horizontal Doppler velocity within a measurement volume to a travel distance using a geometrical expression that is sketched in Figure 2.4 a). This makes it possible to calculate a displacement time for each height bin. Equation 2.4 also shows that for high elevation α, this time decreases. It becomes zero for zenith pointing radar measurement, $\alpha = 90°$. Such a contribution keeps the displacement due to cloud dynamics independent from radar elevation so that it can be directly used in vertical pointing mode.

2.3.4. STEP 3: DYNAMICAL CONTRIBUTION

The calculation of the displacement time caused by the cloud dynamics is represented by $\Delta t_{dyn}(z)$, Equation 2.5. The first two terms, the travel time along the vertical and relative horizontal displacement, are related to the existing fall streak theory [8, 10]. The third term is related to turbulence and is empirical, based on observations made during the retrieval development.

$$\Delta t_{dyn}(z) = \overbrace{\frac{\Delta h}{vd_V(z)}}^{travel\,time} \cdot \overbrace{\frac{(vd_H(z) - vd_H(z-\Delta h))}{vd_H(z)}}^{relative\,horizontal\,displacement} \cdot \overbrace{\frac{(\sigma(vd_H(z)) + \sigma(vd_V(z)))}{W(z)}}^{f_{turb}=turbulence\,contribution\,term}, \; f_{turb} \geq 1$$

$$\Delta t_{dyn}(z) = \underbrace{\frac{\Delta h}{vd_V(z)}}_{travel\,time} \cdot \underbrace{\frac{(vd_H(z) - vd_H(z-\Delta h))}{vd_H(z)}}_{relative\,horizontal\,displacement}, \; f_{turb} < 1 \tag{2.5}$$

where $vd_V(z)$ is the vertical Doppler velocity, $vd_H(z)$ and $vd_H(z-\Delta h)$ are the horizontal Doppler velocities within the considered height bin and the bin below, respectively (Δh is the height resolution); These velocities result from averaged profiles and therefore assumed to be constant per height bin. $\sigma(vd_H(z))$ and $\sigma(vd_V(z))$ are the standard deviations of the horizontal and vertical Doppler velocities per height bin within the averaged time window, and $W(z)$ is the mean Doppler spectrum width during the averaging period. Consequently the last term is a ratio of turbulence contribution at different spatial scales (large scale to radar resolution scale).

The *first term* in Equation 2.5 describes the travel time (the time particle population needs to fall through one radar height bin). Figure 2.4 b) illustrates that vd_V (blue arrow) is a good representation of the mean vertical particle velocity if the falling particle population is not influenced by turbulence or horizontal advection [22]. Knowing the height resolution, therefore, allows calculating the travel time in the vertical direction. The contribution of horizontal advection and turbulence is taken into consideration in the remaining two terms.

The *second term* of Equation 2.5 calculates the advection or relative horizontal displacement of fall streaks, which depends on the difference of vd_H between the sampling volume and the one below (Figure 2.4 b, red arrows). The slope of the fall streak depends on the horizontal wind shear. Therefore, in case of no horizontal wind shear the fall streak should feature a straight vertical line (time-height domain), identical to the non-corrected radar profile. In that case, no adding or subtracting of time bins is required to reconstruct the fall streak and therefore the factor is 0. The second term can be ex-

pressed as $1 - \frac{vd_H(z-\Delta h)}{vd_H(z)}$, which equals $1 - \frac{vd_h(z-\Delta h)\cos(\phi_T - \phi_W(z-\Delta h))}{vd_h(z)\cos(\phi_T - \phi_W(z))}$ using Equation 2.2. A singularity is present when the retrieved wind direction, Φ_W, is orthogonal to the looking direction of TARA, Φ_T, and there is a wind direction shear between $z - \Delta h$ and z. In those cases, $\Delta t_{dyn}(z)$ cannot be estimated. Generally, within a cloud system a shear in horizontal wind (velocity and/or direction) is expected, but perfect orthogonality between the retrieved wind direction and the looking direction of TARA is rare, strongly limiting the occurrence of the singularity.

At last, in Equation 2.5 a turbulence contribution, f_{turb}, is proposed. This *third term* is empirically derived. The third term can be considered as a correction to the first and second term. The fall streak retrieval uses a time averaging window. Therefore, a mean horizontal wind is considered (to partially mitigate non-homogeneity in the 3 beams). During this averaging time, the velocities $vd_V(z)$ and $vd_H(z)$ may vary and that affects the fall streak retrieval. To account for this, their standard deviations, estimated from the time averaging window and normalized to the Doppler spectrum width are introduced in the third term. This term is generally necessary for the cloud part where more variability (more turbulence) is expected compared to rain. Because of the relationship of the Doppler spectral width to the particle size distribution the denominator cannot become 0 if particles within the sampling volume are present. Therefore, a singularity caused by $W = 0$ will not occur. The wind fields within cloud systems generally vary within the averaging period. The same can be said for the fall velocities of the particle population. Therefore, the standard deviations, $\sigma(vd_H(z))$ and $\sigma(vd_V(z))$, differ from zero. During all cases analyzed the numerator of f_{turb} was always larger or almost equal to W and so $f_{turb} \geq 1$. However, when the values of $f_{turb}(z) < 1$ the turbulence correction term should not be applied. In that case the dynamical contribution of the fall streak at height z is retrieved taking only the first two terms into account.

If in Equation 2.5 singularities occur ($vd_V(z)$ close to zero or orthogonal wind direction with wind direction shear), this will lead to a large and not representative number of time bins. Therefore, such values have to be filtered out and cannot be used in the retrieval. Only values of $\Delta t_{dyn}(z) < 3\sigma(\Delta t_{dyn}(t_0))$ are chosen, where $\sigma(\Delta t_{dyn}(t_0))$ is the standard deviation of the Δt_{dyn} -profile for the same starting time, t_0. Higher values are set to $3\sigma(\Delta t_{dyn}(t_0))$.

In comparison with the existing theory of Browne [10] and Marshall and Gunn [5], and following representations [12] no generation level at cloud top and no microphysical assumptions are used. A bottom-up approach is chosen instead, due to lower accuracy of the wind retrieval in the far range of the radar beam. So the reference point of the retrieval is as close to the ground as possible where we expect accurate dynamical information.

2.3.5. STEP 4: BOTTOM-UP SUMMATION OF Δt_α AND Δt_{dyn}

Figure 2.3 shows that the final step of the retrieval is the summation of Δt_α and Δt_{dyn} to obtain the total displacement time for the height z. These time shifts can be expressed in amount of radar time bins. By using the radar time resolution $\Delta t_{res} = 2.56$ s,

$$\Delta t_{bins}(z) = t_{0,bin}(z_0) + \sum_{z_0}^{z} \frac{\Delta t_\alpha(z_i)}{\Delta t_{res}} + \sum_{z_0}^{z} \frac{\Delta t_{dyn}(z_i)}{\Delta t_{res}} \tag{2.6}$$

where the values in the sum have to be rounded before the final summation. The displacement in time bins $\Delta t_{bins}(z)$ is calculated with respect to the measurement time, t_0 or $t_{0,a}$, expressed in bins, $t_{0,bin}(z_0)$, and the lowest point z_0 of the fall streak. As an example profiles of $\Delta t_{bins}(z)$ and of the individual contributions $\Delta t_{\alpha}(z)$ and $\Delta t_{dyn}(z)$, expressed in bins, are depicted in Figure 2.5 a).

This procedure strongly depends on the accuracy of retrieved winds which may decrease at far ranges. This decrease is caused on the one hand by a decrease of the radar sensitivity and on the other hand by the increasing physical separation of the three beam resolution volumes of the wind profiler with increasing range (height). With the bottom-up approach, errors are reduced, and no generation level has to be assumed. This procedure relates the retrieved fall streak to the $t_{0,bin}(z_0)$ which is closest to the bottom. But to get appropriate results for the fall streak within the cloud part, which is the aim of this retrieval, the position of the averaging window plays an important role. How to retrieve the right start point for different cases is explained in the next section.

2.4. DISCUSSION: LIMITATIONS AND REQUIREMENTS OF THE RETRIEVAL TECHNIQUE

2.4.1. RETRIEVED 3D WIND

Thanks to its three-beam configuration, the TARA radar can retrieve the full 3D wind field continuously at high resolution within the cloud systems, taking into account Doppler information within each beam. However, the wind retrieval decreases in quality in the region where the signal-to-noise-ratio (SNR) is low or when turbulence is present, or the wind field is inhomogeneous. Turbulence is often the highest at the cloud edges because of the de- and entrainment of air. Low SNR is also expected near the cloud top because there the particles are small in size and their concentration is low. Furthermore, the radar sensitivity is decreasing with increasing range (height). At cloud base for non-precipitating clouds, similar effects occur like entrainment of dry air leading to turbulence and evaporation, the later results in a SNR decrease. Due to the bottom-up structure of the algorithm, choosing z_{cb} slightly above the cloud base height improves the retrieval by reducing the propagation of cloud-base potential errors in the upper height bins. Additionally, the three-beam configuration can provide some bias near cloud edges due to the increased distance between the different probing beams. Assumed is that the beams measure the same dynamical conditions, but if the cloud top is turbulent, this assumption is not longer valid. Averaging horizontal and vertical Doppler velocities partially mitigate all these effects.

Low SNR is detected using linear-depolarization ratio (Ldr). This reflectivity ratio, cross-polar to co-polar, can be seen as NSR (Noise to Signal Ratio) [dB] in the cloud part because the cross-polar measurement within that area is below the noise level. Therefore this radar observable provides an estimation of the SNR, which is used to ensure the quality of the data. A threshold of $Ldr < -10\,\mathrm{dB}$ (SNR $> 10\,\mathrm{dB}$) is applied on TARA data in this paper. For the values of $Ldr > -10\,\mathrm{dB}$ the data are discarded.

Broadening of the Doppler spectra within the three-beams can also lead to biased wind information. The broadening of the Doppler spectrum can be caused by turbulence or by horizontal wind shear. In cases of wind shear the broadening within the

three-beam Doppler spectra might not be evenly spread. Furthermore, the spectra might be skewed towards the smaller particles, because of higher inertia of the bigger particles [23]. Large particles are less prone to follow the air stream flow compared to the smaller particles. Therefore, the calculated mean Doppler velocity of that volume shifts towards lower or larger fall speeds.

At last, the final result of the retrieval can also be influenced by multi modality of the spectra. Several microphysical processes can affect the particle population monitored along the fall streak. This sometimes can lead to the formation of a secondary particle population (new particle formation or particle growth), which in turns can lead to secondary fall velocity mode in the Doppler spectra. Such a secondary mode in the spectrum causes a broadening, affecting the calculated mean Doppler velocity and, therefore, the retrieved fall streaks. The algorithm is at the moment not capable of handling such a case.

Averaging is used to improve the wind estimates. It is worth mentioning that the averaging window size has an influence on the shape of the resulting fall streak.

2.4.2. AVERAGING WINDOW SIZE

The slope and shape of retrieved fall streaks depend on the retrieved wind input as well as on its averaging time. Therefore the choice of the average window for the wind average is the main influence of the fall streak shape. For a case study, the appropriate wind averaging can be estimated by a variation of the averaging time for a fixed start time. In the case of retrieving all the fall streaks within a fixed time-period, the averaging window has to be fixed. This fixed averaging window is selected in that way that it guarantees the best representation of the dynamical conditions during that period. In the following, a statistical method is proposed to estimate the best averaging window within a fixed time frame using a bias analysis of the retrieved fall streaks (Step E in Figure 2.3).

The time averaging window is calculated so that it minimizes the influence of small and large scale dynamical structures that affect wind profiles. The bias-analysis compares the variability of retrieved fall streaks for different lengths of the averaging window. The calculation of the bias profile $B(\Delta t_{ref}, z)$ at starting time t_0 is function of the time bin displacement for the chosen reference window size Δt_{ref} at a given height z and the number of averaging window sizes N:

$$B(\Delta t_{ref}, z, t_0) = \left(\frac{1}{N}\sum_{a=1}^{N}(\Delta t_{ref}(z, t_0) - \Delta t_a(z, t_0))^2\right)^{\frac{1}{2}}. \tag{2.7}$$

Δt_a corresponds to the retrieved fall streaks for the N different averaging window widths. To get a better representation for the whole time period, the calculation is done for several start times t_0 within the chosen time period. In a next step, the bias is normalized. The normalization is done via:

$$B_n(\Delta t_{ref}, z, t_0) = \frac{B(\Delta t_{ref}, z, t_0) - min(B(\Delta t_a, z, t_0))}{max(B(\Delta t_a, z, t_0)) - min(B(\Delta t_a, z, t_0))}. \tag{2.8}$$

where $min(B(\Delta t_a, z, t_0))$ and $max(B(\Delta t_a, z, t_0))$ represent the minimum and maximum values of all calculated $B(\Delta t_{ref}, z, t_0)$ that correspond to the same selected start time. In the last step, all normalized bias profiles of the same Δt_{ref} are averaged. It is an average

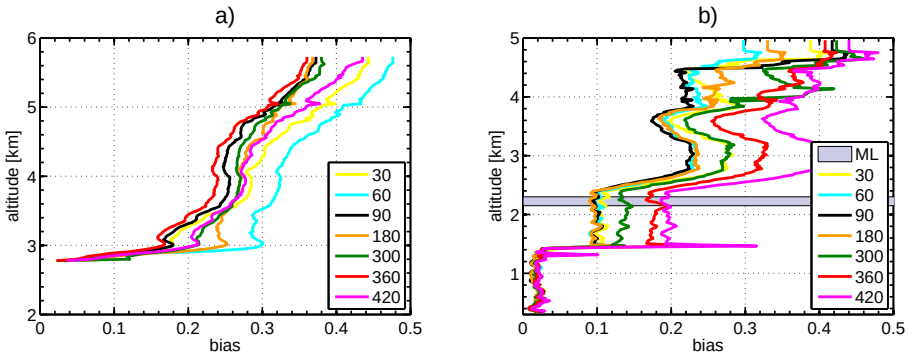

Figure 2.6: Normalized bias of the retrieved fall streaks with respect to different selections of the average window sizes within fixed time frame. a) mean normalized bias profile over 10 min for different reference averaging time windows in seconds (see legend) for a stratiform case 12^{th} Oct 2014, 1657-1707 UTC. b) mean normalized bias profile over 10 min for different reference averaging time windows in s (see legend) for a raining case 16^{th} Oct 2014, 0250-0300 UTC. The shaded area in b) indicates the melting layer height (ML).

over all the retrieved fall streaks ($B_n(\Delta t_{ref}, z)$). Therefore if the influence of the small or large scale turbulence is too strong the resulting bias value is large with respect to a more suitable averaging window size. The averaging window with the lowest bias gives the best representation within the whole time-period.

Figure 2.6 shows results of such an analysis for two cases. Both plots show analysis for a 10 min time-period with a one minute time difference between the different t_0. 14 different averaging window sizes ($N = 14$) were chosen for this analysis (10 s, 30 s, 60 s, 90 s, 120 s, 150 s, 180 s, 210 s, 240 s, 300 s, 360 s, 420 s, 480 s, 540 s). Figure 2.6 a) shows the analysis for a stratiform case. The profiles of the normalized and averaged bias are all quite near to each other at cloud base. After that, a divergence in the first 250 m is occurring. This bias is caused by evaporation and entrainment of dry air at cloud base. For 30 s and 60 s averaging window, the variability within the wind field seems to be high for the different t_0 so the resulting bias is high. Above 3 km the wind field is homogeneous and the bias profiles have almost the same shape. All in all, the 360 s profile shows the lowest bias values and therefore is selected to retrieve fall streaks within the 10 minutes time-period. To get more robust retrieval results the divergence in the first 250 m could be avoided by setting z_{cb} 250 m higher. However, the results in that area are still considered reasonable and it was chosen to keep the retrieval at cloud base in order to demonstrate that the retrieval can produce stable results even for such turbulence mixing areas (see Figure 2.7 a).

Figure 2.6 b shows results for a precipitating and dynamically more complex case. In the rain part, at heights below 1.5 km, all profiles are close and overlapping each other. Above 1.5 km single profiles have a higher bias when the averaging time is larger than 180 s. This can be caused by the inhomogeneity in the precipitation pattern. Above 4.5 km the divergence between the profiles increases, which is caused by a low SNR and more turbulence. The 90 s averaging window gives the best performance within the time period of 10 min. It is worth mentioning that the averaging window size for the raining case is much more critical than for the stratiform case (complex cloud dynamics). It is

demonstrated that different cases can lead to various window sizes.

2.5. RESULTS

Several fall streaks retrieved for two different cloud systems are presented in this section. Figure 2.7 d) and 2.8 d) show TARA measurements of, respectively, a stratiform and a raining cloud system obtained during the ACCEPT campaign. The results of the fall streak retrieval for those two cloud cases are depicted in Figures 2.7 a) and 2.8 a).

2.5.1. STRATIFORM CLOUD CASE: 12^{th} OCTOBER 2014

Figure 2.7 represents TARA measurements of a stratiform cloud of an approaching warm front on 12^{th} October 2014, at the Cabauw Experimental Site for Atmospheric Research (CESAR).

Table 2.2: List of variables

variables	description	unit
α	antenna elevation	°
B	bias of fall streaks at t_0	
B_n	normalized bias of the fall streaks at t_0	
Δt_α	time displacement (elevation contribution)	s
Δh	radar height resolution	m
Δt_{bins}	time bins to add or subtract per height bin	
Δt_a	time bin displacement	
Δt_{dyn}	time displacement (dynamical contribution)	s
Δt_{ref}	time bin displacement (reference averaging window size)	
Δt_{res}	radar time resolution	s
Δx	horizontal distance	m
Φ_T	azimuth of antenna, measured clockwise from the North	°
Φ_W	wind direction, measured clockwise from the North	°
N	number of averaging window sizes	
t_0	start time of a fall streak	UTC
$t_{0,a}$	start time of the wind averaging window	UTC
$t_{0,bin}$	start time bin of the fall streak retrieval	
vd_h	horizontal wind velocity	m s^{-1}
vd_H	horizontal Doppler velocity (along line of sight)	m s^{-1}
$vd_{H,5\,min}$	horizontal Doppler velocity, 5 min average	m s^{-1}
vd_V	vertical Doppler velocity	m s^{-1}
W	Doppler spectral width	m s^{-1}
z	height	m
z_0	start height of retrieval	m
z_{cb}	cloud base height	m
z_i	height between z_0 and z	m

Figure 2.7 a) depicts 8 retrieved fall streaks using a 6 minutes averaged wind profile

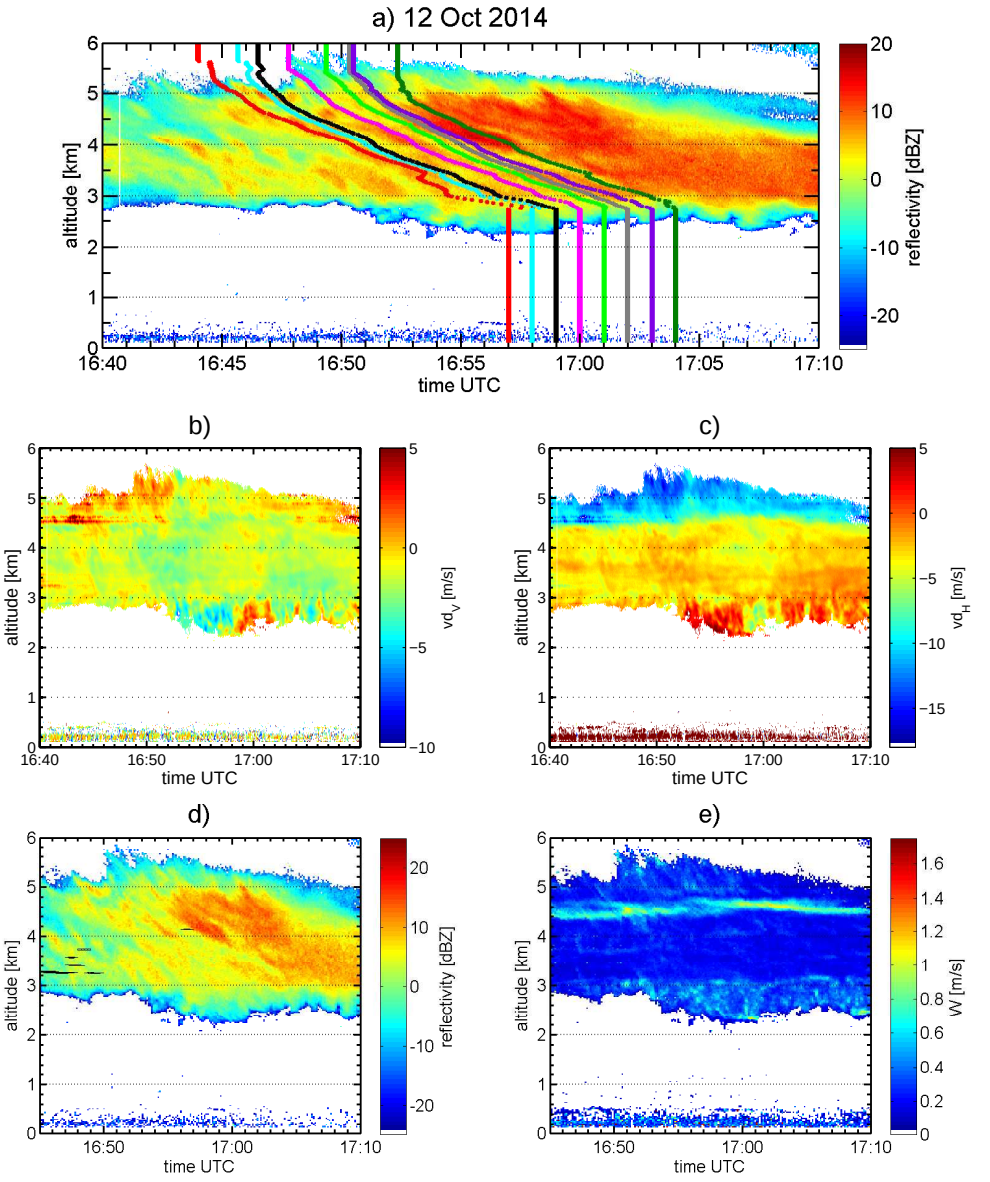

Figure 2.7: Overview of a stratiform cloud case of ACCEPT observed 12^{th} October 2014, 1640 - 1710 UTC. a) shows the reflectivity overlaid with 8 retrieved fall streaks, separated with one minute time difference from 1657 to 1704 UTC. b) and c) show plots of the vertical and horizontal Doppler velocities. d) is the reflectivity overlaid with the retrieved supercooled liquid water signatures from lidar (black) [19]. The Doppler spectrum width is shown in e).

and an approximate cloud base height $z_{cb} = 2.75$ km. The time between each fall streak retrieval is one minute, from 1657 till 1704 UTC. Due to dynamical homogeneity within the cloud, all fall streaks feature similar pattern. Only the first two fall streaks exhibit some turbulence effects occurring, below 3.0 km. This can be seen by the dots instead of a line representation of the fall streaks, and a higher displacement towards a higher number of time bins. Changes in the vertical Doppler velocity induced by the turbulence influence the contribution of the dynamics in Equation 2.5. For all fall streaks, a shift in slope occurs at around 4.5 km. This shift is due to the wind shear around 4.5 km that is clearly visible in the horizontal Doppler velocity profile vd_H which also associates with an increased Doppler spectral width W (see Figures 2.7 c) and e)). The microwave radiometer retrieved relative humidity values at 3 km are around 70 %. Mixing of dry air from below cloud base might also modify the Doppler width by acting on the particle size distribution, see Figure 2.7 e). Evaporation probably occurs at that height and below. It is also seen that turbulence effects due to changes in wind direction and de- and entrainment are also present in Figure 2.7 e). They might influence the Doppler spectra differently in the three radar-beams and therefore the wind field quality. In particular, the downdrafts and updrafts shown by the vertical Doppler velocity, Figure 2.7 b) above cloud base, are present but probably overestimated (the vertical Doppler velocity being a retrieval at 45° elevation). So the visible spikes and sharp changes in slopes of the first two retrieved fall streaks below 3.0 km are the consequences of such effects.

The mean f_{turb} is 6.53 with a standard deviation of 2.83 in the cloud. Although the cloud is dynamically homogeneous, the mean of f_{turb} is relatively large. There are two reasons for this. First the de- and entrainment at the cloud bottom increase the numerator of f_{turb}. Secondly, the horizontal wind direction is nearly perpendicular to the radar looking direction, introducing large variability in vd_H while W is small and stable, between 3 km and 4.5 km. Nevertheless, it is possible to retrieve fall streaks.

In Figure 2.7 d) no signature of supercooled liquid water is retrieved within the cloud system when using the method of de Boer *et al.* [19]. The liquid water path (LWP) measurements from the microwave radiometer show values below 25 g m^{-2} during this time. The presented cloud contains no supercooled liquid water, and no analysis of the spectra along such fall streaks is done.

2.5.2. PRECIPITATING CASE: 16th OCTOBER 2014

Figures 2.8 and 2.9 show a cloud system which was related to an occlusion front overpasses at the CESAR observatory in the night of the 16th October 2014. This example shows a precipitating cloud with embedded liquid layer so that the benefit to analyze growth processes related to supercooled liquid water using fall streak correction can be examined.

RETRIEVED FALL STREAKS

Figure 2.8 a) features the result of 10 different retrieved fall streaks from 0250 till 0259 UTC. All fall streaks are retrieved with 1.5 minutes averaged wind profiles with a one-minute interval. The wind profile averaging time is smaller than the one in the case in Section 2.5 2.5.1 because the dynamical conditions are less homogeneous. The mean f_{turb} is 4.64 with a standard deviation of 2.85 in the cloud part above the melting layer.

The melting layer can be identified by the increased reflectivity signature between 2.1 km and 2.35 km in Figure 2.8 a) and d) and the cloud base was set to $z_{cb} = 2.35$ km to retrieve

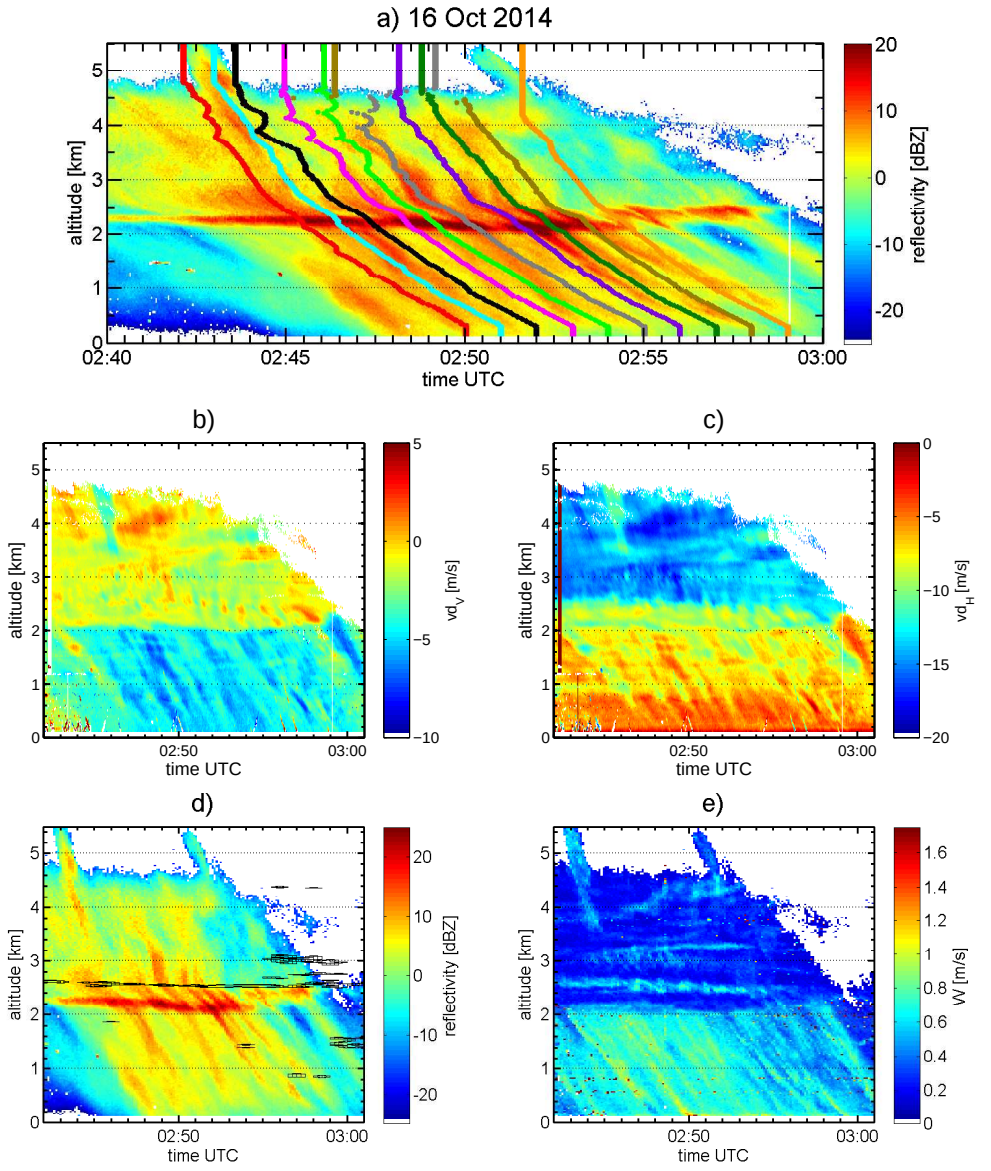

Figure 2.8: Overview of a raining cloud case of ACCEPT observed 16^{th} October 2014, 0240 - 0300 UTC. a) shows the reflectivity overlaid with 10 retrieved fall streaks separated by one minute time difference from 0250 to 0259 UTC. b) and c) show plots of the vertical and horizontal Doppler velocities, respectively. d) is the reflectivity overlaid with the retrieved supercooled liquid water signatures from lidar (black) [19]. The Doppler spectrum width is shown in e).

fall streaks for that case. The slopes of the retrieved fall streaks are parallel. They all capture a wind shear above the melting layer, that can be identified by the increased spectral Doppler width W in Figure 2.8 e), and in c) by the increased horizontal Doppler velocities above 2.5 km. It can also be seen that the fall streaks 3 till 6 (0252 - 0255 UTC) exhibit some spikes in their slopes in the upper part of the cloud (> 3.5 km). Alternations of down to upward motion in the vertical Doppler velocity field, as seen in Figure 2.8 b), produce heterogeneities in the vertical velocity field that lead to strong variability in the fall streak retrieval from one height bin to the other. This variability is due to the errors in the quantitative estimation of the input wind. When analyzing the broadening of the Doppler spectrum width around 3.2 km to 3.4 km in Figure 2.8 e) no relation to a visible change within the vd_V and vd_H plots is found. Besides, the bottom of a supercooled liquid layer was detected with the measurements of the Raman-lidar, see black contours in Figure 2.8 d). This retrieved information is used further by analyzing a spectrogram along a fall streak to identify microphysical changes of the ice crystals associated with the presence of detected supercooled liquid water layer.

SPECTROGRAMS

To identify and analyze changes in the ice particle microphysics and link them to the presence of supercooled liquid water, spectrograms are used. Spectrograms provide Doppler spectra information per height bin at each time step (spectral reflectivity versus Doppler velocity and height, elevation 45°). The Doppler spectra are related to both the hydrometeor size distribution and the dynamics of the measured volume. Because of this complexity, the analysis of microphysical changes is only done qualitatively by analyzing changes in the Doppler spectra shape (broadening, modality, and amplitude) with height. However, microphysical changes can only be interpreted by assuming that we look at the same population of particles.

Figure 2.9 a) shows a spectrogram as a vertical profile at 0251 UTC, while Figure 2.9 b) is the fall streak corrected spectrogram for the same starting time (along the light blue line in Figure 2.8 a). In the example presented in Figure 2.9 three specific features can be identified (see arrows and letters in Figure 2.9).

The first region features a spectral broadening between 3.5 km and 4 km, where multimodality can be identified in Figure 2.9 b). This broadening is not correlated with any dynamical effect from Figure 2.8 and therefore changes of the particle microphysics are taken into account. As indicated with arrows two different particle modes A and B can be identified and separated in the spectrogram between 4 km and 3.5 km. Between 3.8 km and 3.5 km even a third particle mode, C, occurs that even has higher Doppler velocities with respect to the other two modes. Other studies showed similar multi-modal structures of Doppler spectra when particles fall through a liquid layer and start to rime [2, 24]. Therefore we assume that a supercooled liquid layer is present in that region with riming processes involved. Because measurements are done under 45° elevation, the Doppler velocities do not correspond to the actual fall velocities of the particles. Nevertheless, the observed spread in velocity of almost 3 m s^{-1} in the Doppler spectrum at 3.6 km exhibits the possible differences in mean particle fall velocities in modes A, B, and C. Assuming a mean particle fall speed of 2 m s^{-1} for C would fit to rimed particles. Such processes are not present in the vertical profile spectrogram at the same heights. The spectrogram only shows a monomodal spectrum (single mode A). However, the time-height-plots of

reflectivity in Figure 2.8 indicate clear signs of particle growth (enhanced reflectivity) below 4 km that strongly suggests a change in the microphysical processes as detected from the fall streak corrected spectrogram. Below 3.5 km the signature of the separated particle modes A, B and C seems to end. Therefore, we expect that the observed particle population that included the riming mode C and the two other particle modes A

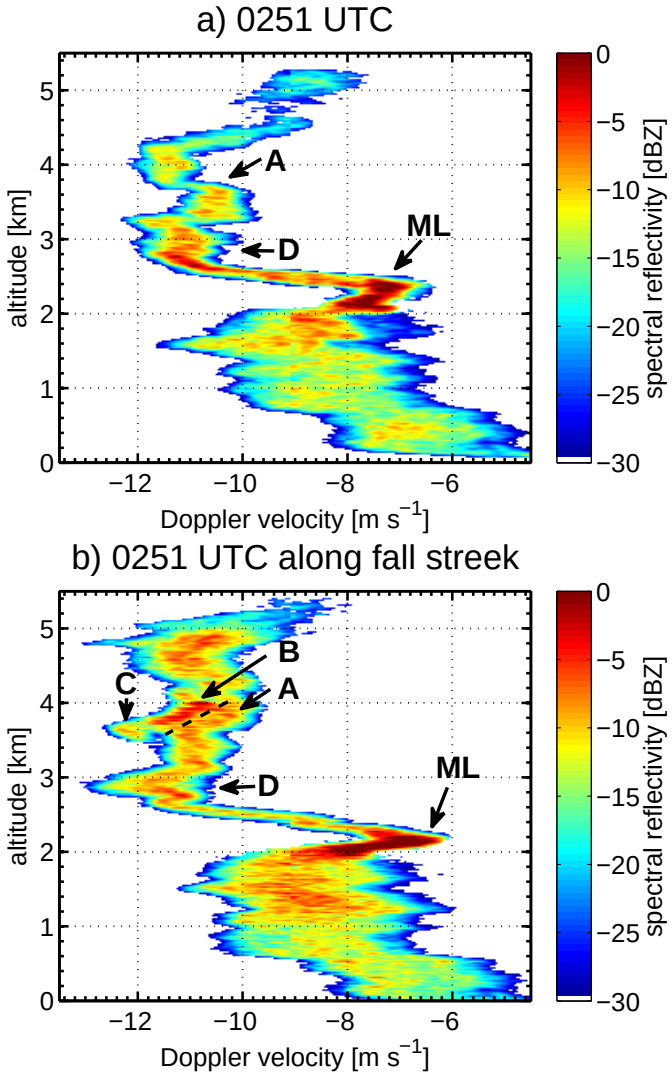

Figure 2.9: a) shows the vertical spectrogram of Doppler spectra at 0251 UTC. b) shows the fall streak corrected spectrogram at t_0 =0251 UTC (both at 45° elevation). Note that the Doppler velocity still contains the radial wind contribution. In b) A, B, and C indicates different particle modes identified at the upper particle growth process. a) only indicates a single particle mode A. D shows a region of particle growth that is present in both spectrograms. ML indicates the melting layer signature.

and B have not seeded further through the cloud system. So the reflectivity values below are lower and the spectrogram narrower again. Hence, we suggest that the fall streak corrected spectrogram at that heights represents the background particle population.

In Figure 2.9 b) a *second region*, indicated with a D, is visible between 2.6 km and 3.1 km. As for the first region, no significant wind shear can be detected in Figures 2.8 b) and c). The increase of reflectivity at the same heights in Figure 2.8 indicates microphysical changes that lead to a broadening of the spectra. At the bottom of the broadening signature at 2.6 km a supercooled liquid layer is retrieved by the lidar [19]. The broadening is probably caused by ice particle growth due to liquid water interaction (riming or Bergeron-Findeisen processes). This feature is again not present in the vertical profile spectrogram (indicated with a D), demonstrating the importance of using fall streaks corrected data.

The *third feature* is the increase of reflectivity within the rain pattern below the melting layer (melting layer in Figure 2.9 is indicated by ML). This feature is well correlated with the lowest particle growth processes, D, detected in the cloud and discussed above. The vertical profile spectrogram shows a weaker correlation of this cloud to rain conversion related to the detected particle growth processes.

Summarizing, it is shown in this section, that there is a strong potential for studying microphysical processes of a particle population along its path from cloud top to the bottom using the fall streak corrected spectrograms. In this example, enhanced cloud particle growth due to the presence of a liquid layer increases rainfall intensity. This type of pattern can be identified several times in the time-height-plots in Figure 2.8. Further analysis shows that this signature is correlated with the small pattern of upward motion in the vertical Doppler velocity field at around 2.6 km between 0250 UTC till 0258 UTC in Figure 2.8 b. Other studies have also demonstrated that updrafts promote the formation of supercooled droplets [7, 25].

2.6. CONCLUSION

In this paper, a new algorithm to retrieve fall streaks within a radar time-height-plot is presented. The aim is to study the microphysical process evolution of a single particle population through its fall. Fall streaks are based on the assumption that particle populations are constantly and homogeneously generated at cloud top. Under such hypothesis, the fall streak signature contains all evolution states of the tracked particle population and therefore their microphysical changes can be observed.

The unique aspect of the retrieval is that it relies on genuine high-resolution wind information obtained with the TARA radar (Transportable Atmospheric Radar), avoiding any assumption on the wind field from other sensors or models that are known to drastically affect the accuracy of the retrieval. The high spatial and temporal observations provided by TARA can be employed to retrieve fall streaks in the case of dynamically stable stratiform cloud cases (Section 2.5.1) as well as for precipitating and dynamically more complex cases (Section 2.5.2).

Several steps are taken into account to guarantee the quality of the input velocity field, based on adaptive averaged windows. The presented case studies suggest that the retrieval can produce robust results for stratiform clouds as well as for raining cases. Regarding microphysical process studies and particle growth due to supercooled liquid

water presence the spectrograms in Figure 2.9 display clearly the advantage of using the fall streak corrected spectrogram instead of the vertical profile spectrogram. Using fall streak corrected spectrogram the identified signatures can be linked to coherent microphysical processes. The coherent features observed can also be linked and compared better to the structures that are visible in the corresponding time-height plots.

Summarizing the presented retrieval technique provides the first algorithm for fall streaks that is completely independent of additional wind information, a prescribed relation between particle size and fall velocity, and particle generation level height. Such fall streaks offer a completely new perspective and potential to study cloud microphysics through process evolution analyses of the tracked particle populations.

REFERENCES

[1] M. D. Shupe, J. S. Daniel, G. de Boer, E. W. Eloranta, P. Kollias, C. N. Long, E. P. Luke, D. D. Turner, and J. Verlinde, *A Focus On Mixed-Phase Clouds,* Bulletin of the American Meteorological Society **89**, 1549 (2008).

[2] H. Kalesse, W. Szyrmer, S. Kneifel, P. Kollias, and E. Luke, *Fingerprints of a riming event on cloud radar doppler spectra: observations and modeling,* Atmospheric Chemistry and Physics **16**, 2997 (2016).

[3] P. Kollias, E. E. Clothiaux, M. A. Miller, B. A. Albrecht, G. L. Stephens, and T. P. Ackerman, *Millimeter-Wavelength Radars: New Frontier in Atmospheric Cloud and Precipitation Research,* Bulletin of the American Meteorological Society **88**, 1608 (2007).

[4] H. R. Pruppacher and D. J. Klett, *Microphysics of Clouds and Precipitation* (Springer, 1996) p. 976.

[5] J. S. Marshall and K. L. S. Gunn, *Measurement of Snow Parameters by Radar.* Journal of Atmospheric Sciences **9**, 322 (1954).

[6] S. E. Yuter and R. A. Houze, *Microphysical modes of precipitation growth determined by S-band vertically pointing radar in orographic precipitation during MAP,* Quarterly Journal of the Royal Meteorological Society **129**, 455 (2003).

[7] A. Heymsfield, *Cirrus Uncinus Generating Cells and the Evolution of Cirriform Clouds. Part II: The Structure and Circulations of the Cirrus Uncinus Generating Head.* Journal of Atmospheric Sciences **32**, 809 (1975).

[8] J. S. Marshall, *Precipitation Trajectories and Patterns.* Journal of Atmospheric Sciences **10**, 25 (1953).

[9] A. Heymsfield, *Cirrus Uncinus Generating Cells and the Evolution of Cirriform Clouds. Part I: Aircraft Observations of the Growth of the Ice Phase.* Journal of Atmospheric Sciences **32**, 799 (1975).

[10] I. C. Browne, *Precipitation streaks as a cause of radar upper bands,* Quarterly Journal of the Royal Meteorological Society **78**, 590 (1952).

[11] P. M. Mittermaier, J. R. Hogan, and J. A. Illingworth, *Using mesoscale model winds for correcting wind-drift errors in radar estimates of surface rainfall,* Quarterly Journal of the Royal Meteorological Society **130**, 2105 (2004).

[12] R. J. Hogan and S. F. Kew, *A 3D stochastic cloud model for investigating the radiative properties of inhomogeneous cirrus clouds,* Quarterly Journal of the Royal Meteorological Society **131**, 2585 (2005).

[13] C. Unal, Y. Dufournet, T. Otto, and H. Russchenberg, *The new real-time measurement capabilities of the profiling TARA radar,* in *Article in monograph or in proceedings* (ERAD 2012 - 7th European conference on radar in meteorology and hydrology, Toulouse, France, 24-29 June 2012, 2012).

[14] S. H. Heijnen, L. P. Ligthart, and H. W. J. Russchenberg, *First Measurements with TARA; An S-Band Transportable Atmospheric Radar,* Physics and Chemistry of the Earth B **25**, 995 (2000).

[15] C. M. H. Unal and D. N. Moisseev, *Combined Doppler and Polarimetric Radar Measurements: Correction for Spectrum Aliasing and Nonsimultaneous Polarimetric Measurements,* Journal of Atmospheric and Oceanic Technology **21**, 443 (2004).

[16] J. Bühl, P. Seifert, U. Wandinger, H. Baars, T. Kanitz, J. Schmidt, A. Myagkov, R. Engelmann, A. Skupin, B. Heese, A. Klepel, D. Althausen, and A. Ansmann, *LACROS: the Leipzig Aerosol and Cloud Remote Observations System,* in *Society of Photo-Optical Instrumentation Engineers (SPIE) Conference Series*, Society of Photo-Optical Instrumentation Engineers (SPIE) Conference Series, Vol. 8890 (2013) p. 2.

[17] A. Myagkov, P. Seifert, U. Wandinger, J. Bühl, and R. Engelmann, *Relationship between temperature and apparent shape of pristine ice crystals derived from polarimetric cloud radar observations during the ACCEPT campaign,* Atmospheric Measurement Techniques **9**, 3739 (2016).

[18] U. Görsdorf, V. Lehmann, M. Bauer-Pfundstein, G. Peters, D. Vavriv, V. Vinogradov, and V. Volkov, *A 35-GHz Polarimetric Doppler Radar for Long-Term Observations of Cloud Parameters - Description of System and Data Processing,* Journal of Atmospheric and Oceanic Technology **32**, 675 (2015).

[19] G. de Boer, E. W. Eloranta, and M. D. Shupe, *Arctic Mixed-Phase Stratiform Cloud Properties from Multiple Years of Surface-Based Measurements at Two High-Latitude Locations,* Journal of Atmospheric Sciences **66**, 2874 (2009).

[20] D. Althausen, R. Engelmann, H. Baars, B. Heese, A. Ansmann, D. Müller, and M. Komppula, *Portable Raman lidar Polly^{XT} for automated profiling of aerosol backscatter, extinction, and depolarization,* Journal of Atmospheric and Oceanic Technology **26**, 2366 (2009).

[21] C. Unal, *High-Resolution Raindrop Size Distribution Retrieval Based on the Doppler Spectrum in the Case of Slant Profiling Radar,* Journal of Atmospheric and Oceanic Technology **32**, 1191 (2015).

[22] P. Kollias and B. Albrecht, *Vertical Velocity Statistics in Fair-Weather Cumuli at the ARM TWP Nauru Climate Research Facility,* Journal of Climate **23**, 6590 (2010).

[23] A. C. P. Oude Nijhuis, F. J. Yanovsky, O. A. Krasnov, C. M. H. Unal, H. W. J. Russchenberg, and A. Yarovoy, *Assessment of the rain drop inertia effect for radar based turbulence intensity retrievals,* Int. J. Microw. Wirel. Technol. (2016).

[24] M. Oue, M. R. Kumjian, Y. Lu, Z. Jiang, E. E. Clothiaux, J. Verlinde, and K. Aydin, *X-Band Polarimetric and Ka-Band Doppler Spectral Radar Observations of a Graupel-Producing Arctic Mixed-Phase Cloud,* Journal of Applied Meteorology and Climatology **54**, 1335 (2015).

[25] M. R. Kumjian, S. A. Rutledge, R. M. Rasmussen, P. C. Kennedy, and M. Dixon, *High-Resolution Polarimetric Radar Observations of Snow-Generating Cells,* Journal of Applied Meteorology and Climatology **53**, 1636 (2014).

3

OBSERVATIONS OF ICE PARTICLE GROWTH PROCESSES USING SPECTRAL POLARIMETRIC RADAR DATA

Abstract: The growth of ice crystals in presence of super-cooled liquid droplets represents the most important process for precipitation formation in the mid-latitudes. Such mixed-phase interaction processes remain however pretty much unknown, as capturing the complexity in cloud dynamics and microphysical variabilities turns to be a real observational challenge. Ground-based radar systems equipped with fully polarimetric and Doppler capabilities in high temporal and spatial resolutions such as the S-band Transportable Atmospheric Radar (TARA) are best suited to observe mixed-phase growth processes. In this paper, measurements are taken with the TARA radar during the ACCEPT campaign (Analysis of the Composition of Clouds with Extended Polarization Techniques). Besides the common radar observables, the 3D wind field is also retrieved due to TARA unique three beam configuration. The novelty of this paper is to combine all these observations with a particle evolution detection algorithm based on a new fall streak retrieval technique in order to study ice particle growth within complex precipitating mixed-phased cloud systems. In the presented cases, three different growth processes of ice crystals, plate-like crystals, and needles, are detected and related to the presence of supercooled liquid water. Moreover, TARA observed signatures are assessed with co-located measurements obtained from a cloud radar and radiosondes. This paper shows that it is possible to observe ice particle growth processes within complex systems taking advantage of adequate technology and state of the art retrieval algorithms. A significant improvement is made towards a conclusive interpretation of ice particle growth processes and their contribution to rain production using fall streak rearranged radar data.

3.1. INTRODUCTION

The interaction of liquid water droplets and ice crystals leads to an enhanced growth of the ice crystals while falling through layers of super-cooled liquid water. In the mid-latitudes, this is an important process for precipitation formation [1, 2]. Nevertheless, the implications of the microphysical processes on precipitation formation is currently not well understood. Such microphysical processes involve a variety of hydrometeor sizes, shapes, phases, all affected by cloud dynamics, making the observation particularly challenging [3, 4]. Nowadays, ground-based radar measurement techniques have the advanced capabilities to observe and study microphysical processes within mixed-phase cloud systems [3]. Analyses of ice particle growth processes within mixed-phase cloud systems are primarily based on cloud radar data. Among them, Oue *et al.* [5] uses polarimetric radar (K_a-, and X-band) and lidar measurements to study ice particle growth processes in the cloud. Kalesse *et al.* [6] analyzes Doppler spectra (K_a-band) during a riming event and compare their findings of particle growth rates from the observations to simulations of such a riming even. Data from the same measurement campaign are used by [7], where they apply a radar triple frequency method (W-, K_a-, and X-band) to distinguish between different ice hydrometeor types (aggregates, rimed particles) and their particle size distribution characteristics during snowfall events. Myagkov *et al.* [8] uses polarimetric radar measurements (K_a-band) to derive the shape and orientation of mainly pristine ice particles generated at liquid topped mixed phase clouds.

In the studies mentioned above, the focus is on stratiform and layered clouds (dynamically stable and homogeneous) in the Arctic region or on snowfall events that do not involve any phase transition (ice particles constantly remain in the ice phase). Studies of precipitating mixed-phase cloud systems where melting of the ice particles is involved are rare. However, to understand the whole precipitation formation process the growth of the ice particles and the associated microphysical processes above the melting layer have to be studied to be related to the precipitation intensity below the melting layer. Nevertheless, the frequency bands listed in the studies above (W-, K_a-, and X-band) suffer from attenuation when it comes to observations of precipitation cloud systems, Kollias *et al.* [3]. To avoid attenuation in precipitation, radars that operate in lower radar frequencies (C- and S-band) can be used. An example of attenuation of a K_a-band radar in comparison to an S-band radar profiler is depicted in the reflectivity fields in Figures 3.4 a) and b). The reflectivity difference due to attenuation reaches up to 20 dBZ above the melting layer (1010-1020 UTC and 1140-1150 UTC). In the past, low-frequency radars were mainly used to estimate precipitation [9] and to classify hydrometeor types [10, 11]. However, in the last few years, the polarimetric capabilities of those radars were also used to study ice particle microphysics and growth processes in cloud systems (during snowfall events or in the ice part of the cloud above the melting), Kennedy and Rutledge [12], Bechini *et al.* [13], Moisseev *et al.* [14]. Microphysical studies of ice crystal habits using a C-band radar were first done by Bader *et al.* [15]. They compared differential reflectivity, Z_{DR}, signatures from the radar with aircraft measurements of ice crystal habits of precipitating stratiform clouds. It was found that the enhanced bands of Z_{DR} values occur where the aircraft measurements detected defined pristine ice particle shapes. Later it was found that a combination of Z_{DR} and specific differential propagation phase, K_{DP}, can be used to identify regions of plate-like particle

growth processes and onset of aggregation [12, 14]. Andrić *et al.* [16] modeled polarimetric signatures for a winter storm case. The related simulations showed agreements with the observations; nevertheless, the model was not able to match all the features of the observations in a single run.

Low-frequency radar observation of ice particle growth process due to the interaction of the ice crystals with supercooled liquid droplets is also found in the literature. Field *et al.* [17] compared the observed Z_{DR} signatures (C-band) to the obtained ice to liquid particle fraction measured with an aircraft and found a good agreement between liquid water presence and Z_{DR} signatures that were caused by defined ice crystal shapes. Similar findings have also been made by Hogan *et al.* [18]. Hogan *et al.* [18] showed that small convective cells embedded in warm frontal mixed-phase cloud systems triggered ice particle formation, growth, and multiplication related to super-cooled liquid water. Chandrasekar *et al.* [11] discussed spectrograms measured with a C-band radar that exhibit signatures of aggregation and riming of ice particles. This shows that precipitation radar can capture particle growth in spectral domain and their related microphysics.

In this work, radar data measured during the ACCEPT campaign are presented. They are obtained with TARA, which is a fully polarimetric S-band Doppler radar profiler providing measurements in high temporal and spatial resolutions. Because of TARA's unique 3 beam configuration, the full 3D wind vector per sampling volume is also retrieved for each measurement. Therefore, using this radar and its configuration, it is possible to identify and study microphysical processes of ice particles within complex mixed-phase clouds. On top of that, TARA measurements are rearranged along fall streaks according to the recently developed fall streak retrieval algorithm [19]. Fall streaks are considered to be the precipitating path of a population of particles from top to bottom of the cloud system. Therefore, the analyzes of microphysical changes along the fall streaks contain information of microphysical evolution of the same particle population [6, 19]. The retrieval technique reconstructs the precipitation path based on the obtained TARA wind information. In a next step, Doppler spectra and polarimetric radar variables rearranged along those fall streaks are used to study the microphysical evolution of a particle population. This paper demonstrates the advantage of analyzing data along fall streak instead of vertical profiles of radar data. Rearranged spectrograms of polarimetric variables allow to understand how the ice particle size and shape distribution changes versus height. This is used to improve the understanding of the impact of super-cooled liquid water on ice particle growth within a cloud system. Furthermore, the spectral signatures are compared to additional measurements performed during the ACCEPT campaign (K_a-band cloud radar spectral information and radiosonde temperature profiles) to assess the results from TARA data. After introducing the observation strategy of the ACCEPT campaign, in Section 3.2, some examples of microphysical observations of ice particle growth processes and their spectral signatures are given in Sections 3.3 and 3.4. An overview of the fall streak technique is given in Section 3.5. Section 3.6 finally combines the retrieved microphysical information with fall streak correction to interpret growth processes of three different cases. Discussions and conclusions are provided in Section 3.7.

Figure 3.1: Measurement setup of the ACCEPT campaign at CESAR. The arrows point on the TARA radar (radar on the left), the disdrometer that is mounted on the LACROS container, and the vertical pointing Mira cloud radar (35 GHz). Complementary instruments of ACCEPT are listed but not visible on this photo.

3.2. OBSERVATION STRATEGY

3.2.1. INSTRUMENTAL SETUP OF THE ACCEPT CAMPAIGN

The aim of the ACCEPT campaign (Analysis of the Composition of Clouds with Extended Polarization Techniques) is achieving a better understanding of microphysical processes involved in mixed-phase clouds using high-resolution polarimetric observations. The measurements were performed from October to mid-November 2014 at the Cabauw Experimental Site for Atmospheric Research (CESAR), the Netherlands. An instrumental synergy was used during ACCEPT to detect the different phases, the variety of sizes and shapes of the involved hydrometeors. For this purpose the TARA radar [20] at the site was extended by several other sensors: the Leipzig Aerosol and Cloud Remote Observation System (LACROS) [21], a second vertically pointing K_a-band cloud radar Mira [22], and the Raman Lidars Polly^{XT} [23, 24] and CAELI (CESAR Water Vapour, Aerosol and Cloud Lidar) [25]. A picture of the setup is provided in Figure 3.1. During special observation periods, radiosondes were launched at the site. Some results of the ACCEPT campaign are already published. Myagkov *et al.* [8] developed a retrieval to obtain the shapes of new generated ice crystals at liquid topped single layer mixed-phase clouds and compared their results to laboratory studies. Good agreement was obtained. Pfitzenmaier *et al.* [19] developed a retrieval algorithm to reconstruct fall streaks within the TARA measurements to improve the study of ice particle growth due to supercooled liquid water presence within the cloud system.

3.2.2. THE TRANSPORTABLE ATMOSPHERIC RADAR - TARA

TARA is a frequency modulated continuous wave (FM-CW) S-band radar profiler (3.3 *GHz*) that has full polarimetric and Doppler capabilities. TARA is able to provide high-resolution column measurements in the Doppler domain (0.03 m s^{-1}), in range (30.0 m, max. height of 10.05 km) as well as high temporal resolution (2.56 s). Measurements are performed under a fixed antenna elevation (45°) and a fixed azimuth (246.5° related to the North). Measurements at 45° elevation are considered as an optimum to get polarimetric and Doppler spectra information related to microphysical properties of the probed medium [26, 27]. Therefore, TARA does not only allow the analysis of polarimetric bulk parameters as differential reflectivity, Z_{DR}, and co-polar correlation coefficient, ρ_{HV}, but it is also possible to study changes in the signatures of Doppler spectra, sZ, and spectral differential reflectivity ,sZ_{DR} (sZ_{DR} being the ratio of horizontal polarized to vertical polarized spectral reflectivity, $sZ_{\mathrm{hh}}/sZ_{\mathrm{vv}}$). These changes in the spectra and spectrogram

(height profiles of spectra) can be related to cloud microphysical variations. Therefore, it is possible to identify separate particle modes (having different velocity ranges) in the sZ and sZ_{DR} spectra. Furthermore, the unique three-beam configuration of TARA allows retrieving the full 3D wind vector per measurement. Using the Doppler spectra information of the three beams, main beam and two offset beams, the horizontal wind velocity vd_h, the vertical Doppler velocity vd_V , and the wind direction ϕ_W are retrieved with a minimal temporal resolution of 2.56 s [27]. Examples of wind velocities and the wind direction fields are displayed in Figure 3.5 b) to d). The combination of all these measurements makes it possible to study ice particle growth within such complex precipitating mixed-phase cloud systems. Table 4.1 gives an overview over the specifications of TARA during ACCEPT.

3.2.3. INSTRUMENTAL SYNERGY

In addition to the TARA radar, other co-located sensors measured in parallel, allowing full comparison of the observed data signatures for similar volumes of study. In this paper, measurements of the Mira and TARA radars are compared, and data from two radiosonde launches are used. Unlike TARA, the data of high-frequency, Mira type, radar systems, suffer from attenuation during precipitation events. Low-frequency radar systems with high spatial and temporal resolution like the TARA radar have advantages measuring precipitation cloud systems. Nevertheless, the K_a-band radar is more sensitive to the smaller pristine ice particles near cloud top. Therefore, it can detect particles in far ranges where TARA, operating at a low-frequency, is not able to measure these small particles. Despite of the attenuation the detected cloud top with Mira is at least 0.5 km higher than the one identified with TARA. TARA and the vertical pointing Mira obtain linear depolarization ratio in the spectral domain (sL_{DR}) at high temporal resolution (1 s for Mira). This parameter, which is the ratio of sZ_{vh}, cross-polar received spectral reflectivity, to sZ_{hh}, is not affected by attenuation issues at vertical incidence. Therefore, comparisons between the observed spectral polarimetric signatures from TARA and Mira can be done. These spectral polarimetric measurements are used in combination with thermodynamical conditions (temperature and humidity) within the cloud system, measured from radiosonde launches. On the one hand, radiosondes can retrieve regions of super-cooled liquid water within precipitating cloud systems when other methods or sensors are limited. On the other hand, the temperature profiles in super-cooled liquid layer and the polarimetric radar signatures can help identifying the dominant ice particle shape affecting the growth process in the mixed-phase area [1, 8, 15, 29].

3.3. ICE PARTICLE GROWTH PROCESSES

Ice particles within clouds can grow through three main processes [1, 2].

- *Riming of ice particles*: occurs when supercooled water droplets collide and freeze onto bigger ice crystals, see Figure 3.2 a). Ice particles grow into large, dense and almost spherical shaped particles. In terms of conical graupel the resulting particles get slightly prolate [30]. Because of the sensitivity of the reflectivity to the hydrometeor size, $Z_{hh} \sim \int D^6 N(D) dD$ where $N(D)$ is the hydrometeor size distribution and D is the equivolumetric diameter, the growth of particles is strongly

Table 3.1: Specifications of the TARA radar during the ACCEPT campaign.

Radar		
Type	FM-CW	
Central frequency	3.298 GHz	S-band
Transmitted power	100 W	Automatic decrease by step of 10 dB in case of receiver saturation
Signal generation		
Sweep time	0.5 ms	
No. of range bins	512	
Range resolution	30 m	Height resolution = 21.2 m
Time resolution	2.56 s	
Polarimetry		
Polarisation	VV HV HH	Main beam only
Measurement cycle	VV HV HH OB1 OB2	Main beam + 2 offset beams
Doppler		
No. Doppler bins	512	
Doppler resolution	0.036 m s^{-1}	
Max. unambiguous vel.	±9.1 m s^{-1}	
Max. vel. main beam	±45.5 m s^{-1}	After spectral polarimetric dealiasing [28]
Max. vel. offset beams	±45.5 m s^{-1}	After spectral dealiasing
Antennas		
Beam width	2.1°	
Gain	38.8 dB	
Near field	≤ 200 m	
Beams	Elevation	Azimuth (North= 0°)
Main beam	45°	246.5°
Offset beam 1	60°	246.5°
Offset beam 2	43.1°	267.3°
Clutter suppression		
Hardware	Antennas	Low side lobes
Processing	Doppler spectrum	Spectral polarimetry (main beam)

connected to an increase of reflectivity. The differential reflectivity Z_{DR} gives information on the shape of the measured particle population (positive = oblate, ≈ 0 dB spherical, and negative = prolate particle shape). The conceptual change in particle shapes is indicated by the dotted lines in Figure 3.2. Thus, rimming processes affect Z_{DR} values by turning horizontally aligned ice particle ($Z_{DR} > 0$) into near spherical (Z_{DR} around 0) or slightly prolate particle ($Z_{DR} < 0$) for conical graupels.

- *Water vapor diffusional growth of ice particles*: occurs when water vapor diffuses towards the crystals instead of forming supercooled droplets, see Figure 3.2 b). During that process particles grow, therefore the reflectivity increases. During the diffusional growth particles keep their characteristic shape, [1, 2, 29]. Their Z_{DR} values slightly increase during the growth process. If particles grow large enough the crystals start to aggregate what again lead to a decrease of polarimetric signature.

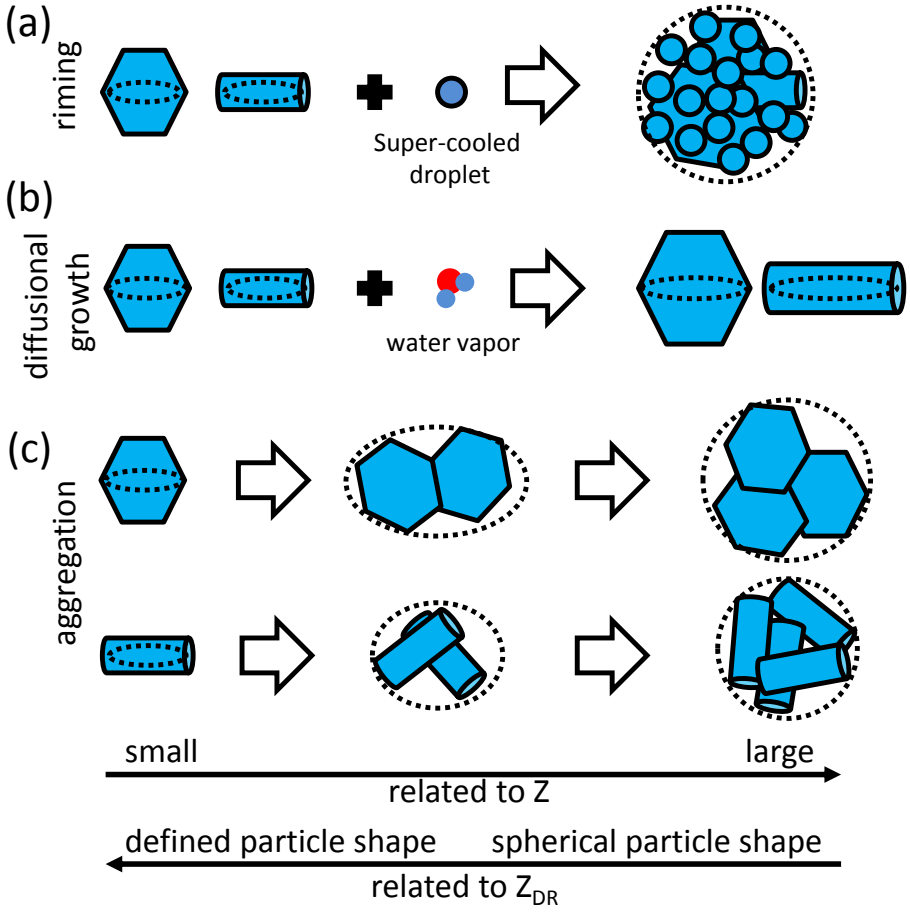

Figure 3.2: Sketch of ice particle growth processes within mixed-phase clouds. In a) riming of ice crystals is depicted. b) shows the diffusional growth of ice crystals and c) the aggregation of ice crystals. The hexagonal plates and cylindrical columns represent either plate and dendrite shape or needles and columns, respectively. Size growth is indicated with bigger particles in the sketch. In the measurements an increase in particle size is related to an increase in Z values, indicated by the first arrow at the bottom. The particle shapes are indicated by the dotted ellipses (the particles are modeled as spheroids). The second arrow at the bottom indicates the decrease of Z_{DR} as an indicator for the decrease of defined particle shape with increasing size.

- *Aggregation of ice particles*: occurs when ice crystals collide and form bigger ice crystals, see Figure 3.2 c). Aggregation leads to an increase of ice particle size and a change in particle shape from pristine particles to spherical shaped ice particles. The decrease of the differential reflectivity signatures depends strongly on the aggregated pristine particle type. Moisseev *et al.* [14] reported that early aggregates of dendrites align horizontally and therefore can also contribute to a high Z_{DR}-signature. This leads to a less strong decrease of polarimetric signatures of Z_{DR} with increasing size of the grown aggregates. Hobbs *et al.* [31] reported that needles have the tendency to clump very fast into spherical particles if their number concentration is high enough. Therefore, needles that aggregate turn faster into spherical shaped particles than dendrites.

3.4. SIGNATURES OF ICE PARTICLE GROWTH IN SPECTRAL RADAR OBSERVATIONS

The main three ice particle growth processes, riming, diffusional growth and aggregation [1, 2] result in different signatures in the spectral radar observations, see Figure 3.3. Identifying the growth process signatures in the Doppler spectrum, sZ, and differential reflectivity spectrum, sZ_{DR}, is challenging due to concurrent growth process mechanisms occurring within the same resolution volume on different group of particles. Therefore, the signatures of different processes can be overlaid and difficult to separate.

Figure 3.3 a) sketches riming signatures in the Doppler spectrum, sZ (black line), and differential reflectivity spectrum, sZ_{DR} (red line). A Doppler spectrum represents the Doppler velocity distribution weighted by particle backscattering. Therefore, sZ and sZ_{DR} are related to the particle size distribution (negative velocities indicate particle movements towards the radar, therefore, larger particles are associated with larger negative velocities), while sZ_{DR} is related to the particle shape distribution. In a Doppler spectrum, a separated particle mode of larger and denser ice particles is often a clear indication of a riming process [3, 11, 30]. As described in Figure 3.3 a) they form a separated particle mode in the Doppler spectrum (left side) that indicates larger particles fall velocities in comparison to already existing particle mode. The particles in the mode on the right side are growing. Ice crystals must have a certain size to be effective to rime [34, 35]. Due to the fast growth of already large ice crystals the reflectivity values are also quite large in the right riming mode. Because not all ice crystals fulfill this criteria and might grow due to diffusional growth and/or aggregation, in the left mode the reflectivity also increases. In comparison to sZ_{DR} values measured in rain, where the oblateness of large rain drops produces the highest sZ_{DR} values, well defined shapes of pristine crystals are mainly responsible of the sZ_{DR}-signatures in cloud. Riming of particles leads to a decrease of polarimetric signatures and a decrease of the sZ_{DR} values towards zero. In case that riming leads to conical graupel sZ_{DR} values become negative (see dotted red line at the left particle mode). In the right mode, a clear shape-size dependence is still expected and the higher sZ_{DR} values corrrespond to the smaller ice crystals that have kept their pristine ice crystal shape.

Figure 3.3 b) depicts a signature of diffusional growth in sZ and sZ_{DR}. The small particle mode on the right side in the Doppler spectrum indicates the diffusional growth of

the ice particles. The Doppler spectrum width increases due to the aggregation mode of the larger particles. Particles that grow via water vapor diffusion keep their pristine crystal shape and, therefore, the sZ_{DR}-values of that mode stay large. The onset of aggregation is seen in the significant decrease of values in the sZ_{DR} spectrum, because aggregation leads to more spherical shaped particles. A significant feature of the diffusional growth is the separated mode in the sZ_{DR} spectrum. Such a mode of defined particle shapes is not present during the aggregation process of particles.

Figure 3.3 c) illustrates an aggregation signature of ice crystals in sZ and sZ_{DR}. Due to the domination of the large particles in the signal the spectral reflectivity can be skewed

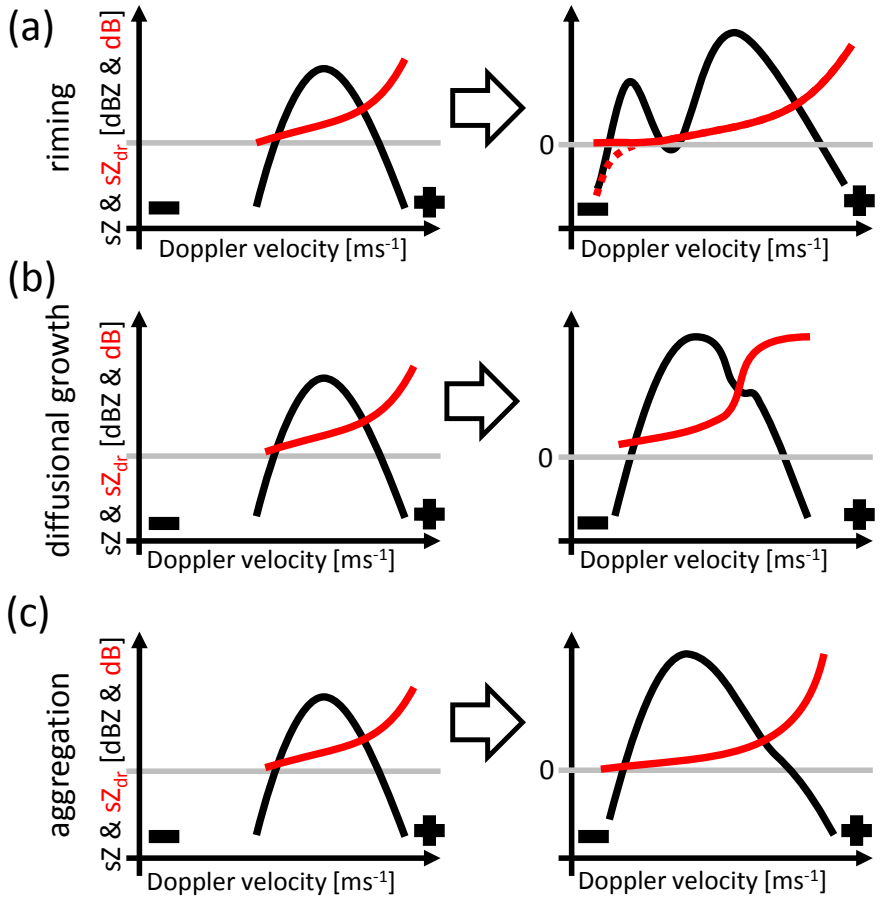

Figure 3.3: Sketch of signature of (a) riming, (b) diffusional growth, and (c) aggregation of ice particles and their corresponding changes in the Doppler spectra sZ (black lines) and spectral differential reflectivity sZ_{DR} (red lines). All sketches represent theoretical dependencies, the gray line indicates 0 dB for the sZ_{DR} values. The Doppler velocity values are relative values (left: minus sign: large negative Doppler velocities; right: plus sign; very small or positive Doppler velocities; negative Doppler velocities indicate movements towards the radar). Conceptional sketches are based on spectral simulations of Oue *et al.* [30], Spek *et al.* [32], Dufournet and Russchenberg [33].

towards bigger particles. Depending on the particle size distribution a separation of the different particles modes is not always possible in the Doppler spectrum. Therefore, the signatures in sZ_{DR} are needed to separate the different particle modes in the spectral domain if they are present. Nevertheless, it has to be mentioned that the differential reflectivity is also influenced by the density of the measured particles. Therefore, the strong decrease of sZ_{DR} signature due to aggregation onset can be caused also by the lower density of the aggregates, compared to the pristine crystals.

The shown signatures in the spectral domain are used to identify qualitatively particle growth within mixed phase clouds. Using bulk and spectral polarimetric measurements, several cases during a complex precipitation system will be investigated next.

3.5. METHODOLOGY

The aim of this study is to analyze the microphysical process of a particle population on its way from cloud top to the bottom of the cloud system. Therefore, radar data are rearranged along so-called fall streaks before their signatures are examined. This offers a new insight on ice growth processes occurring in complex, local and inhomogeneous cloud conditions in precipitating cloud systems.

Marshall [36] and Browne [37] were the first that analyzed fall streak signatures within radar measurements. They investigated the structure and shape of outstanding reflectivity patterns within radar measurements. They described a fall streak like Yuter and Houze [38], as a manifestation of an inhomogeneity in the microphysical structure of a cloud system. To be observed, the relative size and number of precipitation particles within the fall streak need to be large such that their radar reflectivity stands out as a local maximum from the immediate background reflectivity. Nevertheless, it was already pointed out that the main shape and structure of the fall streaks is influenced by the present cloud dynamics [36, 37]. Because of this dynamical influence on the fall streak shape and structure, Pfitzenmaier *et al.* [19] defines a fall streak as the path of a particle population obtained from the observation of its own motion. Taking into account the dynamical conditions within the cloud system the fall streak retrieval is based on the mean 3D wind field retrieved by TARA. Therefore the fall streak retrieval is based on radar Doppler measurements only.

Using directly measured 3D wind information (vertical Doppler velocity vd_V, horizontal wind speed vd_h, and wind direction ϕ_W) the fall streak retrieval estimates the time displacement per height to reconstruct the path of a particle population. This is done using a bottom-up approach starting at the lowest (closest to the ground) valid data point at starting time t_0. The time displacement at the height z is in principle estimated following Equation 3.1. It consists of two terms:

$$\Delta t(z) = t_0(z_0) + \sum_{z_0}^{z} \Delta t_\alpha(z_i) + \sum_{z_0}^{z} \Delta t_{dyn}(z_i) \tag{3.1}$$

The first term is the displacement time related to the antenna elevation, Δt_α. The second term is the displacement time due to the cloud system dynamics, Δt_{dyn}. The calculation of the displacement contributions Δt_α and Δt_{dyn} is done following the steps of Pfitzenmaier *et al.* [19]. The initial condition for the retrieval algorithm (cloud base height and

averaging time for the wind profiles) are set individually per case, applying the suggested method in Pfitzenmaier *et al.* [19].

The microphysical analyzes of the cases are based on fall streak corrected bulk parameter profiles of reflectivity, Z, differential reflectivity, Z_{DR}, and the co-polar correlation coefficient ρ_{HV} as well as on the fall streak corrected Doppler spectra, sZ, and spectral differential reflectivity, sZ_{DR}. The growth of the measured particle population is indicated by an increase of reflectivity. Changes in the Z_{DR}-signature give information on the shape and density changes of the measured particle population. The co-polar correlation coefficient ρ_{HV} gives information about particle homogeneity within the measured volume. The closer ρ_{HV} is to 1 the more homogeneous are the particle shapes of the measured particle population. Therefore, changes of those parameters are used to examine the microphysical evolution of the particle population tracked from cloud top to bottom [6, 19, 30]. The analysis of the fall streak corrected spectrograms are used to investigate the changes in the spectra due to microphysical changes of the tracked ice particle distribution. Spectrograms provide Doppler spectra per height bin at each time step (spectral reflectivity versus Doppler velocity and height). Therefore, it is possible to identify the different signatures of riming, aggregation and diffusional growth of different pristine crystals by analyzing their changes in signature (Figure 3.3) from cloud top to bottom.

Due to the variation of small time scale dynamics (horizontal and vertical wind at 45° elevation) on the spectra, the signatures are only analyzed qualitatively. Nevertheless, the changes in the Doppler spectra shape (broadening, modality, and amplitude) with height are detailed enough to provide information about the present particle microphysics. To ensure a good data quality the spectra are averaged over 3 time bins per height (one time bin before and one time bin after the rearranged spectrum are used for the averaging) as well as a 10 dB threshold above the noise level is applied to Doppler bins in the spectra. This removes artifacts at the edges of the spectra due to low SNR. However sZ_{DR} values are still noisy. Therefore the presented and analyzed visible signatures in the spectrograms are also checked manually for consistency over time and height.

3.6. OBSERVATIONS AND RESULTS

Figures 3.4 and 3.5 show measurements obtained with the S-band radar profiler TARA, on 7^{th} November 2014, from 1000 UTC to 1200 UTC. In addition, the fields of reflectivity and linear depolarization ratio from the co-located vertical profiling cloud radar Mira are presented in Figure 3.4 a) and d), respectively. The reflectivity (Z) fields in Figure 3.4 a) and b) display a precipitating cloud system. The band of enhanced Z values around 2.2 km indicates the melting layer of this frontal system. The attenuation due to precipitation is clearly visible for the 35 GHz radar Mira, comparing the Z fields of both radars (e.g. case 1 and 3 with differences in Z above the melting layer up to 20 dBZ). The Z fields in the cloud part show a high variation. Variability in the structure of the fields of differential reflectivity (Z_{DR}) and linear depolarization ratio (L_{DR}) are also visible in Figure 3.4 c) and d). They have a high correlation with the visible fall streak signatures in the Z-field (e.g. 1030 UTC - 1130 UTC above 4 km). Unfortunately, the TARA obtained wind fields between 1030 UTC and 1120 UTC are corrupted (due to clutter in the

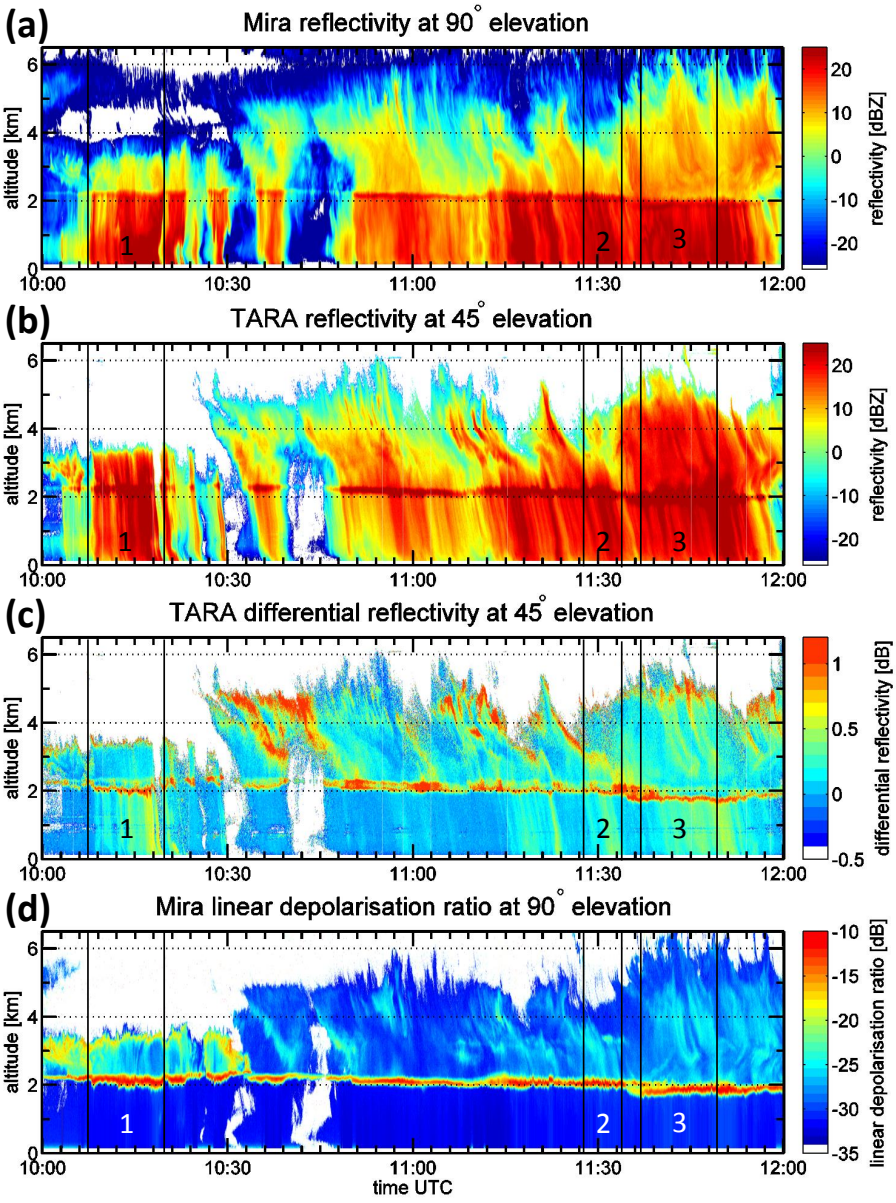

Figure 3.4: Overview of the radar measurements used in this paper. b) and c) show reflectivity and differential reflectivity measurements, obtained with TARA radar (S-band). a) and d) show the reflectivity and linear depolarization ratio measurements from the Mira radar (K_a-band). The boxes 1 , 2, and 3 highlight the time frames where fall streaks at 101250 UTC, 113331 UTC and 114730 UTC are retrieved and their rearranged data are discussed and analyzed.

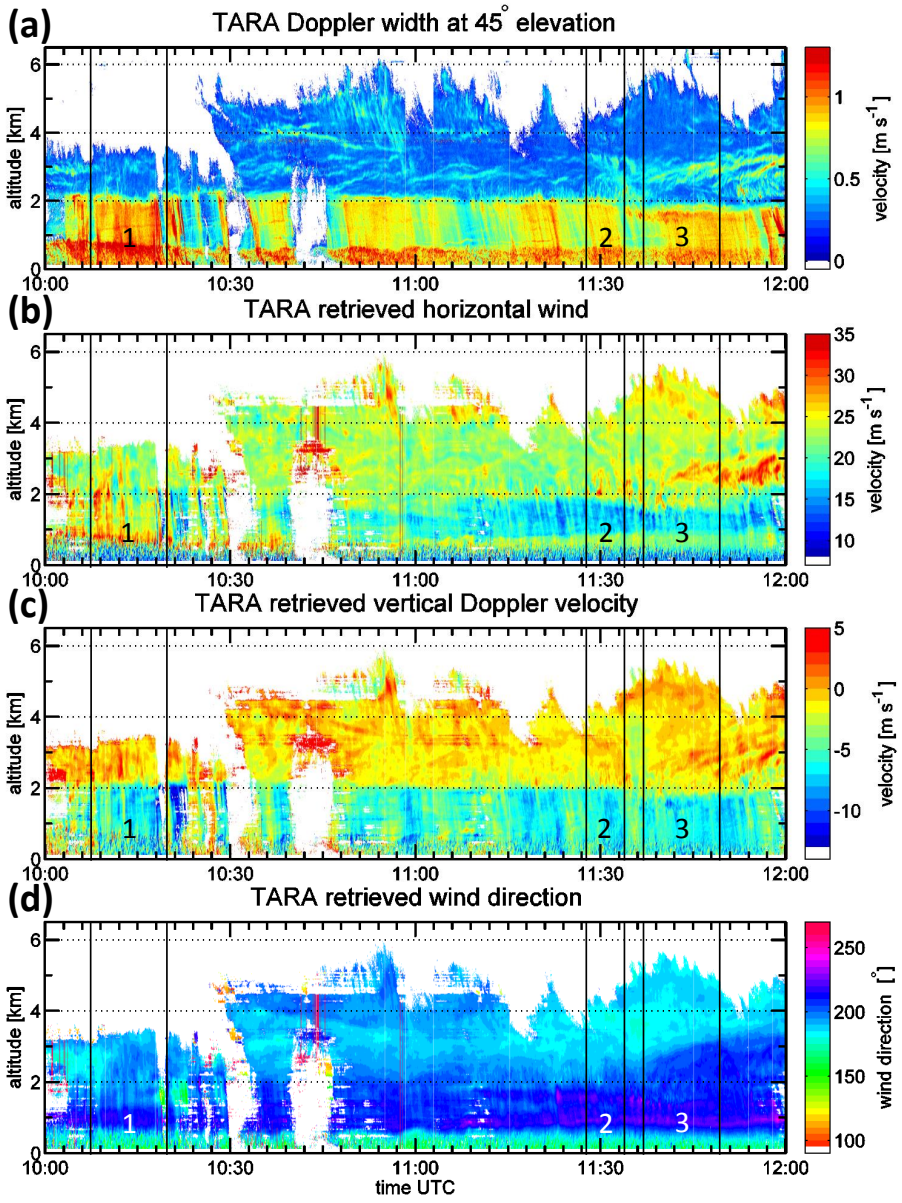

Figure 3.5: Overview of the dynamic variables measured and retrieved by TARA radar (S-band). In a) the Doppler width is displayed, b) shows the retrieved horizontal wind velocity, c) the retrieved vertical Doppler velocity, and d) the retrieved wind direction. The boxes 1, 2, and, 3 highlight the time frames where fall streaks at 101250 UTC, 113331 UTC and 114730 UTC are retrieved, and their rearranged data are discussed and analyzed.

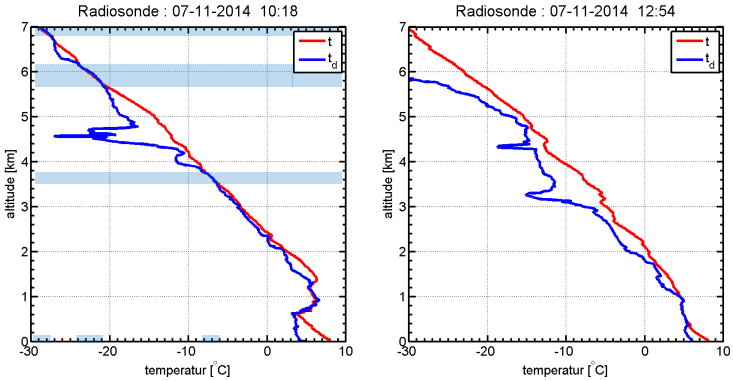

Figure 3.6: Radiosonde launches from the CESAR site at 1018 UTC (left) and after precipitation system has passed at 1254 UTC (right). Displayed are profiles of the temperature t (red) and dew-point temperature t_d (blue). The light blue bars indicate areas where supercooled liquid water was detected with the radiosondes, their corresponding temperature range on the x-axis is highlighted.

non polarimetric offset beam measurements that influenced the retrieved wind fields especially the vertical Doppler velocity component, see Figure 3.5 c)). Therefore, the data analysis is restricted to cases where the wind retrieval quality is good enough to apply the fall streak retrieval technique [19]. Figure 3.5 displays the Doppler spectrum width and wind fields. Besides some small fluctuations in the horizontal wind field, Figure 3.5 b), the measurements show homogeneous wind conditions within the cloud. In the wind direction field, Figure 3.5 d), a shear in wind direction is visible (about 30 ° from 1000 UTC onwards). Later the wind direction shear reaches the cloud part (starting at 1135 UTC). Therefore, enhanced values of vertical Doppler velocity and horizontal wind speed are visible as well as an increase of the Doppler spectral width can be identified. The turbulence is caused by the mixing of an approaching air-mass that is related to a cold frontal cloud system, into the present airmass. Case 1 analyses an example during the enhanced Z_{DR} and L_{DR} signatures on top of the lower cloud layer between 1009 UTC and 1018 UTC. While Case 2 focuses on the band of enhanced Z_{DR} between 1128 UTC and 1133 UTC at around 3 km. For the last case, Case 3, the fall streak structures of Z and polarimetric variables that generated within the enhanced band of Z_{DR} at around 5 km between 1135 UTC and 1147 UTC, are discussed.

3.6.1. CASE 1: AGGREGATION OF NEEDLES, 1009-1018 UTC

With Case 1 the analysis of along a fall streak rearranged S-band radar data is discussed to understand the present particle growth process. Figure 3.7 a) shows the result of a retrieved fall streak at 101251 UTC. The results are obtained using a fixed cloud base height of 2250 m and an averaging window of 30 s for the wind profile as initial conditions for the algorithm [19]. The main features of interest are the enhanced Z_{DR} and L_{DR} signatures near the cloud top of the lower cloud layer (3.75 km to 3.5 km) between 1009 UTC and 1018 UTC in Figure 3.4. The reflectivity during Case 1 increases with decreasing height as quickly as the polarimetric variables change towards a spherical shape depen-

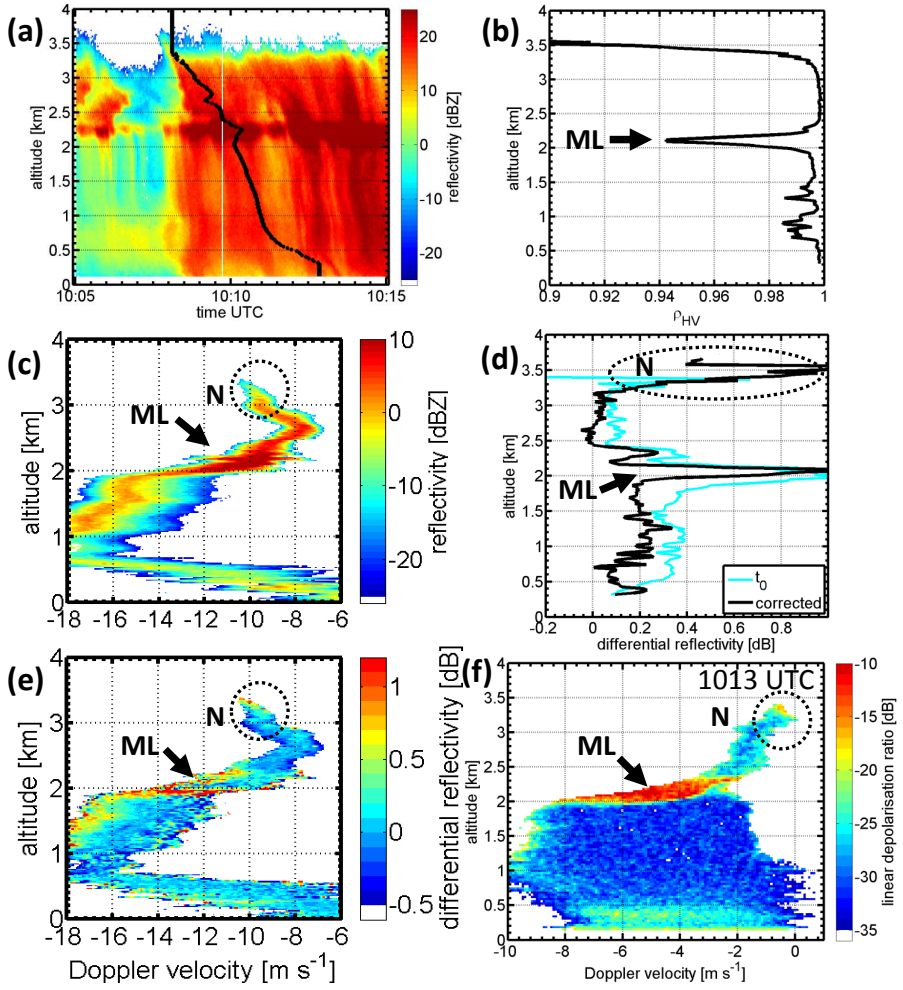

Figure 3.7: a) shows the retrieved fall streak at 101250 UTC obtained with TARA. c) and e) are the fall streak corrected spectrograms (sZ and sZ_{DR}, 45° elevation - Note that the Doppler velocity contains the radial wind). b) and d) show the fall streak corrected profiles of ρ_{HV} and Z_{DR} in black while light blue represents the vertical Z_{DR} profile at 101250 UTC. f) shows the sL_{DR} spectrogram of the vertical pointing Mira at 1013 UTC (all data displayed in the spectrograms have $SNR > 10$ dB). ML points out the signature of the melting layer and N the signature related to the needle particles.

dent signature. Therefore, a strong growth of particle size from pristine shaped particles into almost spherical particles is assumed to be present. To classify the particle population and the growth process even better the fall streak corrected radar data are analyzed.

The particle growth is visible in the fall streak corrected TARA sZ spectrogram in Figure 3.7 c). The sZ spectrogram shows a mono-modal particle population where sZ maximum increases from $sZ = -7$ dBZ at the top (3.3 km) to $sZ = 10$ dBZ above the melting layer (indicated by ML). The four Doppler spectra examples in Figure 3.9 (left column,

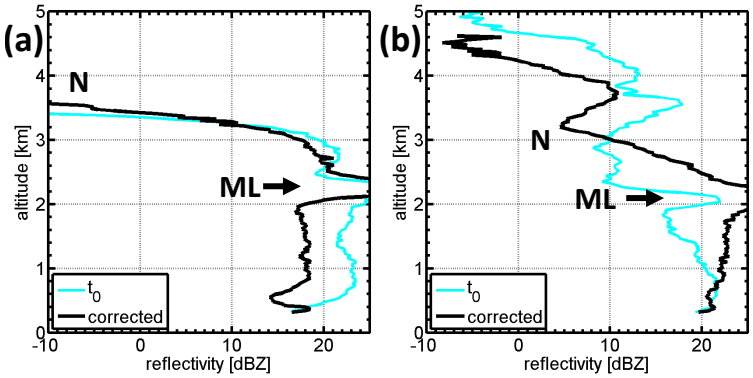

Figure 3.8: a) and b) show the fall streak corrected profiles of Z. a) shows the profiles at 101251 UTC and b) at 113331 UTC. The black line is the fall streak corrected profile and the light blue line represents the vertical profile at the given time. ML points out the signature of the melting layer and N the signature related to needle growth and new generated particle population, respectively.

black spectra) show the evolution from cloud top towards the melting layer. In these examples of Doppler spectra the particle growth is seen by an increase of spectrum peak values and the broadening of the spectrum width with decreasing height. The fall streak corrected Z profile in Figure 3.8 a) (black line) shows a 25 dBZ increase of Z, from cloud top towards the melting layer. In the profile a slight change in the slope at 3 km is visible. While above 3 km the generation and growth of particles are very fast ($\Delta Z \approx 20$ dBZ in 0.6 km) below the increase is less. There the slope shows a slight increasing linear trend towards the melting layer. Such linearity in the reflectivity profile indicates aggregation of particles [39]. Due to the homogeneous cloud conditions the contrast of the along fall streak rearranged and vertical Z profiles (light blue profile) is not huge. A larger difference in the data is only visible in the reflectivity of the rain pattern. Therefore, using fall streak rearranged data in Case 1 has its main importance connecting the cloud microphysics with the rain intensity below.

The decrease of the polarimetric radar signatures in Figure 3.7 e) and f), at N (dotted circles), points out that the ice particles loose their pristine crystal shapes and become spherical particles. Values of sZ_{DR} decreases in the spectrogram from $sZ_{\mathrm{DR}} \approx 1$ dB near 3.25 km to $sZ_{\mathrm{DR}} \approx 0.2$ dB around 3 km. In the spectrograms it is also visible that the particles at all sizes become spherical, below 3 km the maximum values of $sZ_{\mathrm{DR}} \approx 0.2$ dB. In comparison to the schematic sketch of the Z_{DR}-spectrogram in Figure 3.3 c) sZ_{DR} values decrease throughout the whole size range (Doppler velocity range). In Figure 3.9 this is visible in the column of the spectral differential reflectivity (right column, red spectra). At 3.076 km the sZ_{DR} signature versus the whole Doppler velocity range in the spectra is close to zero dB. This observation indicates strong aggregation of particles into spherical ice particles. The fall streak corrected Z_{DR}-profile in Figure 3.7 d) (black line) shows the strong decrease of polarimetric signature from $Z_{\mathrm{DR}} \approx 1$ dB to $Z_{\mathrm{DR}} \approx 0.1$ dB at 3 km. The high values in the ρ_{HV} profile in Figure 3.7 b) exhibit homogeneity of the particles within the measured population. The closer the ρ_{HV} values are to 1 the more homogeneous are the particle shapes in the sampling volume. ρ_{HV} values are constantly above

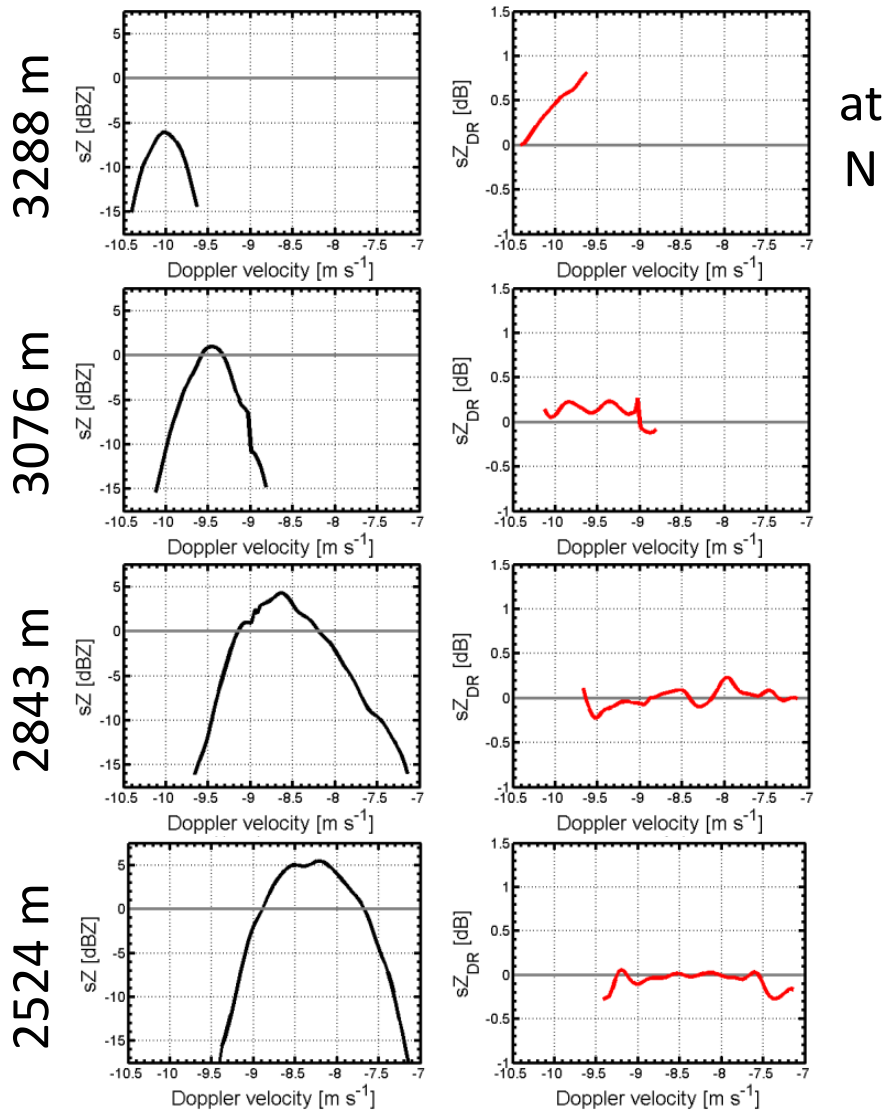

Figure 3.9: Along the fall streak at 101250 UTC rearranged sZ and sZ_{DR} at four different altitudes. The left panel shows Doppler spectra at 3288 m, 3076 m, 2843 m, and 2524 m. The right column displays the corresponding spectral differential reflectivity at the same heights. All spectra are at 45° elevation and averaged over 3 consecutive time bins.

0.9975 below 3 km and therefore match the low Z_{DR}-values and sZ_{DR}-signatures of a homogeneous spherical particle population.

With TARA operating wavelength it is not possible to have a direct signature related to super-cooled liquid water in the Doppler spectra or bulk parameters, additional in-

formation has to be used to detect its presence. The knowledge of the presence of super-cooled liquid water helps in the characterization of the pristine crystal type followed by an even better description of the involved ice crystal growth process. Comparing the observations with the temperature and dew-point-temperature profiles measured by a radiosonde at 1018 UTC (Figure 3.6) a super-cooled liquid water layer at cloud top is identified (light blue shaded area). The detected temperature range of −8°C to −6 °C corresponds to the growth regime of needles at that height [1]. As a second indirect validation the observed sL_{DR} values and signatures in Figure 3.7 f) are used. They are consistent with other observations and simulated sL_{DR} values of needle particles [40–42]. The simulated L_{DR} values span a range from −16 dB to −12.5 dB that is in good agreement with the observed sL_{DR} values in the spectrogram that reach values up to −17 dB in Figure 3.7 f). Therefore, the observed signatures of sL_{DR} and the temperature values indicate the presence of needles at cloud top.

Summing up needles that generated at the cloud top grow fast into a homogeneous population of spherical particles. The fall streak corrected Z-profile, Figure 3.8 a), and the sZ-spectrogram in Figure 3.7 c) show an increase of reflectivity values. The slopes of the Z-profile are consistent with the linear increase of reflectivity in case of aggregation of ice particles into snowflakes, Westbrook *et al.* [39]. In addition the observed Doppler velocities within Mira radar sL_{DR}-spectrogram of $-2\,\mathrm{m\,s^{-1}}$, right above the melting layer also match the expected velocities for aggregates or slightly rimed particles [29, 43]. A strong aggregation or clumping of needle particles is mentioned by Hogan *et al.* [18], Hobbs *et al.* [31], Rangno and Hobbs [44]. The example of sZ_{DR}-spectra in Figure 3.9 shows that such spherical particles can be observed within a short distance below particle generation. These compact and dense particles are more efficient to produce precipitation compared to the ice crystals and snowflakes produced in the time frame before Case 1.

3.6.2. CASE 2: GENERATION OF A SECOND PARTICLE POPULATION, 1128-1133 UTC

The focus of Case 2 is the enhanced Z_{DR} band between 3.2 km and 2.6 km in Figure 3.4 c) and the related microphysical processes that can be identified and connected to its presence. Figure 3.4 b) shows that in parallel the reflectivity values increase below 3.2 km, compared to above, which indicates particle growth. Because the band of enhanced Z_{DR} decreases (particles become more spherical) towards the melting layer a particle growth process can be assumed in Case 2.

In order to go further in the process description, re-arranged fall streaks are additionally retrieved and analyzed. The retrieval is done setting the initial conditions to 2.25 km for the cloud base height and 90 s for the wind averaging. The Z_{DR} profile, Figure 3.10 d) (black), show, at N, the strong increase of the Z_{DR} profile from $Z_{DR} \approx 0.2$ dB at 3.2 km to a maximum of 0.65 dB at 2.9 km which indicates the generation of new particles at that height. From N on towards the melting layer, the Z profile, Figure 3.8 b) (black), shows a linear increase of reflectivity of 15 dBZ that indicates an ongoing aggregation process [39]. The rearranged Z_{DR} profile in Figure 3.10 d) shows also signatures that are in agreement with an aggregation process. Below N, the Z_{DR}-values decrease due to the aggregation of the new generated particles into more spherical shaped particles. It is

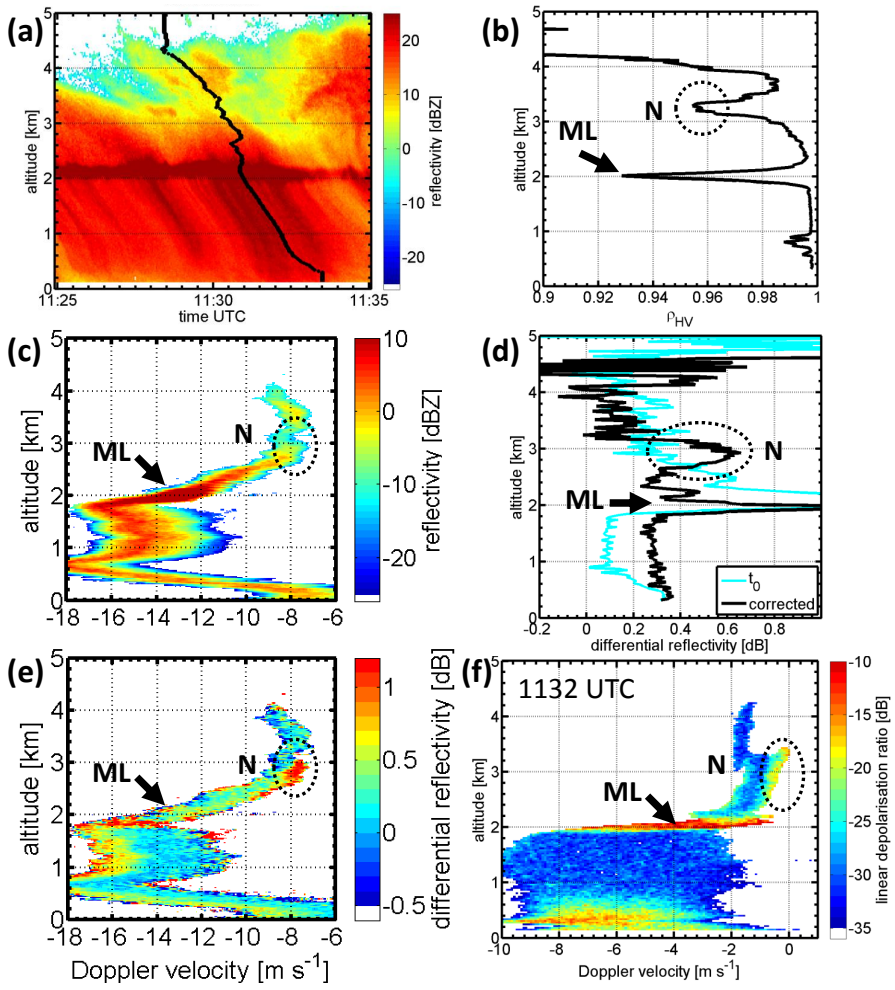

Figure 3.10: a) shows the retrieved fall streak at 113331 UTC on top of the Z field. c) and e) are the fall streak corrected spectrograms (sZ and sZ_{DR}, 45° elevation - Note that the Doppler velocity contains the radial wind). b) and d) show the fall streak corrected profiles of ρ_{HV} and Z_{DR} in black while light blue represents the vertical Z_{DR} profile at 113331 UTC. f) shows the sL_{DR} spectrogram of the vertical pointing Mira at 1132 UTC (all data displayed in the spectrograms have $SNR > 10$ dB). ML points out the signature of the melting layer and N the signature related to the new particle population.

worth noting that such signatures can not be identified in the vertical, not re-arranged, Z and Z_{DR} profiles (light blue profiles in the Figures 3.8 b) and 3.10 d)). This analysis therefore demonstrates the advantage of using along fall streak rearranged radar data, as obtained from Pfitzenmaier *et al.* [19]. Compared to Case 1, the slope of the Z-profile in Case 2 increases much slower at a rate of 15 dBZ per 1km (in Case 1 25 dBZ per 1km). The different slopes of the Z-profiles might indicate different aggregation processes for the two cases. A reason could be that in Case 2 particles seed from above which is not

the case in Case 1, where particles are directly generated at cloud top.

In Figure 3.10 b) the ρ_{HV}-minimum of 0.956 right above the increase of Z_{DR} at 3.2 km indicates the generation of new particles. Due to a high variation of particle shapes (new generated particles, and seeded particles) within the sampling volume the values of ρ_{HV} lead to that minimum. Below 3.1 km, the ρ_{HV} value increases and reaches values > 0.99 below 2.8 km. This increase of ρ_{HV} shows that the particle population becomes more and more homogeneous which indicates an aggregation process.

Next, rearranged fall streak data are analyzed in the spectral domain in order to discriminate between the generated particles at N and the particles seeding from above. The rearranged sZ and sZ_{DR} spectrograms are presented in Figure 3.10 c) and e). At 3.1 km, a broadening is observed in the sZ spectrogram. This broadening of the spectra corresponds to the generation of a second particle mode that is visible a N. The maximum sZ values increase from $sZ \approx -11$ dBZ above N to $sZ \approx 7$ dBZ right above the melting layer. These observations are indicating aggregation of the newly generated crystals towards the melting layer. In Figure 3.10 e) a bimodality is visible in the sZ_{DR}-spectrogram at N. In comparison to the sZ spectrogram the sZ_{DR} spectrogram contains a bimodal shape from N till about 350 m lower. In the sZ-spectrogram such separated modes cannot be identified. Because of the stable second mode in the sZ_{DR} spectrogram the assumption of an aggregation process below N is adjusted and a separated diffusional growth of the new generated particles can be assumed before they aggregate with the ice particles seeded from above.

The analysis of the single sZ and sZ_{DR} spectra in Figure 3.11 confirms the hypothesis of diffusional growth. Figure 3.11 displays four fall streak rearranged Doppler spectra (sZ, left column, black spectra) and differential reflectivity spectra (sZ_{DR}, right column, red line) at four different heights, 3394 m, 3055 m, 2864 m, and 2630 m. At N, a clear broadening in the sZ spectra is visible that is caused by the development of a second particle mode. With decreasing height, the shape of sZ is again monomodal and its values rise, see sZ at 2864 m, and 2630 m. At 3055 m, it is seen that the newly developed particles at N have high sZ_{DR}-values and the sZ_{DR} spectrum shape turns bimodal. However, in comparison to the sZ that looses its bimodal shape rather quickly the sZ_{DR} maintains it further below. At 2864 m still two particle populations can be identified in the sZ_{DR} spectrum. Between -8.5 m s^{-1} and -7.25 m s^{-1}, high sZ_{DR}-values indicate a large amount of pristine shaped ice crystals, while at Doppler velocities < -8.5 m s^{-1} low sZ_{DR}-values refer to almost spherical crystals in that part of the spectrum. This clearly shows that from N to 2864 m the generated particles keep their shape dependence and, therefore, can be separated using the sZ_{DR} spectrum. In parallel the sZ values increases for Doppler velocities > -8.5 m s^{-1}. Due to this growth sZ looses a clearly visible bimodality that was present at N.

These observed signatures fit to the schematic sketches of the diffusional growth of particles, Figure 3.3 b). The signatures of the sZ and the sZ_{DR} clearly show that particles generated at N grow separately from the particles seeding from above. Due to the clear size dependent growth of the smaller particles we assume a diffusional growth of the newly generated particles. Nevertheless, at lower heights it is seen that the clear separation in the sZ_{DR} spectra disappears. This can be explained by the merging of the two particle populations and, therefore, an aggregation process between the particles, see

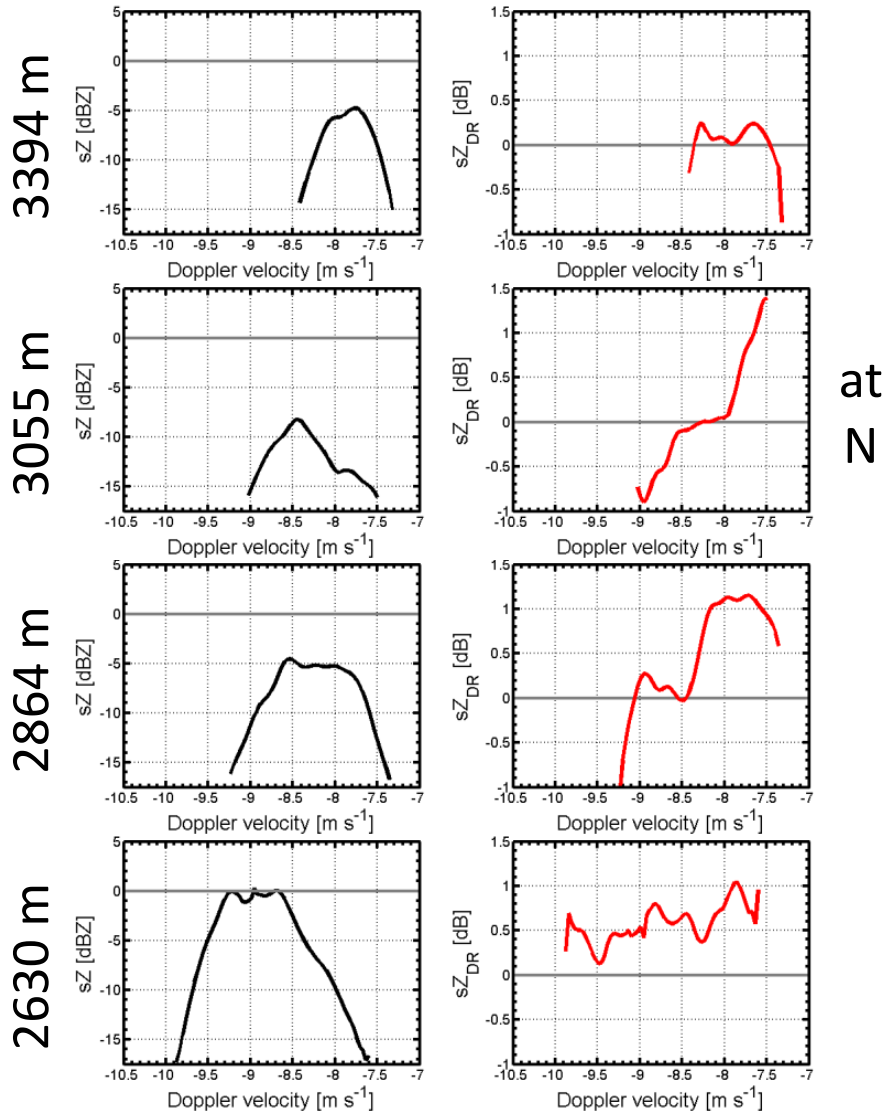

Figure 3.11: Along the fall streak at 113331 UTC rearranged sZ and sZ_{DR} at four different altitudes. The left panel shows Doppler spectra at 3394 m, 3055 m, 2864 m, and 2630 m. The right column displays the corresponding spectral differential reflectivity at the same heights. All spectra are at 45° elevation and averaged over 3 consecutive time bins.

spectra at 2630 m. At N and at 2864 m, the sZ_{DR}-spectrogram shows negative signatures for large ice particles. The values show that the growth at N leads to prolate oriented particles. Super cooled liquid water droplets can lead to partly riming of large particles or turbulence could lead to this prolate orientation. However, with decreasing height

the shape of these particle populations becomes spherical or even slightly oblate again. Nevertheless, the analysis of the along fall streak rearranged spectral data has demonstrated that such processes cannot be identified using integrated volume data. Because using integrated moment data such size dependent spectral signatures are not longer present.

The particle type of the new generated particles can be identified by combining the polarimetric measurements from TARA with additional data from the radiosonde measurements and the sL_{DR}-signatures from the Mira radar. Bands of enhanced Z_{DR} are an indicator for the generation and growth of pristine ice particles, mainly dendrites or hexagonal plates [12, 14, 15]. However, the visible polarimetric signatures in the radar measurements in Case 2 are caused most likely by newly generated ice needles or columns. The temperature ranges of the radiosonde launches in Figure 3.6 show values between $-8°C$ and $-5°C$ at 3 km for both launches. This temperature corresponds to a needle or column generation regime, as in Case 1. In addition the sL_{DR}-spectrogram shows similar signatures with sL_{DR}-values of -17 dB that agree to the simulation signatures for needles or columns [40–42]. Therefore, it is expected that the enhanced Z_{DR} signature is caused by needles or columns. An indication for needle particles can be the presence of a supercooled liquid water layer at that height. Hogan *et al.* [18] showed that small-scale dynamics within frontal system clouds lead to super-cooled liquid droplet formation in the cloud system. Such upward motions are visible in the vertical Doppler velocity field during Case 2 in Figure 3.5, and the hypothesis of needle generation is considered. Nevertheless, in comparison to Case 1, the growth process of the particles is different.

Finally, it is observed, that the new generated particles at 3.1 km and the related growth of ice crystals lead to an increase of Z in the rain pattern below the melting layer. The radiosonde temperature profiles and updraft patterns in the vertical Doppler velocity field show the potentiality for supercooled liquid water layer presence around 3 km. The measured sL_{DR}-signatures show signatures of needle or columnar shaped ice particles. Therefore, the existence of a supercooled liquid water layer is possible. Furthermore, the sZ_{DR}-spectrogram clearly exhibits two different particle populations below this height. The decrease of polarimetric signature in parallel to the increase of Z-values suggest the aggregation of the two present particle populations during Case 2. Deeper analysis of the sZ_{DR} spectra indicate that the mode of smaller particles first grows due to the diffusional growth before merging with the other mode. When these two modes merge, the clear separation disappears and the aggregation of the particles becomes dominant.

3.6.3. CASE 3: GROWTH OF HEXAGONAL PARTICLES, 1135-1147 UTC

Figure 3.12 shows the analysis of the retrieved fall streak from 114730 UTC. The focus of Case 3 is related to the increased Z_{DR} signature at 5 km between 1135 UTC and 1147 UTC. At that height the Z-values increase and indicate a particle growth. The fall streak rearranged data are retrieved using a cloud base height of 2.25 km and a 90 s averaged wind profile. The vertical profiles and fall streak corrected data are only analyzed from cloud top till 3.0 km. This is done because at 3.0 km a strong shear in wind direction is visible in Figure 3.5 d). Therefore, a homogeneous cloud cannot longer be assumed and the along the fall streak rearranged data would describe a different particle population be-

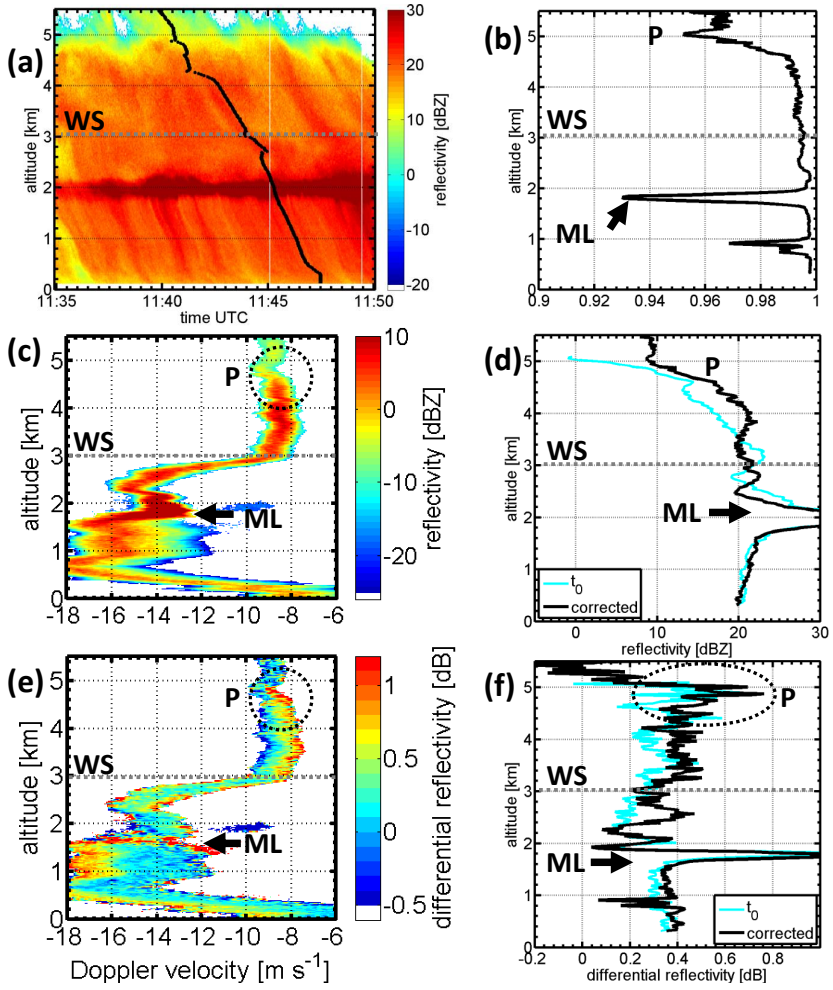

Figure 3.12: a) shows the retrieved fall streak at 114730 UTC obtained with TARA. c) and e) are the fall streak corrected spectrograms (sZ and sZ_{DR}, 45° elevation , all data displayed in the spectrograms have $SNR > 10$ dB - Note that the Doppler velocity contains the radial wind). b), d) and f) show the fall streak corrected profiles of ρ_{HV}, Z, and Z_{DR} in black while the lines in light blue represent the vertical Z and Z_{DR} profiles at 114730 UTC. ML points out the signature of the melting layer and P (black dotted circles) the signature related to the growth process of the particle population under investigation. The dotted line WS indicates approximately the wind direction shear height.

low 3.0 km. So the analysis focuses at regions above 3.0 km and no link to the increased precipitation pattern is done for that case.

The case is anyhow challenging. Because the data above 3.0 km show signatures of aggregation and some indications for riming are found. Therefore, the focus of Case 3 is the identification of the most probable particle growth process.

Figure 3.4 b) depicts a horizontal homogeneous Z-field during Case 3 where the

main increase of reflectivity is visible between 5 km and 4.5 km. In the fall streak corrected sZ spectrogram, Figure 3.12 c) and Figure 3.13, the increase of sZ can be localized at the same height range. There the maximum values of sZ increase from -5dBZ above 5 km to $sZ \approx 6$ dBZ at around 4.5 km ($sZ \approx 7.5$ dBZ at 4 km). The Z-profile in Figure 3.12 d) (black line) shows constant values above 5 km ($Z \approx 10$ dBZ) and below 4 km ($Z \approx 20$ dBZ). The main growth process of the tracked particle population is visible between 5 km and 4 km, where the reflectivity increases linearly of 10 dBZ, which indicates an ongoing aggregation [39]. This signature is consistent with other observations and, therefore, the studies of the microphysics are based on fall streak rearranged TARA data.

The sZ_{DR} spectrogram exhibits a clear shape-size dependency even below the particle growth. The sZ_{DR} signature consists of high values at the right edge where the small particles are present. This signature is constantly present between 4.5 km and 3 km. The maximum values of sZ_{DR} are just below 5 km, $sZ_{DR} \approx 2.25$ dB, sZ_{DR}-spectra at P in Figure 3.13, and decrease with the height. Nevertheless, the shape-size dependency stays. The fall streak corrected Z_{DR} profile in Figure 3.12 f) exhibits a maximum of 0.75 dB between 5.0 km and 4.5 km. Below Z_{DR} values are rather constant around 0.4 dB till 3.0 km. Such a bulk volume is challenging to interpret without the spectral polarimetric measurement.

The profile of ρ_{HV} in Figure 3.12 b) increases with the observed particle growth below 5 km (Z profile) and stays constant from 4.5 km to 3 km. It also exhibits a minimum before the increase around 5 km (slightly above the maximum of Z_{DR}). This is caused by a large variety of particle shapes before the growth, like in Case 2. Below the growth process ρ_{HV} shows a constant value that is 0.05 lower than in Case 2. This is caused by the shape-size relation that is present in the sZ_{DR} spectrogram. Because this signature stays constant till 3 km further growth processes of the tracked particle population like aggregation do not occur.

The constant shape-size dependency within the sZ_{DR} spectrogram between 4.5 km and 3.0 km is the most dominant feature. Comparing these signatures to the schematic sketches in Figure 3.3 we can opt for riming or aggregation of particles. In Figure 3.13 the Doppler spectra do not show a separated mode. Simulations of sZ_{DR} signature indicate that the observed signature at P in Figure 3.13, 4.794 km, can be produced by a mixture of pristine hexagonal shaped ice particles and aggregated or rimed particles [32]. Like in Case 1 and 2, the trend of the sZ_{DR} versus Doppler velocity can be examined, when it is stable for several heights and times. However, caution is required for the values of sZ_{DR} because of their large variance. The absolute values of the Doppler velocities of the Mira spectra (not shown) are below 2 m s^{-1}. They correspond to pristine and slightly rimed particles [43]. Due to the homogeneity of the particle population below 4.5 km in terms of sZ and sZ_{DR} we assume that the particles mainly grow at P and then seed further through the cloud system. Below 4 km the sZ_{DR} spectrogram and spectra in Figure 3.12 e) and Figure 3.13 (right column) show that the larger particles could be prolate. Negative differential reflectivity signatures can be expected for conical graupel presence [30]. However, the observations of [30] indicated that the reflectivity of graupel particles is much higher than in our observations. Riming of particles that lead to prolate particles is also possible but the presence of conical graupel cannot be confirmed. Nevertheless,

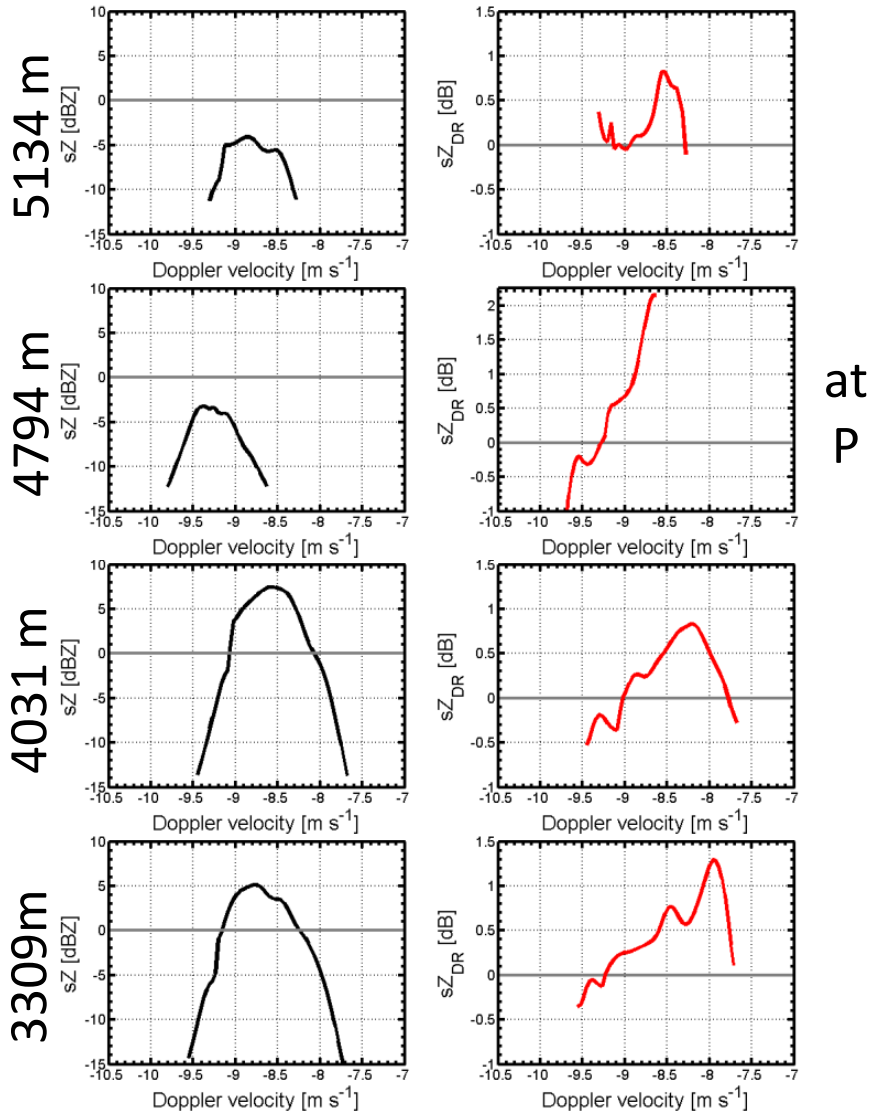

Figure 3.13: Along the fall streak at 114730 UTC rearranged sZ and sZ_{DR} at four different altitudes. The left panel shows Doppler spectra at 5134 m, 4794 m, 4031 m, and 3309 m. The right column displays the corresponding spectral differential reflectivity at the same heights. All spectra are at 45° elevation and averaged over 3 consecutive time bins.

the observed vertical Doppler velocities of the Mira radar are within the expected range for slightly rimed particles. In comparison to the schematic sketches in Figure 3.3 a) no separated particle mode is visible. However, the Doppler spectra at 4031 m, and 3309 m in Figure 3.13 exhibit a small bump where sZ_{DR} signatures are negative. Therefore, a

small amount of rimed prolate oriented particles could be present.

The identification of the dominant particle shape at 5 km can indicate the dominant growth process. Because dendrites and plates have different efficiencies of aggregation and riming [1, 2], the temperature of radiosonde launches is used to identify the possible pristine particle growth regime. In Figure 3.6 both profiles indicate a temperature range between −15° and −13° C, but a direct identification of a super-cooled liquid water layer around 5.0 km cannot be done (dew-point-temperature and temperature profiles do not match at that height). Nevertheless, the temperature range at 5.0 km agrees with the growth regime of hexagonal plates or dendrites [1, 29]. As in Case 2, the vertical Doppler velocity measurements indicate updraft patterns in that region that increases the probability of the presence of super-cooled liquid water droplets [18]. However, from the observations it is not clear which pristine particle shape is dominating the growth process at that height: hexagonal plates or dendrites. Summing up all the facts, the polarimetric measurements, the temperature range, and the updraft patterns we conclude that the presence of supercooled liquid water around P is possible. Because no separated riming mode could be identified in the spectra we do not expect riming to be the dominant particle growth process. It is more likely that the constant reflectivity values and the constant shape-size relationship along the fall streak rearranged data below P are caused by an aggregation process. However, more measurements of the particle microphysics would be necessary to get a more detailed picture on which growth process might dominate in that case.

3.7. DISCUSSION AND CONCLUSION

The high temporal and spatial resolution of profiling S-band radar TARA made it possible to detect and identify structures of particle generation and growth within complicated and dynamically complex mixed-phase cloud systems. Using a S-band radar system has the advantage that the attenuation of the radar signal during precipitation can be neglected compared to higher frequencies operating systems [3]. The unique 3 beam configuration of TARA makes it possible to retrieve the full 3 D wind field for each measurement [27]. Furthermore, this dynamical information is used to retrieve particle fall-streaks within the bulk parameter fields, Pfitzenmaier *et al.* [19]. Therefore, the bulk parameter profiles, Z, Z_{DR}, and ρ_{HV}, as well as spectrograms, sZ and sZ_{DR}, are rearranged along such retrieved fall streak before they are analyzed. Consequently, these corrected spectrograms and profiles show the consistency of the particle growth within the cloud part and relate better to the increase of the rain pattern below the melting layer. Such increased rain patterns are identified during Case 1 and 2.

The analysis of the along fall streak rearranged measurements allows to localize the particle growth process. This can be done by examination of the increase and the slope of Z along the fall streak. Westbrook *et al.* [39] showed that the aggregation of ice crystals leads to a constant increase of Z with decreasing height. The observations were based on averaged data of homogeneous ice clouds over a long time period. Using rearranged data along fall streak such studies can be done in less homogeneous cloud conditions. The presence of super-cooled liquid water leads to a much faster growth of ice particles within a shorter amount of time (fast increase of Z within short height ranges) compared to the growth of particles by aggregation in the ice phase only [1]. That may explain the

increase in the Z profile within 1 km of 25 dBZ in Case 1, 15 dBZ in Case 2, and 10 dBZ in Case 3.

The fall streak corrected sZ_{DR} measurements of TARA are able to deliver shape information and their distribution within the tracked particle population. The changes of the observed signature is in good agreement with the discussed particle growth (increase of Z). However, stable trends of sZ_{DR} should be examined, rather than absolute values because of the large variance of this spectral polarimetric parameter.

In Case 3 the observed polarimetric signature in the sZ_{DR} spectrogram agrees with the simulated sZ_{DR} signature for a mixture of hexagonal plates and rimed particles or aggregates in Spek *et al.* [32]. Therefore, we can opt for riming and/or aggregation of particles in that case. Aggregation is assumed to be the dominant particle growth process. Nevertheless, negative sZ_{DR}-values are observed in the spectrogram, which may indicate rimed prolate oriented particles. However, a typical separated riming mode within the Doppler spectra sZ is not visible. The Mira vertical Doppler velocities fit to the velocity range of slightly rimed particles. Observed updraft patterns indicate the possible presence of supercooled liquid water at the region of the main particle growth, like observed by [18]. Therefore, riming cannot be neglected in Case 3, however, explicit riming signatures cannot be observed in the measured spectra.

The observed signatures of sL_{DR} and sZ_{DR} as well as the measured temperature in Case 1 are in agreement with modeled signatures of needles and their strong tendency to clump and aggregate as reported by [44]. In Case 2 the observed signatures are more complex. While the temperature range can be considered the same as Case 1 the polarimetric signature differs. One reason can be the difference in aggregation efficiency of the new produced particles in these two cases. In Case 2 the needles show a lower aggregation efficiency with the ice particles seeded from above, than in Case 1 where only needles were present. The decrease of the polarimetric signature is less strong than in Case 1. Another reason might be a difference in the particle concentration of the generated particles that is less in Case 2 (sZ of the increased sZ_{DR} mode is less that the sZ values in Case 1). Then the aggregation efficiency is less and the decrease of the sZ_{DR} signature takes longer. Nevertheless, from the observations it is not visible which mechanism is dominant or if they depend on each other. It is only seen that a second population of particles with a high shape size dependency is present in the data. These polarimetric signatures as well as the corresponding temperature profiles indicate the presence of super-cooled liquid water.

Parallel radiosonde launches and the sL_{DR} of the vertical pointing K_a radar Mira are used to compare and verify the results based on the TARA measurements. The cases presented in Section 2.5 are examples of the spectral and bulk parameter characteristics observed during the whole event. These analyzed ice particle growth processes above the melting layer show a strong correlation with increased pattern of precipitation in the reflectivity fields. Therefore, the presented data with applied fall streak correction demonstrate the advantage of using also high resolution S-band radar data to increase the understanding of ice particle growth within precipitating mixed-phase cloud systems.

REFERENCES

[1] H. R. Pruppacher and D. J. Klett, *Microphysics of Clouds and Precipitation* (Springer, 1996) p. 976.

[2] D. Lamb and J. Verlinde, *Physics and Chemistry of Clouds*, edited by geïllustreerd, 1 (Cambridge University Press, 2011) p. 600.

[3] P. Kollias, E. E. Clothiaux, M. A. Miller, B. A. Albrecht, G. L. Stephens, and T. P. Ackerman, *Millimeter-Wavelength Radars: New Frontier in Atmospheric Cloud and Precipitation Research,* Bulletin of the American Meteorological Society **88**, 1608 (2007).

[4] M. D. Shupe, J. S. Daniel, G. de Boer, E. W. Eloranta, P. Kollias, C. N. Long, E. P. Luke, D. D. Turner, and J. Verlinde, *A Focus On Mixed-Phase Clouds,* Bulletin of the American Meteorological Society **89**, 1549 (2008).

[5] M. Oue, M. Galletti, J. Verlinde, A. Ryzhkov, and Y. Lu, *Use of X-Band Differential Reflectivity Measurements to Study Shallow Arctic Mixed-Phase Clouds,* Journal of Applied Meteorology and Climatology **55**, 403 (2016).

[6] H. Kalesse, W. Szyrmer, S. Kneifel, P. Kollias, and E. Luke, *Fingerprints of a riming event on cloud radar doppler spectra: observations and modeling,* Atmospheric Chemistry and Physics **16**, 2997 (2016).

[7] S. Kneifel, A. Lerber, J. Tiira, D. Moisseev, P. Kollias, and J. Leinonen, *Observed relations between snowfall microphysics and triple-frequency radar measurements,* Journal of Geophysical Research (Atmospheres) **120**, 6034 (2015).

[8] A. Myagkov, P. Seifert, U. Wandinger, J. Bühl, and R. Engelmann, *Relationship between temperature and apparent shape of pristine ice crystals derived from polarimetric cloud radar observations during the ACCEPT campaign,* Atmospheric Measurement Techniques **9**, 3739 (2016).

[9] V. N. Bringi and V. Chandrasekar, *Polarimetric Doppler Weather Radar, by V. N. Bringi and V. Chandrasekar, pp. 662. ISBN 0521623847. Cambridge, UK: Cambridge University Press, October 2001.* (2001) p. 662.

[10] J. M. Straka, D. S. Zrnic, and A. V. Ryzhkov, *Bulk Hydrometeor Classification and Quantification Using Polarimetric Radar Data: Synthesis of Relations.* Journal of Applied Meteorology **39**, 1341 (2000).

[11] V. Chandrasekar, R. Keränen, S. Lim, and D. Moisseev, *Recent advances in classification of observations from dual polarization weather radars,* Atmospheric Research **119**, 97 (2013).

[12] P. C. Kennedy and S. A. Rutledge, *S-Band Dual-Polarization Radar Observations of Winter Storms,* Journal of Applied Meteorology and Climatology **50**, 844 (2011).

[13] R. Bechini, L. Baldini, and V. Chandrasekar, *Polarimetric Radar Observations in the Ice Region of Precipitating Clouds at C-Band and X-Band Radar Frequencies,* Journal of Applied Meteorology and Climatology **52**, 1147 (2013).

[14] D. N. Moisseev, S. Lautaportti, J. Tyynela, and S. Lim, *Dual-polarization radar signatures in snowstorms: Role of snowflake aggregation,* Journal of Geophysical Research (Atmospheres) **120**, 12 (2015).

[15] M. J. Bader, S. A. Clough, and G. P. Cox, *Aircraft and dual polarization radar observations of hydrometeors in light stratiform precipitation,* Quarterly Journal of the Royal Meteorological Society **113**, 491 (1987).

[16] J. Andrić, M. R. Kumjian, D. S. Zrnić, J. M. Straka, and V. M. Melnikov, *Polarimetric Signatures above the Melting Layer in Winter Storms: An Observational and Modeling Study,* Journal of Applied Meteorology and Climatology **52**, 682 (2013).

[17] P. R. Field, R. J. Hogan, P. R. A. Brown, A. J. Illingworth, T. W. Choularton, P. H. Kaye, E. Hirst, and R. Greenaway, *Simultaneous radar and aircraft observations of mixed-phase cloud at the 100 m scale,* Quarterly Journal of the Royal Meteorological Society **130**, 1877 (2004).

[18] R. J. Hogan, P. R. Field, A. J. Illingworth, R. J. Cotton, and T. W. Choularton, *Properties of embedded convection in warm-frontal mixed-phase cloud from aircraft and polarimetric radar,* Quarterly Journal of the Royal Meteorological Society **128**, 451 (2002).

[19] L. Pfitzenmaier, Y. Dufournet, C. M. H. Unal, and H. W. J. Russchenberg, *Retrieving fall streaks within cloud systems using Doppler Radar,* Journal of Atmospheric and Oceanic Technology (2017), 10.1175/JTECH-D-16-0117.1.

[20] S. H. Heijnen, L. P. Ligthart, and H. W. J. Russchenberg, *First Measurements with TARA; An S-Band Transportable Atmospheric Radar,* Physics and Chemistry of the Earth B **25**, 995 (2000).

[21] J. Bühl, P. Seifert, U. Wandinger, H. Baars, T. Kanitz, J. Schmidt, A. Myagkov, R. Engelmann, A. Skupin, B. Heese, A. Klepel, D. Althausen, and A. Ansmann, *LACROS: the Leipzig Aerosol and Cloud Remote Observations System,* in *Society of Photo-Optical Instrumentation Engineers (SPIE) Conference Series*, Society of Photo-Optical Instrumentation Engineers (SPIE) Conference Series, Vol. 8890 (2013) p. 2.

[22] U. Görsdorf, V. Lehmann, M. Bauer-Pfundstein, G. Peters, D. Vavriv, V. Vinogradov, and V. Volkov, *A 35-GHz Polarimetric Doppler Radar for Long-Term Observations of Cloud Parameters - Description of System and Data Processing,* Journal of Atmospheric and Oceanic Technology **32**, 675 (2015).

[23] R. Engelmann, T. Kanitz, H. Baars, B. Heese, D. Althausen, A. Skupin, U. Wandinger, M. Komppula, I. S. Stachlewska, V. Amiridis, E. Marinou, I. Mattis, H. Linné, and A. Ansmann, *The automated multiwavelength Raman polarization and water-vapor lidar Polly^{XT}: the neXT generation,* Atmospheric Measurement Techniques **9**, 1767 (2016).

[24] H. Baars, T. Kanitz, R. Engelmann, D. Althausen, B. Heese, M. Komppula, J. Preißler, M. Tesche, A. Ansmann, U. Wandinger, J.-H. Lim, J. Y. Ahn, I. S. Stachlewska, V. Amiridis, E. Marinou, P. Seifert, J. Hofer, A. Skupin, F. Schneider, S. Bohlmann, A. Foth, S. Bley, A. Pfüller, E. Giannakaki, H. Lihavainen, Y. Viisanen, R. K. Hooda, S. Nepomuceno Pereira, D. Bortoli, F. Wagner, I. Mattis, L. Janicka, K. M. Markowicz, P. Achtert, P. Artaxo, T. Pauliquevis, R. A. F. Souza, V. Prakesh Sharma, P. Gideon van Zyl, J. P. Beukes, J. Sun, E. G. Rohwer, R. Deng, R.-E. Mamouri, and F. Zamorano, *An overview of the first decade of Polly^{NET}: an emerging network of automated Raman-polarization lidars for continuous aerosol profiling,* Atmospheric Chemistry & Physics **16**, 5111 (2016).

[25] A. Apituley, K. Wilson, C. Potma, H. Volten, and M. de Graaf, *Performance assessment and application of CAELI, a high-performance Raman lidar for diurnal profiling of water vapour, aerosols and clouds,* (Proceeding of the 8th International Symposium on Tropospheric Profiling, 978-90-6960-233-2 (2009) Delft, The Netherlands, 2009).

[26] D. Moisseev, C. Unal, H. Russchenberg, and V. Chandrasekar, *Radar observations of snow above the melting layer,* in *Third European Conference on Radar Meteorology (ERAD)* (2004) pp. 407–411.

[27] C. Unal, Y. Dufournet, T. Otto, and H. Russchenberg, *The new real-time measurement capabilities of the profiling TARA radar,* in *Article in monograph or in proceedings* (ERAD 2012 - 7th European conference on radar in meteorology and hydrology, Toulouse, France, 24-29 June 2012, 2012).

[28] C. M. H. Unal and D. N. Moisseev, *Combined Doppler and Polarimetric Radar Measurements: Correction for Spectrum Aliasing and Nonsimultaneous Polarimetric Measurements,* Journal of Atmospheric and Oceanic Technology **21**, 443 (2004).

[29] N. Fukuta and T. Takahashi, *The Growth of Atmospheric Ice Crystals: A Summary of Findings in Vertical Supercooled Cloud Tunnel Studies.* Journal of Atmospheric Sciences **56**, 1963 (1999).

[30] M. Oue, M. R. Kumjian, Y. Lu, Z. Jiang, E. E. Clothiaux, J. Verlinde, and K. Aydin, *X-Band Polarimetric and Ka-Band Doppler Spectral Radar Observations of a Graupel-Producing Arctic Mixed-Phase Cloud,* Journal of Applied Meteorology and Climatology **54**, 1335 (2015).

[31] P. V. Hobbs, S. Chang, and J. D. Locatelli, *The dimensions and aggregation of ice crystals in natural clouds,* jgr **79**, 2199 (1974).

[32] A. L. J. Spek, C. M. H. Unal, D. N. Moisseev, H. W. J. Russchenberg, V. Chandrasekar, and Y. Dufournet, *A New Technique to Categorize and Retrieve the Microphysical Properties of Ice Particles above the Melting Layer Using Radar Dual-Polarization Spectral Analysis,* Journal of Atmospheric and Oceanic Technology **25**, 482 (2008).

[33] Y. Dufournet and H. W. J. Russchenberg, *Towards the improvement of cloud microphysical retrievals using simultaneous Doppler and polarimetric radar measurements,* Atmospheric Measurement Techniques **4**, 2163 (2011).

[34] P. K. Wang and W. Ji, *Collision Efficiencies of Ice Crystals at Low-Intermediate Reynolds Numbers Colliding with Supercooled Cloud Droplets: A Numerical Study.* Journal of Atmospheric Sciences **57**, 1001 (2000).

[35] E. E. Ávila, N. E. Castellano, C. P. R. Saunders, R. E. Bürgesser, and G. G. Aguirre Varela, *Initial stages of the riming process on ice crystals,* grl **36**, L09808 (2009).

[36] J. S. Marshall, *Precipitation Trajectories and Patterns.* Journal of Atmospheric Sciences **10**, 25 (1953).

[37] I. C. Browne, *Precipitation streaks as a cause of radar upper bands,* Quarterly Journal of the Royal Meteorological Society **78**, 590 (1952).

[38] S. E. Yuter and R. A. Houze, *Microphysical modes of precipitation growth determined by S-band vertically pointing radar in orographic precipitation during MAP,* Quarterly Journal of the Royal Meteorological Society **129**, 455 (2003).

[39] C. D. Westbrook, R. J. Hogan, A. J. Illingworth, and E. J. O'Connor, *Theory and observations of ice particle evolution in cirrus using Doppler radar: Evidence for aggregation,* grl **34**, L02824 (2007), physics/0608144 .

[40] K. Aydin and T. M. Walsh, *Millimeter wave scattering from spatial and planar bullet rosettes,* IEEE Transactions on Geoscience and Remote Sensing **37**, 1138 (1999).

[41] S. Y. Matrosov, R. F. Reinking, R. A. Kropfli, B. E. Martner, and B. W. Bartram, *On the Use of Radar Depolarization Ratios for Estimating Shapes of Ice Hydrometeors in Winter Clouds.* Journal of Applied Meteorology **40**, 479 (2001).

[42] M. Oue, M. R. Kumjian, Y. Lu, J. Verlinde, K. Aydin, and E. E. Clothiaux, *Linear Depolarization Ratios of Columnar Ice Crystals in a Deep Precipitating System over the Arctic Observed by Zenith-Pointing Ka-Band Doppler Radar,* Journal of Applied Meteorology and Climatology **54**, 1060 (2015).

[43] D. L. Mitchell, *Use of Mass- and Area-Dimensional Power Laws for Determining Precipitation Particle Terminal Velocities.* Journal of Atmospheric Sciences **53**, 1710 (1996).

[44] A. L. Rangno and P. V. Hobbs, *Ice particles in stratiform clouds in the Arctic and possible mechanisms for the production of high ice concentrations,* jgr **106**, 15 (2001).

4

INVESTIGATION OF THE SPECTRAL DIFFERENTIAL PHASE AND SPECIFIC DIFFERENTIAL PHASE IN S-BAND

Abstract: Within the ice phase of cloud systems, the interaction between ice crystals or between ice and supercooled liquid water leads to a variety of ice particle habits and particle growth processes. Understanding these different microphysical processes is important because the ice phase is involved in many processes especially, in the precipitation formation in the mid-latitudes. Nowadays, these processes are still not clearly understood. Polarimetric radar measurements are used to analyze the microphysical processes in precipitating cloud systems. The polarimetric radar variables differential reflectivity, Z_{DR}, differential phase, Φ_{DP}, and specific differential phase, K_{DP}, are used currently to improve rain estimation, hydrometeor classifications, and microphysical processes understanding. Additionally, spectrally resolved radar data have shown to particularly improve the analysis and understanding of cloud microphysical processes. In this paper, the spectral polarimetric measurement capabilities of the Transportable Atmospheric RAdar (TARA, an FMCW S-Band radar profiler) are used to obtain Φ_{DP} and K_{DP} in the spectral domain. In the ice phase of clouds, it was found that on one hand K_{DP} is a good indicator of the onset of aggregation processes. But on the other hand some K_{DP}-signatures might not be visible in the radar moments. Therefore, K_{DP} is processed in spectral domain and its signatures are analyzed and related to microphysical processes. To be able to do this, in this paper, a technique to estimate spectral differential phase and spectral specific differential phase is presented as well as some preliminary results based on radar data are discussed. The variation of microphysical properties make the estimation and especially the interpretation of the spectral-K_{DP} very challenging. Nevertheless, the estimated signals shows some unexpected features that point out that further investigation of the spectral-K_{DP} is necessary to understand this parameter.

4.1. INTRODUCTION

Measuring ice particle microphysical processes is an observational challenge because of the small temporal and spatial scales involved [1–3]. However, the analysis of the ice particle microphysics is important to understand for example precipitation formation processes. Nowadays, ground-based radar measurements are widely used for such observations [1, 4]. Their advanced capabilities make the observation and study of microphysical processes within cloud and precipitation systems possible using a single instrument.

The use of polarimetric radar observables creates new possibilities to study cloud microphysical properties and to develop retrieval techniques [1, 4, 5]. Currently, lower frequency polarimetric variables are mostly used to estimate the amount of precipitation [5, 6]. For liquid precipitation, the differential phase shift, Φ_{DP}, its derivative the specific differential phase shift, K_{DP}, and the differential reflectivity, Z_{DR}, are used to estimate rainfall rates in weather radar systems. Both, Φ_{DP}, and K_{DP}, depend on the number of scatterers in the measured volume and are used to estimate the amount of precipitation [5–7]. The differential reflectivity, Z_{DR}, is related to the raindrop shape. Because of the relationship between the shape and the size of raindrops Z_{DR} values can be related to the raindrop sizes (the larger rain drops are, the more oblate they become) [8]. Further, differences and combinations of polarimetric variables are used to classify hydrometeors [9–12]. There is also an increasing interest in studying microphysical properties of frozen hydrometeors with low-frequency radar systems, thanks to the progress achieved in the measurement quality [13–20]. Frozen hydrometeors are also studied using polarimetric weather radar measurements. Bader *et al.* [13] compared the radar observed Z_{DR} signatures with aircraft in situ measurements of ice crystal habits. It was found that enhanced Z_{DR} values matched well when the aircraft detected pristine ice crystals. Therefore, increased Z_{DR} values can help to detect cloud regions where pristine ice crystals are present. [14, 21] did some simulations of polarimetric signatures for low frequencies radar. These simulations showed that ice crystals can produce significant K_{DP} for low-frequency radars and that these K_{DP} signatures can be related to the ice water content of the cloud system. The combination of Z_{DR} and K_{DP} was found to be a good indicator identifying the growth of hexagonal plate-like ice particles and to determine the onset of the aggregation of these particles [15, 19, 22]. It is also reported that the Z_{DR} and K_{DP} signatures show altitude offset of their signature maxima with respect to each other. These observed offsets are most likely caused by the different sensitivities of these parameters to the maximum oblateness of the observed particles and the maximum of the particle number concentration. Andrić *et al.* [23] simulated Z_{DR} and K_{DP}-signatures to improve the understanding of these parameters and their offset in the observed signatures. The simulations showed agreements with the observations. Nevertheless, not all simulated features matched the observations.

The use of spectral resolved radar measurements can even improve the observation and estimation of ice microphysical processes. In the spectral domain different microphysical processes and ice particle populations can be identified in the same sampling volume [4, 20]. Main reason is the decomposition of the measured signal in the volume versus the corresponding Doppler velocity of measured hydrometers. Therefore, the different spectral signatures can be related via the corresponding Doppler velocity values

to different hydrometer microphysical properties. Analyzing the changes of these signatures over time it is further possible to identify different microphysical cloud processes. Oue *et al.* [16] used Doppler spectra, spectral linear depolarizations ratio spectra, and K_{DP}-signatures to analyze an event of graupel formation in Arctic mixed-phase clouds. Kalesse *et al.* [24] analyzed the modes and other features of Doppler spectra to identify the characteristics of ice particle riming and compared them to simulations of a riming event. The mentioned studies had a focus on ice particle microphysics of cloud systems without melting of the hydrometeors and were based on high-frequency radar observations. In such clouds that include the melting layer and liquid precipitation the signal of high-frequency radars can be attenuated [4]. Therefore, studying the ice particle growth to understand precipitation formation has its limitation in heavily precipitating cloud systems. This is the rationale why an S-band radar like TARA (Transportable Atmospheric Radar; operated by the TU Delft) is used to study such processes although the polarimetric/spectral polarimetric observables may be noisier. TARA can observe ice particle microphysical properties in heavy precipitating systems because of its high spatial and temporal resolution [20, 25, 26]. [25] simulated spectral polarimetric radar variables of ice crystals and demonstrated that signatures of ice crystals could be measured using low-frequency radars. [26] used spectral polarimetric radar data and spectral measurements to retrieve microphysical properties of ice particles. [20] analyzed spectral polarimetric radar data which were rearranged along fall streaks to identify different ice particle growth processes.

The aim of this paper is to present an algorithm for spectral Φ_{DP} and K_{DP} estimation in precipitating cloud systems. Due to the presented processing algorithm the spectral measurement capability of the TARA radar systems is extended and the new spectral derived polarimetric parameters can be used also to analyze microphysical processes in cloud systems and can potentially help identity different microphysical processes. However, the estimation of the spectral Φ_{DP} and K_{DP} procedure is rather challenging. One reason is that already the Φ_{DP} and K_{DP}-values for low-frequency radar systems are low and noisy. To be able to estimate these parameters temporal averaging, a high signal-to-noise ratio, and smoothing techniques are applied during the estimation process. Nevertheless, at high frequencies, the Φ_{DP} has to be corrected for the backscattering differential phase shift contribution to the signal before the K_{DP} can be calculated. At S-band such a correction is not required which simplifies the processing. Theoretical studies point out, that spectral Φ_{DP} and K_{DP} cannot be decomposed versus Doppler velocity. Therefore, the separation of the spectra into contributions of different particle populations might not be possible in the spectral domain. Nevertheless, the spectral processing can be used in the future to improve the estimation of the non spectral Φ_{DP} and K_{DP} or possibly the clutter removal. However, the presented primarily results show spectral signatures versus Doppler velocity in the spectral Φ_{DP} and spectral K_{DP}. The cause of these signatures are not understood. However, one hypothesis might be that the signatures might be caused by variations in the particle microphysics during the averaging period of the measurements. This paper is organized as follows. The TARA radar system and the used data set are described in Section 4.2. An overview of the methodology of polarimetric radar measurements as well as the spectral K_{DP} interpretation is given in Section 4.3. The data processing algorithm is presented in Section 4.4. In the Section 4.5 the study

case is introduced and in Section 4.6 the results of data processing are presented. Limitations and assumption of the presented processing technique is discussed in Section 4.7, and in Section 4.8 conclusions are given.

4.2. INSTRUMENTATION AND DATA SET

4.2.1. THE ATMOSPHERIC TRANSPORTABLE RADAR - TARA

TARA is a frequency modulated continuous wave (FM-CW) S-band radar profiler (3.3 GHz, $\lambda = 0.091$ m). TARA has full polarimetric and Doppler capabilities. The TARA radar system provides high-resolution column measurements in the Doppler domain (0.03 m s^{-1}), in range (30.0 m, max. range of 15.36 km) as well as high temporal resolution (2.56 s). All the measurements are performed under a fixed antenna elevation (45°) and a fixed azimuth (246.5° related to the North, counted clockwise). Measurements performed at 45° elevation are considered as an optimum to get polarimetric and Doppler spectra information related to microphysical properties of the probed medium [27, 28]. TARA measures reflectivity, Z, differential reflectivity, Z_{DR}, linear depolarization ratio L_{DR}, co-polar correlation coefficient, ρ_{HV}, and differential phase shift, Φ_{DP}. The specific differential phase shift, K_{DP}, is calculated as a range derivative from Φ_{DP}. Because of the spectral configuration of TARA all the parameters can also be processed in the spectral domain (sZ, sZ_{DR}, $s\Phi_{DP}$, sK_{DP}). These spectra can also be analyzed along a vertical profile they form thus a spectrogram (height profiles of spectral parameters). These spectrograms are analyzed focusing on changes in their signatures that are caused by changes in the cloud microphysics. Therefore it is possible to identify separate particle modes within the spectra (having different intensities over the velocity range) in the sZ and sZ_{DR} spectra [20].

4.2.2. THE ACCEPT CAMPAIGN

The presented data were obtained during the ACCEPT campaign (Analysis of the Composition of Clouds with Extended Polarization Techniques). The measurements were performed from October to November 2014 at the Cabauw Experimental Site for Atmospheric Research (CESAR), the Netherlands. During the campaign, the TARA radar was collocated with an extended setup of the Leipzig Aerosol and Cloud Remote Observation System (LACROS) [29], as well as other additional sensors. Table 4.1 gives an overview over the specifications of TARA during ACCEPT. The aim of the ACCEPT campaign is to understand the microphysical processes involved in mixed phase clouds at high resolution, temporal and spatial. One focus was to improve the understanding of ice crystal formation at the top of single layer mixed-phase clouds [2]. Another aim was to improve the understanding of ice particle growth when ice crystals interact with the present super-cooled liquid water embedded within the cloud systems [20]. [31] used the obtained data set to retrieve microphysical properties of liquid cloud and drizzle droplets.

4.3. METHODOLOGY

The aim of this study is to develop an algorithm that can process the differential phase shift, Φ_{DP}, and the specific differential phase shift, K_{DP}, in the spectral domain. The

Table 4.1: Specifications of the TARA radar during the ACCEPT campaign.

Radar		
Type	FM-CW	
Central frequency	3.298 GHz	S-band
Transmitted power	100 W	Automatic decrease by step of 10 dB in case of receiver saturation
Signal generation		
Sweep time	0.5 ms	
No. of range bins	512	
Range resolution	30 m	Height resolution = 21.2 m
Time resolution	2.56 s	
Polarimetry		
Polarisation	VV HV HH	Main beam only
Measurement cycle	VV HV HH OB1 OB2	Main beam + 2 offset beams (for wind measurements)
Doppler		
No. Doppler bins	512	
Doppler resolution	0.036 $m\,s^{-1}$	
Max. unambiguous vel.	$\pm 9.1\ m\,s^{-1}$	
Max. vel. main beam	$\pm 45.5\ m\,s^{-1}$	After spectral polarimetric dealiasing [30]
Max. vel. offset beams	$\pm 45.5\ m\,s^{-1}$	After spectral dealiasing
Antennas		
Beam width	2.1°	
Gain	38.8 dB	
Near field	≤ 200 m	
Beams	Elevation	Azimuth (North= 0°)
Main beam	45°	246.5°
Offset beam 1	60°	246.5°
Offset beam 2	43.1°	267.3°
Clutter suppression		
Hardware	Antennas	Low side lobes
Processing	Doppler spectrum	Spectral polarimetry (main beam)

analysis of $s\Phi_{DP}$ and sK_{DP} spectra provides additional information and may improve the identification and study of ice particle microphysical processes, e.g., the onset of aggregation of ice particles. The use of Φ_{DP} and K_{DP} in combination with the differential reflectivity, Z_{DR}, was found to be a good indicator for the growth of hexagonal plate-like particles and the onset of aggregation of these ice crystals within the cloud [13, 15, 19, 23]. The reason for that is that the polarimetric radar variables, Z_{DR}, Φ_{DP}, and K_{DP} have

different sensitivity to microphysical properties of ice crystals.

- The reflectivity, Z, is related to the particle number concentration and $Z \sim D^6$, where D is the particle diameter. Therefore, the integrated Z has a strong dependency on particle size and is weighted towards the large particles in the sampling volume. Changes in the number concentration of particles can be identified analyzing changes in the sZ-slope versus height.

- The differential reflectivity, Z_{DR} depends on the axis ratio and density of the measured ice particles in the sampling volume. The value of $Z_{\mathrm{DR}} > 0$ dB for oblate particles, $Z_{\mathrm{DR}} \approx 0$ dB for spherical particles, and $Z_{\mathrm{DR}} < 0$ dB for prolate particle shapes or particle orientations. Although, the Z_{DR} is independent of the total particle number concentration, the integrated Z_{DR} value is weighted by reflectivity and, therefore, weighted towards larger and averaged spherically shaped particles. This effect leads to a masking of Z_{DR}-signatures caused by regular shaped pristine ice crystals that might be present in the sampling volume. Aggregates can cause a decrease of Z_{DR} because the bulk densities of aggregates are lower than the one of pristine ice crystals. Nevertheless, [19] demonstrated based on simulations and observations that early aggregates can produce Z_{DR}-values that are significant and can be detected by radars, although their bulk density gets lower.

- The differential phase shift, Φ_{DP}, is a range cumulative quantity and related to number concentration, the axis ratio or orientation and density of particles in the sampling volume. Φ_{DP} increases in regions with a large number of horizontally aligned particles. In rain, Φ_{DP} has generally increasing positive value. In the cloud part, Φ_{DP} can have negative values because of prolate oriented ice particles [9, 10].

- As the Φ_{DP}, the specific differential phase shift, K_{DP}, is also related to the particle number concentration, $N(D)$, the axis ratio r_a or orientation, and particle bulk density, ρ_p, of the measured particles in the sampling volume (Bringi and Chandrasekar [5], Chapter 7)

$$K_{\mathrm{DP}} = \frac{\pi}{\lambda}\, C_{bc} \int \frac{\pi}{6}\, \rho_{\mathrm{p}}^2\, D^3\, (1 - r_a)\, N(D)\, dD. \tag{4.1}$$

  where C_{bc} is a constant containing the ice crystal scattering characteristics in the Rayleigh regime, λ is the radar wavelength, and D the particle diameter. In the equation 4.1 it is seen that K_{DP} raises with increasing number concentration, larger ice particle bulk density, and decreasing axis ratio. Negative K_{DP} values can be caused by prolate ice particle shapes or prolate oriented ice crystals. Because the K_{DP} value is influenced by three microphysical parameters, the interpretation of this parameter is challenging. To be able to interpret K_{DP} in ice clouds also a high SNR ratio of the data is needed. Oue *et al.* [16] showed that the low number concentration of ice crystals in Arctic clouds might decrease the quality of K_{DP} and, therefore increases the standard deviation of the values.

- Theoretical studies show that the spectral phase shift, $s\Phi_{\mathrm{DP}}$, cannot be decomposed versus Doppler velocity (communication with C. Unal). Therefore, from the

theoretical point of few $s\Phi_{DP}$ is supposed to be a constant and a flat line along the Doppler velocity range and as a consequence of that sK_{DP} as well. However, the later presented $s\phi_{DP}$ and sK_{DP} spectra show signatures along the Doppler velocity range. These signatures are discussed and investigated further in the Sections results and discussion.

4.4. PROCESSING OF SPECTRAL DIFFERENTIAL PHASE, $s\Phi_{DP}$, AND SPECTRAL SPECIFIC DIFFERENTIAL PHASE, sK_{DP}

As mentioned before, the estimation of the spectral differential phase, $s\Phi_{DP}$, and the spectral specific differential phase, sK_{DP}, is challenging and during the processing lots of steps have to be taken into account to obtain good quality results. Due to the used frequency, the values to estimate are small and noisy. Also, the significant dependence of the K_{DP} to ice particle microphysical properties makes the interpretation of results a challenge. Figure 4.1 illustrates all the steps taking into account during the estimation procedure. The algorithm is explained in detail in the following sections.

4.4.1. sK_{DP}-RETRIEVAL STEP 1 - SHIFT OF THE SPECTRA TO vd_0

Before the averaging, the spetra are shifted along the Doppler velocity axis in order to have their mean Doppler velocity equal to 0 $\mathrm{m\,s^{-1}}$. This is done to minimize the influence of wind variations during the averaging period. The horizontally polarized, sZ_{HH}, and the vertical polarized Doppler spectra, sZ_{VV}, as well as the cross-spectrum, sF_{HV}, have the same Doppler velocity shift.

$$sF_{HV}(r,v) = \widehat{S}_{HH}(r,v)\,\widehat{S}^{*}_{VV}(r,v), \tag{4.2}$$

where v is the measured Doppler velocity, r the range and $\widehat{S}$ the scattering Matrix in the Doppler domain.

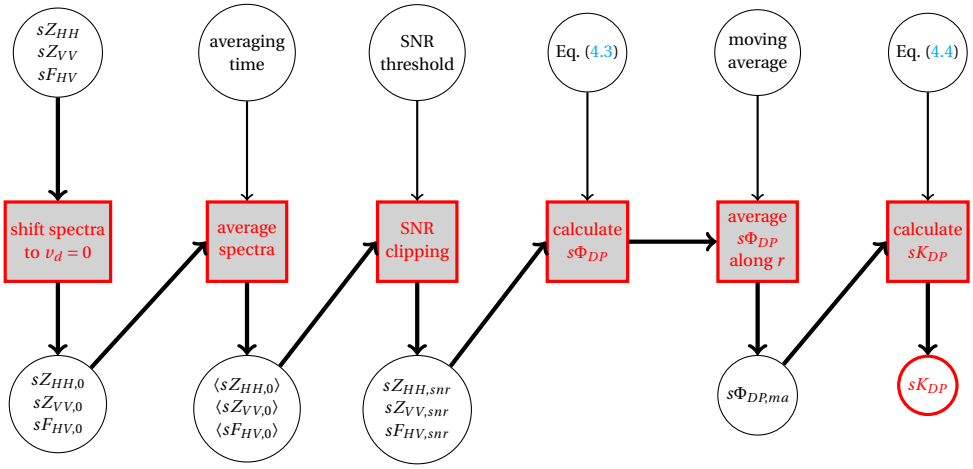

Figure 4.1: Flowchart of the $s\Phi_{DP}$ and sK_{DP} processing chain

4.4.2. sK_{DP}-RETRIEVAL STEP 2 - AVERAGE SPECTRA IN TIME

In this step the spectra are averaged in time. The averaging is important because in general Φ_{DP} is a very noisy parameter. Also the Φ_{DP} values are low at S-band [5]. Therefore, the preprocessing increases their quality and the averaging in time increases the Signal-to-Noise-Ratio (SNR) of the spectra.

4.4.3. sK_{DP}-RETRIEVAL STEP 3 - APPLY SNR THRESHOLD

In the third step, a SNR-clipping is applied to the spectral data. The data are clipped at $SNR+20$ dB, SNR being the signal-to-noise ratio in the Doppler domain. Note that the SNR clipping reduces the sensitivity of the radar measurements, especially signal of the smaller particles can get lost.

4.4.4. sK_{DP}-RETRIEVAL STEP 4 - CALCULATION $s\Phi_{DP}$

The spectral differential phase, $s\Phi_{DP}$, is the angle of the cross-spectrum sF_{HV} [30]

$$s\Phi_{DP}(r,v) = arg\langle sF_{HV}(r,v)\rangle. \tag{4.3}$$

4.4.5. sK_{DP}-RETRIEVAL STEP 5 - AVERAGE $s\Phi_{DP}$ IN RANGE

The Φ_{DP}-values are noisy. Therefore, the Φ_{DP}-values have to be smoothed along the range direction before use [5, 6, 32]. Before sK_{DP} is calculated, $s\Phi_{DP}$-spectrogram are smoothed along the range direction, because the spectra have been shifted towards 0 m s^{-1}. Fixing a Doppler bin in the spectrogram, a moving average smooths $s\Phi_{DP}$-values along the range domain. A 20 bin moving average is applied (10 bins before and 10 after the selected range bin; no data interpolation). After that the sK_{DP} values are calculated from the $s\Phi_{DP}$ smoothed spectrogram.

4.4.6. sK_{DP}-RETRIEVAL STEP 6 - CALCULATION sK_{DP}

The spectral specific differential phase shift sK_{DP} is retrieved from the spectral differential phase shift $s\Phi_{DP}$ via Equation 4.4.

$$sK_{DP}(r_1,r_2,v) = \frac{s\Phi_{DP}(r_2,v) - s\Phi_{DP}(r_1,v)}{2(r_2-r_1)}. \tag{4.4}$$

where r_1 and r_2 are two consecutive radar range gates, $r_1 < r_2$. The sK_{DP}-values are smoothed as well, first 3 bins in the Doppler domain and than also 3 bins along range (1 bins before and 1 after the selected bin; no data interpolation). This smooths out to noisy spectral bins and, therefore, signatures in the spectrogram can be identified better.

4.4.7. INFLUENCE OF THE $s\Phi_{DP}$ SMOOTHING

This section points out that the smoothing of the $s\Phi_{DP}$-spectrogram causes unwanted signatures in the $s\Phi_{DP}$ and sK_{DP}-spectrogram. Generally, Φ_{DP} is directly related to the propagation of the electromagnetic wave through a medium. Therefore, the $\Phi_{DP}(r)$-value is related to all the propagation effects in the medium that happen till the range r. For precipitating cloud systems, this means that the $s\Phi_{DP}$-signatures of the ice crystals are influenced by the corresponding effects that occur in the melting layer and the rain. As seen in the 5 minutes averaged 20 dB SNR clipped sZ-spectrogram in Figure 4.2 a), the

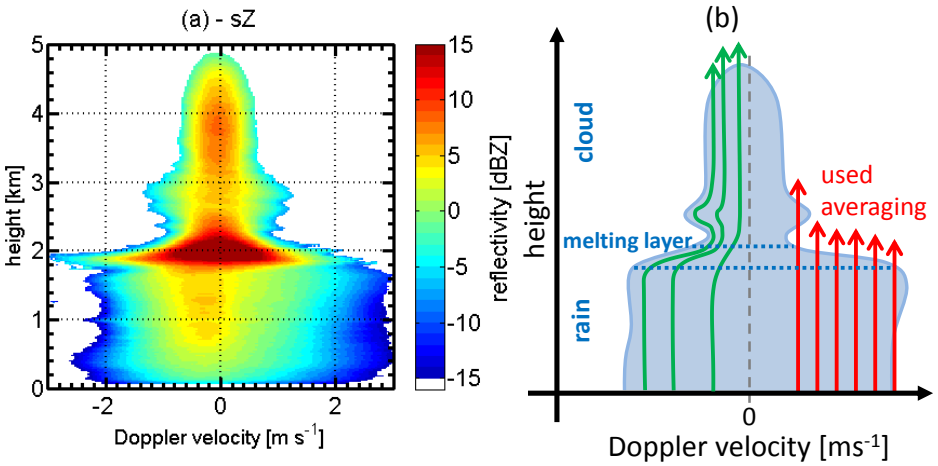

Figure 4.2: (a) shows the whole 5 minutes averaged 20 dB SNR clipped sZ-spectrogram from top to bottom. (b) sketches a $s\Phi_{DP}$-spectrogram for a similar case. The arrows indicate two different smoothing techniques applied to the $s\Phi_{DP}$-spectrogram. In red the used technique is sketched that smoothed the $s\Phi_{DP}$ along a fixed Doppler velocity bin. In green a technique is sketched that proposes to take the spectral broadening in the rain into account.

spectrogram is much wider for rain than for the cloud part. Turbulence might broaden the spectrogram, as seen above the melting layer. The melting process can be identified by the highest Z-values observed and the broadening of the spectrogram at around 2 km. Applying a smoothing along a fixed Doppler bin, as the red arrows in Figure 4.2 b) indicate, misses a lot of melting layer and rain effect that would influence the Φ_{DP}-values in the cloud. Therefore, we assume that applying some size depended averaging as proposed by the green arrows might lower such effects. Especially, at the edges of the spectra where the large and small particles are present. The estimated spectrograms shown in Section 4.6 show such signatures.

4.4.8. USED SETUP TO ESTIMATE sK_{DP}

The estimated sK_{DP}-spectrum is influenced by the chosen setup of smoothing and temporal averaging used in the sK_{DP}-processing algorithm. During the development of the algorithm, several setups are tested. The used setup was found to give the best results for the used data trying to keep the high spatial resolution with the lowest temporal averaging possible. For temporal averaging of less than 3 minutes, no satisfying results could be archived, especially, towards the top of the cloud. These nonsatisfying signatures are observed for several and varying placements of the averaging window. Average the data over a longer time signatures can be identified near the cloud top that are consistent in time. To exclude statistical random errors and artifacts in the processed signatures a 5 minutes average is used. This averaging gives consistent signatures in the sK_{DP}-spectrogram in height and time. Note that at longer temporal averaging the signatures are averaged and smoothed out again. The selected smoothing length and direction for

the $s\Phi_{DP}$ and sK_{DP}-spectrograms are also found by adjusting the settings during the processing. The applied smoothing length was found to give conclusive signatures using a minimum of smoothing.

4.5. CASE STUDY PRESENTATION

Before the estimated spectral parameters are going to be analyzed and discussed, the dataset is introduced. The measurements analyzed are obtained during the ACCEPT campaign, Autumn 2014, Cabauw, The Netherlands. Figure 4.3 shows the fields of reflectivity, differential reflectivity, and differential phase of an overpassing frontal cloud system over the measurement site on 7^{th}, November 2014. In this introduction signatures already give an overview of the microphysical processes that can be expected within in the case study. This information will help below in the further understanding and analysis of the visible signatures in the estimated spectrograms.

Figure 4.3 a) shows the Z-field between 1135 UTC and 1150 UTC. In the selected time frame (black box) the Z-values increase in two steps the first one around 5 km and a slight second increase below 4 km. These increases indicate particle growth at these two regions within the cloud during the selected time frame. In Figure 4.3 b) at 5 km, the maximum values of the Z_{DR}-field are identified. Below the band of maximum values the Z_{DR}-signature decreases. Because the Z-field increases in parallel aggregation of particles is assumed. However, two fall streak like signatures in the Z_{DR}-field indicate that the microphysical conditions during averaging might vary more than expected by only analyzing the Z-field. The observed dynamical conditions during the selected case are stable and homogeneous. The wind fields of TARA (not presented here) depict only one shear in wind direction around 2.7 km. This shear leads to a broadening of the TARA spectra around that height, due to turbulence in the sampling volume. Above, the wind-fields do not show any significant dynamical feature. Figure 4.3 c) depicts the corresponding Φ_{DP}-field. This graph demonstrates how noisy the Φ_{DP}-values are and have to be averaged before they can be used. The black boxes indicate the 5 minutes time frame of averaging.

Although, some variations in the Z and Z_{DR} are visible the cloud is assumed to be homogeneous during the averaging time. Therefore, the estimation algorithm is applied to the presented data set. Note, between 2.2 km and 2 km, in all-time height plots the melting layer can be identified by a band of increased values.

4.6. RESULT: $s\Phi_{DP}$ AND sK_{DP} ESTIMATION

4.6.1. THE ESTIMATED $s\Phi_{DP}$ AND sK_{DP} SPECTROGRAMS

Figure 4.4 a) displays the reflectivity spectrogram, sZ, b) the differential reflectivity spectrogram, sZ_{DR}, c) the spectrogram of the differential phase shift, $s\Phi_{DP}$, and d) displays the spectrogram of the specific differential phase shift, sK_{DP}. All the spectrograms are averaged over 5 minutes and a 20 dB SNR clipping is applied. The dashed line indicates the separation of pristine ice crystals and aggregates. The separation based on a sZ_{DR}-threshold defining spectral bins $sZ_{DR} > 0.6$ dB as pristine ice [10]. The markers C1 to C4 refer signatures of enhanced sK_{DP} identified within the spectrograms. In the following, the sZ and sZ_{DR}-spectrograms are analyzed as well as their signatures related to cloud

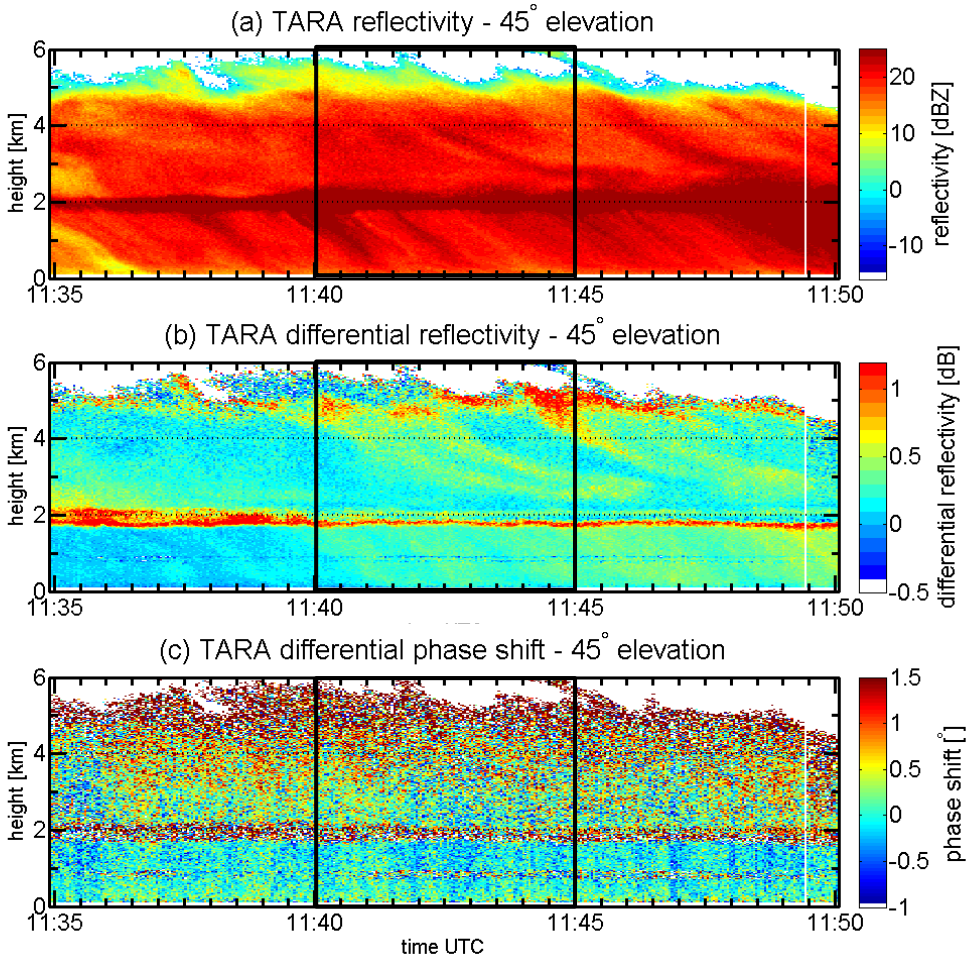

Figure 4.3: shows the measured time-height plots of the measured cloud system from 1135 UTC-1150 UTC, 7^{th} November, 2014. The measurements were performed under 45° elevation. (a) shows the reflectivity field, Z, (b) the differential reflectivity field, Z_{DR}, and (c) the field of the differential phase, Φ_{DP}. The black boxes indicate the 5 minutes time frame the spectral data are averaged.

microphysical processes. Further, the new estimated $s\Phi_{DP}$ and sK_{DP}-spectrograms are described. Although, several signatures are visible in the sK_{DP}-spectrogram. Nevertheless, it was not possible to find distinct relations between the all observed signatures, the theoretical base of K_{DP} (Equation 4.1), and the other observed signatures in sZ and sZ_{DR}-spectrogram. However, the estimated values demonstrate the potential of sK_{DP}-spectra for microphysical process understanding. The presented results are preliminary and further investigations have to be made to relate the sK_{DP}-signatures to the resulting microphysical processes.

The sZ-spectrogram shows a smooth increase of values with a maximum at 3.7 km.

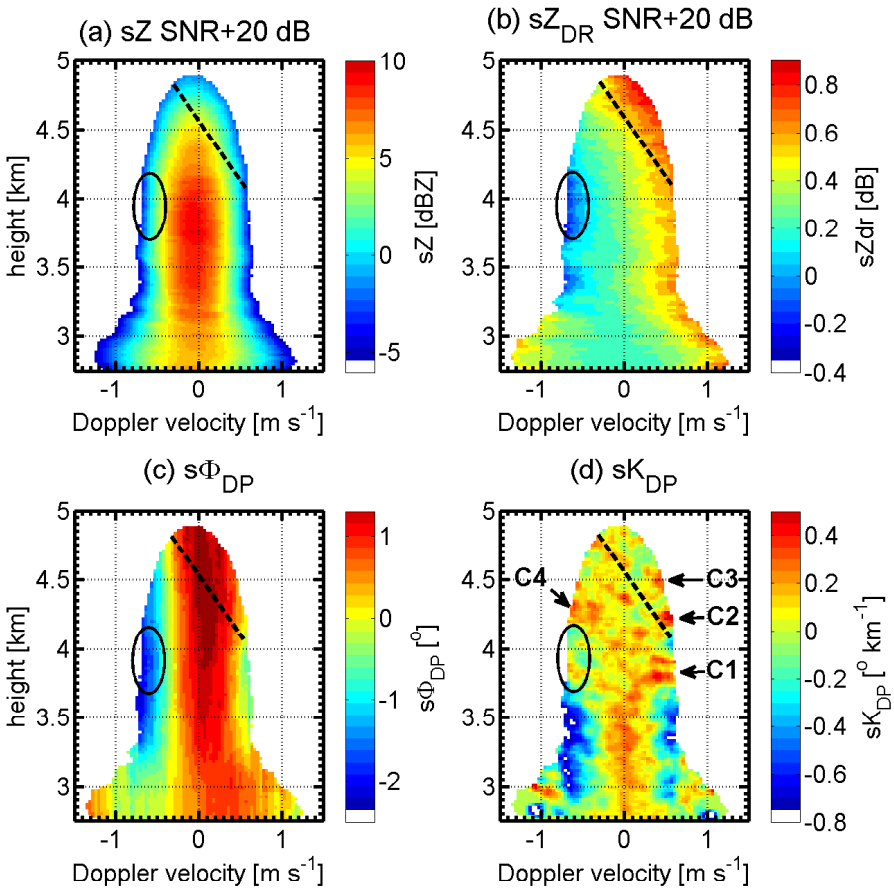

Figure 4.4: (a) shows the reflectivity spectrogram, sZ, and (b) the differential reflectivity spectrogram, sZ_{DR}. (c) shows the differential phase shift spectrogram, $s\Phi_{DP}$, and (d) the corresponding specific differential phase shift spectrogram, sK_{DP}. The dashed line approximates the separation of pristine crystals and aggregates. C1--C4 and the ellipse are markers that highlight signatures discussed in the text. All the shown spectrograms are averaged over 5 minutes and clipped 20 dB above SNR. For $s\Phi_{DP}$ and sK_{DP} also smoothing was applied.

Below 3.1 km, a broadening is observed in the spectrogram corresponding to a shear in wind direction around that height. In Figure 4.5 a) five profiles of spectral reflectivity are presented (-0.6 ms^{-1} (light blue), -0.3 ms^{-1} (blue), 0 ms^{-1} (black), $+0.2$ ms^{-1} (red), and $+0.45$ ms^{-1} (purple)). There is visible that the profiles at -0.3 ms^{-1}, 0 ms^{-1}, and $+0.2$ ms^{-1} from the middle of the spectrogram have similar profile slopes and increase constantly till 3.7 km. This constant increase also indicates a constant particle growth process. Below 3.7 km, in the 0 ms^{-1}-profile a decrease of values is visible. In parallel the two profiles from the spectrogram edges increase, at -0.6 ms^{-1} and $+0.45$ ms^{-1} sZ values increases of about 1 dBZ and 1 dB, respectively. This observation indicates a

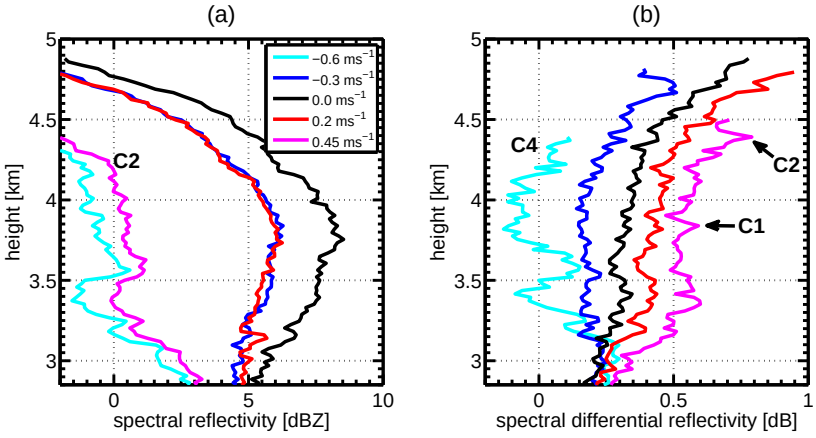

Figure 4.5: shows height profiles for fixed Doppler velocity bins, $-0.6\,\mathrm{ms}^{-1}$ (light blue), $-0.3\,\mathrm{ms}^{-1}$ (dark blue), $0.0\,\mathrm{ms}^{-1}$ (black), $+0.2\,\mathrm{ms}^{-1}$ (red), and $+0.45\,\mathrm{ms}^{-1}$ (magenta), for the spectrograms presented in Figure 4.4. (a) shows the Z-profiles and (b) the Zdr-profiles for the constant Doppler velocities. C1-C4 are markers that are discussed in the text refering to the ones of Figure 4.4.

change in particle growth process, further below the influence of the turbulence region and the related broadening of the spectra is visible. Therefore a clear interpretation in that area is rather complicated.

Figure 4.4 b) shows the corresponding sZ_{DR}-spectrogram. At the top, large sZ_{DR}-values indicate the presence of pristine ice crystals. Using the sZ_{DR}-threshold mentioned above the spectrogram can be separated into pristine crystals and aggregates. This separation is indicated by the dotted line in all the spectrograms. It is seen basically that from top to bottom the sZ_{DR}-values decrease. Although, a particle size shape relation is visible in the sZ_{DR}-spectrogram. Due to the parallel sZ increase this sZ_{DR}-signature indicates the aggregation of particles towards the melting layer. Even negative sZ_{DR}-values are observed (see ellipse in the spectrograms). Such negative sZ_{DR}-values are possible when particles aggregate into prolate oriented aggregates. Nevertheless, the spectrogram also exhibits that smaller particles have higher sZ_{DR}-values than larger ones. These signatures are visible in the spectral differential reflectivity profiles in Figure 4.5 b), too. Especially, the relationship between particle size and shape is presented clearly. The largest sZ_{DR}-values are present for small particles and decrease towards larger particle size (toward lower Doppler velocities). The second visible feature is a change in the profile slopes above 4.25 km, where their values rise faster. Near the top, the more rapid increase of sZ_{DR}-values is observed caused by a higher amount of early aggregates and pristine crystals. The $-0.6\,\mathrm{m\,s}^{-1}$-profile shows that also prolate shaped particles are observed in the volume. These values indicate that the present particle growth process also leads to prolate oriented particles. Because the corresponding sZ-profile shows low values, it can be assumed that the number of prolate oriented aggregates within the observed period is low.

Figure 4.4 c) depicts the differential phase shift spectrogram. As expected from theory, the $s\Phi_{DP}$-values increase with height. Because the further the emitted signal propa-

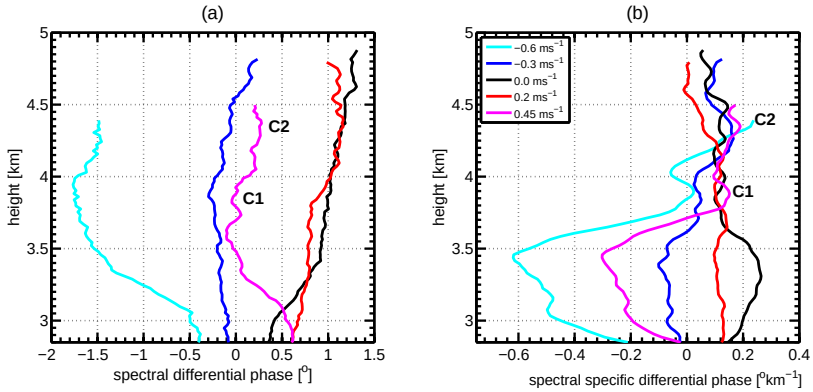

Figure 4.6: shows height profiles for fixed Doppler velocity bins, $-0.6\,\mathrm{ms}^{-1}$ (light blue), $-0.3\,\mathrm{ms}^{-1}$ (dark blue), $0.0\,\mathrm{ms}^{-1}$ (black), $+0.2\,\mathrm{ms}^{-1}$ (red), and $+0.45\,\mathrm{ms}^{-1}$ (magenta), for the spectrograms presented in Figure 4.4. (a) shows the Φ_{DP}-profiles and (b) the K_{DP}-profiles for the constant Doppler velocities. C1-C3 are markers that refer to the ones of Figure 4.4 and discussed in the text.

gates through the cloud system, the larger number of particles with pristine particles or another defined particle shape that cause differences between the phases of the signal and increase the $s\Phi_{\mathrm{DP}}$-values. Nevertheless, the spread of $s\Phi_{\mathrm{DP}}$-values in the Doppler domain is found to be larger than the increase of $s\Phi_{\mathrm{DP}}$ with height exhibiting a range from around 3° at 4 km. Theoretically, such a spread should not be possible. However, the measurements clearly indicate these spread. Especially, at the edges of the $s\Phi_{\mathrm{DP}}$-spectrogram a decrease of values is visible. As discussed already, the edges of the $s\Phi_{\mathrm{DP}}$-spectrogram are influenced by the applied smoothing of the values during the processing as well as from the wind shear and the resulting broadening of the spectrum. Therefore, the visible signatures might be highly influenced by these processes and not only due to the present microphysical processes. Figure 4.6 a) shows $s\Phi_{\mathrm{DP}}$-profiles and illustrates well the visible signatures in the spectrogram and their changes. The $s\Phi_{\mathrm{DP}}$-profiles at the spectral edges, at $-0.6\,\mathrm{m\,s}^{-1}$ and $+0.45\,\mathrm{m\,s}^{-1}$, show decreasing values till 4 km and 3.6 km, respectively. Till 3.6 km the $s\Phi_{\mathrm{DP}}$-signatures at the edges are influenced by the effects of the applied smoothing and turbulence broadening. Above 3.6 km, the $s\Phi_{\mathrm{DP}}$-values agree with the other observed signatures of sZ and sZ_{DR}. The other three profiles show increasing values towards the top as expected in regions where particles with a larger axis ratio are present. Therefore, the $s\Phi_{\mathrm{DP}}$-values in the center of the spectrogram are assumed to be not disturbed by cloud dynamical or processing related issues (related to the smoothing).

In Figure 4.4 d) the specific differential phase spectrogram is presented. Generally, in the sK_{DP}-spectrogram a lot of structures are visible. Note, from the short theoretical discussion under stationary conditions the spectra should not have any slope along the Doppler domain. However, the processed spectrograms show structures that can be divided mainly into two. A consistent and defined structure below 3.75 km and into sK_{DP}-patterns that show more fluctuation above 3.75 km.

Because of the discrepancy between processed and spectra K_{DP} and the current the-

oretical knowledge we do not have any coherent explanation of these signatures. Further research and investigation of $s\Phi_{DP}$ and sK_{DP} are needed. Then it might be possible to relate signatures like the enhanced sK_{DP} originating at C1 and that seams to develop further towards the melting layer or the peaks C2, C3, and C4 in the pattern above the corresponding ice particle microphysical state or changes in processes within the 5 minutes averaging period.

4.6.2. INFLUENCE OF THE $s\Phi_{DP}$-SMOOTHING

The aim of this section is to illustrate that the negative sK_{DP}-signatures in Figure 4.4 d) are caused by the smoothing of the $s\Phi_{DP}$ spectrogram. To avoid such unwanted signatures along the spectral edges a stratiform cloud is selected and analyzed. Therefore, rain or melting layer signatures can be neglected that possibly would influence the smoothing of the spectrogram. Figure 4.7 a) shows the Z-field of a stratiform non-precipitating cloud where no melting layer signatures are present. Figure 4.7 b) to e) show the 5 minutes averaged (1705 UTC - 1710 UTC) 20 dB > SNR clipped sZ, sZ_{DR}, $s\Phi_{DP}$, sK_{DP}-spectrograms of a stratiform cloud case obtained during ACCEPT, 12^{th} October, 2014. The sZ_{DR}-spectrogram depicts high values on top of the spectrogram indicating pristine crystals that start to aggregate. The particle growth is visible clearly below 4 km by the increase of Z-values and a decrease of sZ_{DR}. In Figure 4.7 c) the $s\Phi_{DP}$-spectrogram is depicted. There it is seen that the $s\Phi_{DP}$-values turn negative at the left side of the spectrum. Although, no rain and melting layer are not present in this case the present wind shear at cloud bottom leads to a spectral broadening which has an influences on the $s\Phi_{DP}$-processing above. Similar to the sK_{DP}-spectrogram of the above presented case a variety of structures is present in the sK_{DP}-spectrogram, Figure 4.7 d). However, a clear interpretation of these signatures also cannot be given they differ from the one presented in Figure 4.4.

4.7. DISCUSSION

To achieve a good data quality, the spectral data are averaged. The averaging leads to a mean standard deviation per height bin of $\sigma(s\Phi_{DP}) = 0.17°$ and a mean standard deviation per hight bin for sK_{DP} of $\sigma(sK_{DP}) = 0.185°\text{km}^{-1}$.

To mitigate the saturation in the receiver of the FW-CW radar systems, TARA can automatically adjust its transmit power during heavy rain events. The cases selected in such a way that the averaging is done at stable transmit power, because of the 20 dB SNR-threshold. Also, the cases have to be quite homogeneous regarding microphysics and dynamics in order a meaningful averaging can be done. Due to the used radar frequency, the polarimetric measurements of the cloud part are noisy. Therefore, a 20 dB SNR clipping is necessary to improve the data quality. Because of all these procedures, the number of possible cases to analyze so far is limited.

A point of the discussion is the $s\Phi_{DP}$ and sK_{DP} estimation procedure. As discussed and demonstrated in the text, the presented techniques leave room for improvements. The bullet points give remarks what could be improved.

- The number of cases analyzed is too limited and their number must be increased. Only the analysis of a large amount of data prove the sustainability of the estima-

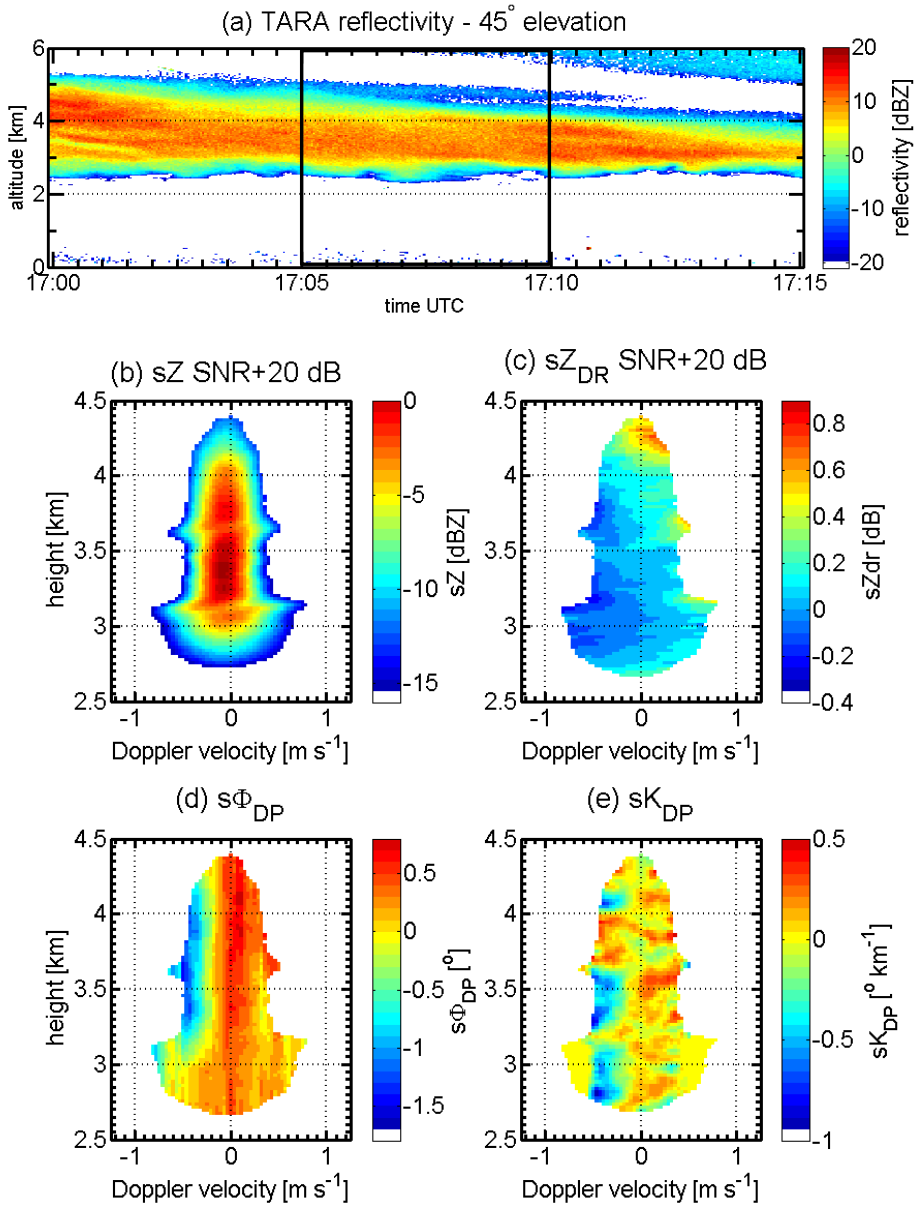

Figure 4.7: shows an stratiform ice cloud case from 12th October 2014. (a) displays the reflectivity field between 1700 UTC to 1715 UTC. (b) shows the sZ, (c) the sZ_{DR} (d) the $s\Phi_{DP}$, and (e) $s\Phi_{DP}$. All the spectral data are averaged 5 minutes (from 1705 UTC to 1710 UTC), are clipped 20 dB above the SNR. $s\Phi_{DP}$ and sK_{DP} are smoothed as mentioned in the text.

tion algorithm. And shows under which cloud dynamical and cloud microphysical conditions reasonable results can be archived.

- The temporal averaging within the estimation procedure has to be reduced and, therefore, the interpretation of the observed sK_{DP}-spectrogram is improved. Especially at the cloud top, the microphysical processes vary a lot in space and time. Therefore, their related microphysical signatures and properties also change and might be smoothed out in when averaging too long. This might be the explanation why no clear signature are identified in sK_{DP}-spectrogram between 5 km and 3.75 km. Nevertheless, shorter temporal averaging would possibly increase the noise in the estimated data and therefore be contra productive. To find the right balance between noise and shorter temporal averaging will be a further challenge on its own.

- The smoothing of $s\Phi_{DP}$ may influence the results, e.g., it averages the enhanced signatures of the melting layer up into the cloud part. Possible signatures and processes related to the melting layer are not discussed in this paper. Also, the figures focus only on the cloud part of the data about 0.5 km above the observed melting layer. At that height, the data are expected to be dominated by cloud processes only. Another critical point is the spectral broadening due to microphysical processes or dynamical influences. In Figure 4.2 a) such a broadening is visible at between 2.5 km and 3.2 km. Therefore, in Figure 4.4 d) the sK_{DP} signatures at the right and left wing of the broadening show a sharp decrease around $v \approx \pm 0.7$ m s^{-1}. This discontinuity is caused by the smoothing of $s\Phi_{DP}$. A smoothing technique taking into account the dynamical broadening would also decrease this effect, similar to the proposed smoothing direction in Figure 4.2 b) (green arrows).

- Last but not least, simulations of the $s\Phi_{DP}$ and sK_{DP} have to be done. Because first steps of further theoretical investigation and simulations done by C. Unal indicate that $s\Phi_{DP}$ and sK_{DP}-signatures are constant over the whole Doppler domain, if the microphysical conditions are constant within the averaging time. They change their value with increasing range depending on the media they propagate through. To see if the observed signatures in the measurements might be caused by such microphysical variations further simulations and theoretical calculations have to be done. Such simulation can help to identify possible spectral signatures that are related to changes in the particle microphysics. Such simulations can help to identify the

Finalizing, the presented estimation algorithm and the corresponding results demonstrate that $s\Phi_{DP}$ and sK_{DP} can be retrieved for S-band radar systems. Nevertheless, to understand the results of the processing and relate the signatures to cloud microphysical processes further investigations are necessary. Currently the knowledge is not sufficient to explain the observed signatures.

4.8. CONCLUSION

In this paper a technique to process spectral differential phase shift, $s\Phi_{DP}$, and specific differential phase shift, sK_{DP}, is presented. The aim is to extend the set of spectral polarimetric radar variables of the profiling S-band radar profiler TARA. The parameters $s\Phi_{DP}$, and sK_{DP} are new parameters that can improve the understanding of ice microphysical processes. So far, K_{DP} and Z_{DR} signatures are used only to analyze and study the onset of aggregation in cloud systems. But K_{DP} is also related to the ice water content present in the measured volume.

Before the calculation of sK_{DP}, the spectral input data are corrected for the horizontal wind influence. They are shifted towards 0 m s^{-1} Doppler velocity before the data are averaged over time. A 20 dB SNR threshold is applied before the $s\Phi_{DP}$ is calculated from the cross-spectra. To estimate sK_{DP} $s\Phi_{DP}$ is smoothed along the range domain. The preliminary results of $s\Phi_{DP}$ and sK_{DP} processing show signatures in the spectrograms and we expect that studying these signatures can help to improve the microphysical process understanding.

REFERENCES

[1] M. D. Shupe, J. S. Daniel, G. de Boer, E. W. Eloranta, P. Kollias, C. N. Long, E. P. Luke, D. D. Turner, and J. Verlinde, *A Focus On Mixed-Phase Clouds,* Bulletin of the American Meteorological Society **89**, 1549 (2008).

[2] A. Myagkov, P. Seifert, U. Wandinger, J. Bühl, and R. Engelmann, *Relationship between temperature and apparent shape of pristine ice crystals derived from polarimetric cloud radar observations during the ACCEPT campaign,* Atmospheric Measurement Techniques **9**, 3739 (2016).

[3] L. Pfitzenmaier, C. M. H. Unal, Y. Dufournet, and H. W. J. Russchenberg, *Observing Ice Particle Growth Along Fall Streaks in Mixed-phase Clouds Using Spectral Polarimetric Radar Data,* Journal of Atmospheric Chenestry and Physics (2017).

[4] P. Kollias, E. E. Clothiaux, M. A. Miller, B. A. Albrecht, G. L. Stephens, and T. P. Ackerman, *Millimeter-Wavelength Radars: New Frontier in Atmospheric Cloud and Precipitation Research,* Bulletin of the American Meteorological Society **88**, 1608 (2007).

[5] V. N. Bringi and V. Chandrasekar, *Polarimetric Doppler Weather Radar, by V. N. Bringi and V. Chandrasekar, pp. 662. ISBN 0521623847. Cambridge, UK: Cambridge University Press, October 2001.* (2001) p. 662.

[6] T. Otto and H. W. J. Russchenberg, *Estimation of Specific Differential Phase and Differential Backscatter Phase From Polarimetric Weather Radar Measurements of Rain,* IEEE Geoscience and Remote Sensing Letters **8**, 988 (2011).

[7] S. E. Giangrande, R. McGraw, and L. Lei, *An Application of Linear Programming to Polarimetric Radar Differential Phase Processing,* Journal of Atmospheric and Oceanic Technology **30**, 1716 (2013).

[8] C. Unal, *High-Resolution Raindrop Size Distribution Retrieval Based on the Doppler Spectrum in the Case of Slant Profiling Radar,* Journal of Atmospheric and Oceanic Technology **32**, 1191 (2015).

[9] D. S. Zrnic and A. V. Ryzhkov, *Observations of insects and birds with a polarimetric radar,* IEEE Transactions on Geoscience and Remote Sensing **36**, 661 (1998).

[10] J. M. Straka, D. S. Zrnic, and A. V. Ryzhkov, *Bulk Hydrometeor Classification and Quantification Using Polarimetric Radar Data: Synthesis of Relations.* Journal of Applied Meteorology **39**, 1341 (2000).

[11] V. Chandrasekar, R. Keränen, S. Lim, and D. Moisseev, *Recent advances in classification of observations from dual polarization weather radars,* Atmospheric Research **119**, 97 (2013).

[12] J. Grazioli, D. Tuia, and A. Berne, *Hydrometeor classification from polarimetric radar measurements: a clustering approach,* Atmospheric Measurement Techniques **8**, 149 (2015).

[13] M. J. Bader, S. A. Clough, and G. P. Cox, *Aircraft and dual polarization radar observations of hydrometeors in light stratiform precipitation,* Quarterly Journal of the Royal Meteorological Society **113**, 491 (1987).

[14] J. Vivekanandan, V. N. Bringi, M. Hagen, and P. Meischner, *Polarimetric radar studies of atmospheric ice particles,* IEEE Transactions on Geoscience and Remote Sensing **32**, 1 (1994).

[15] R. Bechini, L. Baldini, and V. Chandrasekar, *Polarimetric Radar Observations in the Ice Region of Precipitating Clouds at C-Band and X-Band Radar Frequencies,* Journal of Applied Meteorology and Climatology **52**, 1147 (2013).

[16] M. Oue, M. R. Kumjian, Y. Lu, Z. Jiang, E. E. Clothiaux, J. Verlinde, and K. Aydin, *X-Band Polarimetric and Ka-Band Doppler Spectral Radar Observations of a Graupel-Producing Arctic Mixed-Phase Cloud,* Journal of Applied Meteorology and Climatology **54**, 1335 (2015).

[17] M. Oue, M. R. Kumjian, Y. Lu, J. Verlinde, K. Aydin, and E. E. Clothiaux, *Linear Depolarization Ratios of Columnar Ice Crystals in a Deep Precipitating System over the Arctic Observed by Zenith-Pointing Ka-Band Doppler Radar,* Journal of Applied Meteorology and Climatology **54**, 1060 (2015).

[18] J. Grazioli, G. Lloyd, L. Panziera, C. R. Hoyle, P. J. Connolly, J. Henneberger, and A. Berne, *Polarimetric radar and in situ observations of riming and snowfall microphysics during CLACE 2014,* Atmospheric Chemistry & Physics **15**, 13787 (2015).

[19] D. N. Moisseev, S. Lautaportti, J. Tyynela, and S. Lim, *Dual-polarization radar signatures in snowstorms: Role of snowflake aggregation,* Journal of Geophysical Research (Atmospheres) **120**, 12 (2015).

[20] L. Pfitzenmaier, Y. Dufournet, C. M. H. Unal, and H. W. J. Russchenberg, *Retrieving fall streaks within cloud systems using Doppler Radar,* Journal of Atmospheric and Oceanic Technology (2017), 10.1175/JTECH-D-16-0117.1.

[21] J. Vivekanandan, R. Raghavan, and V. N. Bringi, *Polarimetric radar modeling of mixtures of precipitation particles,* IEEE Transactions on Geoscience and Remote Sensing **31**, 1017 (1993).

[22] P. C. Kennedy and S. A. Rutledge, *S-Band Dual-Polarization Radar Observations of Winter Storms,* Journal of Applied Meteorology and Climatology **50**, 844 (2011).

[23] J. Andrić, M. R. Kumjian, D. S. Zrnić, J. M. Straka, and V. M. Melnikov, *Polarimetric Signatures above the Melting Layer in Winter Storms: An Observational and Modeling Study,* Journal of Applied Meteorology and Climatology **52**, 682 (2013).

[24] H. Kalesse, W. Szyrmer, S. Kneifel, P. Kollias, and E. Luke, *Fingerprints of a riming event on cloud radar doppler spectra: observations and modeling,* Atmospheric Chemistry and Physics **16**, 2997 (2016).

[25] A. L. J. Spek, C. M. H. Unal, D. N. Moisseev, H. W. J. Russchenberg, V. Chandrasekar, and Y. Dufournet, *A New Technique to Categorize and Retrieve the Microphysical Properties of Ice Particles above the Melting Layer Using Radar Dual-Polarization Spectral Analysis,* Journal of Atmospheric and Oceanic Technology **25**, 482 (2008).

[26] Y. Dufournet and H. W. J. Russchenberg, *Towards the improvement of cloud microphysical retrievals using simultaneous Doppler and polarimetric radar measurements,* Atmospheric Measurement Techniques **4**, 2163 (2011).

[27] D. Moisseev, C. Unal, H. Russchenberg, and V. Chandrasekar, *Radar observations of snow above the melting layer,* in *Third European Conference on Radar Meteorology (ERAD)* (2004) pp. 407–411.

[28] C. Unal, Y. Dufournet, T. Otto, and H. Russchenberg, *The new real-time measurement capabilities of the profiling TARA radar,* in *Article in monograph or in proceedings* (ERAD 2012 - 7th European conference on radar in meteorology and hydrology, Toulouse, France, 24-29 June 2012, 2012).

[29] J. Bühl, P. Seifert, U. Wandinger, H. Baars, T. Kanitz, J. Schmidt, A. Myagkov, R. Engelmann, A. Skupin, B. Heese, A. Klepel, D. Althausen, and A. Ansmann, *LACROS: the Leipzig Aerosol and Cloud Remote Observations System,* in *Society of Photo-Optical Instrumentation Engineers (SPIE) Conference Series*, Society of Photo-Optical Instrumentation Engineers (SPIE) Conference Series, Vol. 8890 (2013) p. 2.

[30] C. M. H. Unal and D. N. Moisseev, *Combined Doppler and Polarimetric Radar Measurements: Correction for Spectrum Aliasing and Nonsimultaneous Polarimetric Measurements,* Journal of Atmospheric and Oceanic Technology **21**, 443 (2004).

[31] S. P. Rusli, D. P. Donovan, and H. W. J. Russchenberg, *Simultaneous and synergistic profiling of cloud and drizzle properties using ground-based observations,* Atmospheric Measurement Techniques Discussions **2017**, 1 (2017).

[32] A. V. Ryzhkov, D. S. Zrnic, and B. A. Gordon, *Polarimetric Method for Ice Water Content Determination.* Journal of Applied Meteorology **37**, 125 (1998).

5

CONCLUSION AND OUTLOOK

This chapter sums up the findings of the presented work followed by an outlook indicating farther work.

5.1. FALL STREAK RETRIEVAL TO OBSERVE ICE PARTICLE GROWTH USING SPECTRAL RADAR OBSERVATIONS

In *Publication I*, Chapter 2, Pfitzenmaier *et al.* [1] presents an algorithm to retrieve particle fall streaks in a radar time-height-plot. Using this technique, the observation of microphysical cloud processes is improved and the microphysical evolution of a single population of particles falling through the cloud system is studied. The analyzes of the data is based on the assumption that the cloud system is homogeneous in terms of microphysical processes.

The retrieval technique takes advantage of high resolution wind information retrieved by the TARA radar. The wind retrieval is based on the wind profiler capability of the TARA radar which based on the special three-beam configuration of the radar system. Because of this unique configuration of the TARA radar, the developed retrieval does not rely on additional dynamical or wind information and fall streaks can be retrieved during several cloud conditions (stratiform and raining cloud systems). The retrieval allows the rearrangement of radar measurements along the retrieved fall streak. As demonstrated, such rearranged radar Doppler spectra offers a new perspective to analyze radar data qualitatively using a profiling S-band radar.

The fall streak analysis is a useful tool to analyze ice particle microphysical processes in radar data [2, 3]. To run a similar retrieval algorithms for vertical pointing radar systems additional wind information is needed. Therefore, parts of the algorithm presented in Publication I have to be adapted - in particular the dynamic contribution, Equation 2.5, and the implementation of the wind direction. The differences of the temporal resolutions between of the additional wind information and the radar measurements have also to be taken into account. In Equation 2.2, the wind direction is used to project the dynamic information on the line of sight plane. Because of that projection, the wind

is scaled and, therefore, fall streaks can be retrieved in different dynamical conditions. Currently, fall streaks of vertically pointing radar systems are retrieved only for conditions where the wind direction profile is stable [2]. To apply the retrieval algorithm to a vertical profiling radar the changes in wind direction have to be taken into account. One way would be to define also a reference wind direction and scale the other parameters to it. Therefore, further investigation has to be done about defining such a reference wind direction. Equation 2.5, the dynamical contribution has to be adjusted for the use of additional data as well, in particular the turbulence correction, f_{turb}. Because of the empirical relation of that term, more research is needed to find a representation for vertical profiling radar systems.

An example of retrieved fall streaks using vertical pointing radar systems is presented in Figure 5.1. These fall streaks are retrieved using a modified version of Equation 2.5. The fall streaks are retrieved for all three radar systems, based on an 1.5 minute averaged Doppler velocities profiles. The used horizontal wind speed and the wind direction per hight are taken from hourly ECMWF wind-profiles (reanalysis data). To avoid artifacts,

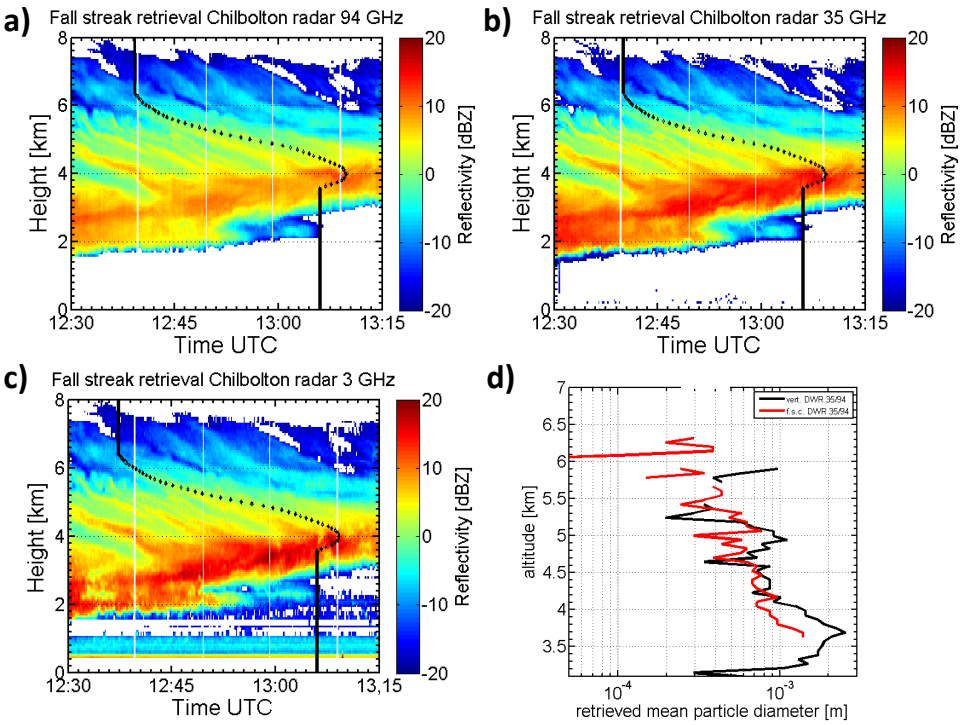

Figure 5.1: a), b), and c) show retrieved fall streaks for the three different vertical pointing radar instruments at Chilbolton, United Kingdom. The three different radar systems work at 94 GHz, 35 GHz, and 3 GHz, respectively. In d) profiles of mean ice particle size are shown following the dual wavelength ration (DWR) approach from [4]. The black profile is base on the vertical DWR profile at 1106 UTC the red one is based on the along the fall streak rearranged DWR profile. (The presented data set was provided during the time as a guest researcher at the University of Reading in 2015).

only cloud parts are analyzed where the wind direction is considered as stable, which means changes of ±12.5° from a chosen mean wind direction in the selected cloud section. To retrieve the fall streaks within that case $f_{\text{turb}} = \frac{vd_z - w_{ecmwf}}{\sigma(vd_z)}$, where w_{ecmwf} is the vertical wind component of the ECMWF profile. The modification factor is more a correction or scaling factor between reanalyzed and the measured vertical velocities than a turbulence correction. Evaluations if the approach to adjust f_{turb} is correct still has to be done. Nevertheless, the example case shows reasonable results for the three different frequencies, Figure 5.1 a) to c). Figure 5.1 d) shows retrieved mean particle size profiles based on the dual-wavelength ratio retrieval technique from [4]. Therefore, the mean particle diameter of ice crystals can be retrieved not only for the vertical profile but also along the fall streak rearranged radar data. A first comparison of the profiles re-arranged along the fall streak show a smoother increase of the particle sizes is visible with decreasing height compared to the vertical profile. Therefore, it is worth to investigate and improve the retrieval technique developed for TARA and apply it to other sensors and data sets. It shows great potential to improve the understanding of microphysical processes in clouds using radar observations.

5.2. ICE PARTICLE GROWTH SIGNATURES IN SPECTRAL POLARIMETRIC RADAR DATA

In the *Manuscript for Publication II*, Chapter 3, Pfitzenmaier *et al.* [3] applied the fall streak retrieval technique of *Publication I* to analyze several ice particle growth processes of a raining cloud system. Different ice particle growth processes can be observed using spectral polarimetric radar data in S-band. Different ice particle growth processes could be distinguished by analyzing the signatures of spectral polarimetric radar measurements.

Using along fall streaks rearranged spectral polarimetric radar data, different regions and ice growth processes are identified. The results obtained by qualitative analyses of spectral polarimetric radar measurements are compared to simulations polarimetric radar data and additional radar measurements. Enhanced growth of ice particles was observed and could be related to the presence of supercooled liquid layer droplets in the cloud system. Additional measurements from radiosondes and a vertical pointing radar system helped to identify regions of supercooled liquid water in the cloud. Furthermore, the enhanced growth of ice crystals increased the rain intensity in the related patterns after the particles melted. Based on the retrieved fall streak signatures, the enhanced ice particle growth can be connected visually to the increase of rain in the radar time-height plot. Thus, the fall streak analysis offers a tool to first analyze the growth of ice particle and later relate them to the corresponding rain patterns.

In the *Manuscript for Publication II* only three cases of enhanced ice particle growth are discussed. In the hour from 1030 UTC to 1130 UTC no fall streak could be retrieved. Because of artifacts in the retrieved wind fields no rearranged data could be analyzed during that period. Nevertheless, the measured radar variables show a large variety in the time-height plots. To analyze these data, the wind retrieval algorithm of the TARA radar has to be improved. Improved dynamical information, especially, the vertical Doppler velocity component, help that fall streaks could be retrieved in such cloud regions.

These would also increase the number of cases the data can be re-arranged along fall streaks and, therefore, increases the possibility for additional retrieval techniques,e.g. hydrometeor classification algorithms, or statistical analysis of data re-arranged along fall streaks. The retrieval technique can also improve the understanding of rain microphysics. For example, the rain drop size distribution along fall streaks can be retrieved using spectral polarimetric radar data [5]. Based on the fall streak technique, differences in the rain drop sizes can be linked to different ice particle processes observed above. The fall streak retrieval has the potential to analyze and understand the whole precipitation formation process, from the top of the cloud system until the corresponding rain drops falls on the ground.

5.3. FURTHER INVESTIGATION OF $s\Phi_{DP}$ AND sK_{DP}

The presented processing technique of Pfitzenmaier *et al.* [6], *Manuscript for Publication III* in Chapter 4, demonstrated, that spectral differential phase, Φ_{DP}, and spectral specific differential phase, K_{DP}, can be processed in S-band. The preprocessing includes the removal of the horizontal wind component from the spectra, the averaging of the spectra in time, a signal-to-noise clipping of the spectral data, and the smoothing of the Φ_{DP} spectrum.By applying all these steps, the spectral specific differential phase shift can be processed. A possible application how spectrally resolved K_{DP} can be used in retrieval techniques is demonstrated in an additional study.

In the *Manuscript for Publication III*, the first processed spectra of Φ_{DP} and K_{DP} are presented. Nevertheless, the processing and the theoretical background has to be improved further. The presented results are based on one analyzed case only. To test the robustness of processing technique another case is shown. Nevertheless, more cases have to be analyzed to identify and confirm characteristic signatures in the processed spectra and relate them to microphysical processes. To do so, the temporal averaging of the spectra has to be decreased to be able to analyze such small scale microphysical processes better. Especially in convective cloud systems conditions change quickly and, therefore, the related microphysical processes. The long averaging diminishes the signatures of such microphysical processes and, consequently, such processes are not recognized in the processed data. The applied smoothing of Φ_{DP} values can change the signatures of the processed K_{DP} values. The smoothing of the Φ_{DP} influences the final processing of the K_{DP} values [7–9]. Nevertheless, based on the simple moving average method, the processed $s\Phi_{DP}$ and sK_{DP} spectrograms show signatures of a possible relation to ice crystal microphysical processes.

One future application can be the retrieval of ice water content (IWC) within the cloud. Several studies have show the potential to retrieve IWC even in S-band [10–12]. Simulations of K_{DP} as a function of the IWC showed better potential for IWC retrievals for higher frequencies. However, high frequency radar systems with full polarimetric capabilities are very rare and, therefore, no attempts for such retrievals reported in literature for higher frequencies. Nevertheless, the results shown in Chapter 4 indicate, not all aspects of the spectral Φ_{DP} and K_{DP} are understood for low frequency radars and further research has to be done to understand the measured signatures.

REFERENCES

[1] L. Pfitzenmaier, Y. Dufournet, C. M. H. Unal, and H. W. J. Russchenberg, *Retrieving fall streaks within cloud systems using Doppler Radar,* Journal of Atmospheric and Oceanic Technology (2017), 10.1175/JTECH-D-16-0117.1.

[2] H. Kalesse, W. Szyrmer, S. Kneifel, P. Kollias, and E. Luke, *Fingerprints of a riming event on cloud radar doppler spectra: observations and modeling,* Atmospheric Chemistry and Physics **16**, 2997 (2016).

[3] L. Pfitzenmaier, C. M. H. Unal, Y. Dufournet, and H. W. J. Russchenberg, *Observing Ice Particle Growth Along Fall Streaks in Mixed-phase Clouds Using Spectral Polarimetric Radar Data,* Journal of Atmospheric Chenestry and Physics (2017).

[4] T. H. M. Stein, C. D. Westbrook, and J. C. Nicol, *Fractal geometry of aggregate snowflakes revealed by triple-wavelength radar measurements,* grl **42**, 176 (2015).

[5] C. Unal, *High-Resolution Raindrop Size Distribution Retrieval Based on the Doppler Spectrum in the Case of Slant Profiling Radar,* Journal of Atmospheric and Oceanic Technology **32**, 1191 (2015).

[6] L. Pfitzenmaier, C. M. H. Unal, Y. Dufournet, and H. W. J. Russchenberg, *Processing of spectral K_{DP} to retrieve ice water content profiles in raining cloud systems,* Journal of Atmospheric and Oceanic Technology (2017).

[7] V. N. Bringi and V. Chandrasekar, *Polarimetric Doppler Weather Radar, by V. N. Bringi and V. Chandrasekar, pp. 662. ISBN 0521623847. Cambridge, UK: Cambridge University Press, October 2001.* (2001) p. 662.

[8] T. Otto and H. W. J. Russchenberg, *Estimation of Specific Differential Phase and Differential Backscatter Phase From Polarimetric Weather Radar Measurements of Rain,* IEEE Geoscience and Remote Sensing Letters **8**, 988 (2011).

[9] S. E. Giangrande, R. McGraw, and L. Lei, *An Application of Linear Programming to Polarimetric Radar Differential Phase Processing,* Journal of Atmospheric and Oceanic Technology **30**, 1716 (2013).

[10] J. Vivekanandan, R. Raghavan, and V. N. Bringi, *Polarimetric radar modeling of mixtures of precipitation particles,* IEEE Transactions on Geoscience and Remote Sensing **31**, 1017 (1993).

[11] J. Vivekanandan, V. N. Bringi, M. Hagen, and P. Meischner, *Polarimetric radar studies of atmospheric ice particles,* IEEE Transactions on Geoscience and Remote Sensing **32**, 1 (1994).

[12] A. V. Ryzhkov, D. S. Zrnic, and B. A. Gordon, *Polarimetric Method for Ice Water Content Determination.* Journal of Applied Meteorology **37**, 125 (1998).

ACKNOWLEDGEMENTS

Buh! I cannot believe that my time as a PhD-student is already over. In the end, all went quicker than I thought. And now I am sitting here at my desk and have to write the hardest few lines of my thesis - the acknowledgments. And I really hope that I have not forgotten someone, even if the name is not listed explicitly.

I would like to thank the ITaRS community. It was a really nice project and I was very happy being a part of it. I enjoyed all the meetings, summer schools, and workshops a lot because they gave me the opportunity to learn a lot and also getting to know other researchers. And so friendships started as well as networking that will hopefully continue in the future. Special thanks for giving us the possibility to realize the ACCEPT campaign in cooperation with the colleagues from TROPOS, the KNMI, and Metek. It was one of the most intensive and fruitful periods within my PhD. Therefore, individual thanks to Yann, Alexander, and Dimitra for your support during the ACCEPT campaign. Second special thanks go to the hosting institutes of my two secondment, my former colleagues from TROPOS and the one from the University of Reading.

I also want to thank all my friends from the PhD-pool for the last five years. For all the fun during the coffee breaks, evenings in bars and all the other thinks. I will miss all of these moments for sure. Thanks to Pedro, to share not only the Desk with me but also the passion for bbq. Thanks to Reenu, for your company in Iceland and where ever we have been. To my favorite French satellite expert Julien. To the Dutch connection Marcel and Thomas from whom I learned that each drop of water contribute to the sea-level rise. And your new simulation and boundary layer measurements experts Steven, Antoon and Jonathan.

Also special thanks to my old school friends, study mates, and friends. I appreciated all your visits, all the time we spent together when I was visiting you as well as all the chats we had on phones. And for all the cheering and support from my family. All your "...du machst das schon!" and "Das wird schon klappen!" helped me a lot - Danke nochmals dafür!

Last but not least, I want to thank the ATMOS group here at TU Delft - Herman, Yann, Christine, Dimitra, Julien, Veronica, Albert, Yiapeng, Stephanie, Tim, Karolina, Igor, Yunlong. It was a pleasure to be part of this group and having coffee breaks together, talking to each other, and do science together. Special thanks go to Herman for giving me the chance to do my PhD in Delft. For the freedom and the support in the planning, and realization of the ACCEPT campaign and the atmospheric project of the GRS field campaign in Iceland. I appreciated all of it and learned a lot! Special thanks also go to Yann! Thanks for all your patience no matter if some fundamental questions at the beginning of my PhD, find and correct typos in my codes or correcting my "texts" (I know that they have been more a pile of letters then sentences. I still remember the moment you saw me struggling for more than a minute trying to write the word "research" correctly). Thanks for all the dinners, lunches and coffee brakes we had. Especially, during the last 2.5 years,

so I could keep you up to date of my work and discuss things (by the way we still have to try out your bbq). The same counts for Christine! Thank you for all your help in my fight against words and sentence construction. For all the proofread you have done and all the advice you gave me. For all the discussions about radar measurements, radar parameters, data processing techniques, and many more things - Thanks a lot!

CURRICULUM VITÆ

Lukas PFITZENMAIER

07-11-1986 Born in Stuttgart, Germany.

EDUCATION

1993–2007 Montessori Schule, Breitbrunn am Ammersee (1993–1997)
Hauptschule an der Heckenstrasse, Olching (1997–1998)
Erasmus Grasser Gymnasium, München (1998–2007)

2007–2010 Bachelor student in Meteorology
University of Leipzig
Thesis: Influence of the planetary boundary layer and air-mass source on atmospheric aerosol particle concentration at the high mountain station BEO-Moussala, Bulgaria
Promotor: Prof. Dr. A. Wiedensohler

2010–2012 Master student in Meteorology
University of Leipzig
Thesis: Determination of microphysical properties of liquid water clouds based on observations with radar, microwave radiometer and lidar
Promotor: Dr. A. Ansmann

2012–2017 PhD. Physics
Delft University of Technology
Thesis: Studying ice particle growth processes in mixed-phase clouds using spectral polarimetric radar measurements
Promotor: Prof. dr. ir. H.W.J. Russchenberg

AWARDS

2015 Outstanding Student Poster Award at the European Geosciences Union, Vienna, Austria, 2015

2014 Best groupe work at the 2^{nd} ITaRS Summer School: "Clouds and Precipitation: Observations and Processes

LIST OF PUBLICATIONS

4. **L. Pfitzenmaier, C.M.H. Unal, Y. Dufournet, and H.W.J. Russchenberg**, *Investigation of spectral phase shift and differential phase shift in S-band,* manuscript for a future submission to a scientific journal.

3. **L. Pfitzenmaier, C.M.H. Unal, Y. Dufournet, and H.W.J. Russchenberg**, *Observing ice particle growth along fall streaks in mixed-phase clouds using spectral polarimetric radar data,* under review in Atmospheric Chemistry and Physics, (2018).

2. **L. Pfitzenmaier, Y. Dufournet, C.M.H. Unal, and H.W.J. Russchenberg**, *Retrieving Fall Streaks within Cloud Systems using Doppler Radar,* Journal of Atmospheric and Ocean Measurement Techniques, Volume 34 No. 4, (2017).

1. **L. Pfitzenmaier, Y. Dufournet, C.M.H. Unal, and H.W.J. Russchenberg**, *Influence of the liquid layer within mixed-phase clouds on radar observations*, Extended Abstract at the 8^{th} European Conference on Radar in Meteorology and Hydrology, Abstract No. 061, (2014).

LIST OF CONFERENCE CONTRIBUTIONS

8. **L. Pfitzenmaier, Y. Dufournet, C.M.H. Unal, and H.W.J. Russchenberg**, *Retrieving fall streaks signatures in radar data to study microphysical changes of particle populations within a mixed phase clouds*, European Geosciences Union, Vienna, Austria, Talk, (2016).

7. **L. Pfitzenmaier, Y. Dufournet, C.M.H. Unal, and H.W.J. Russchenberg**, Poster, *Radar observations of ice particle growth along fall-streaks within mixed-phase clouds*, European Geosciences Union, Vienna, Austria, Poster, (2016).

6. **L. Pfitzenmaier, C.M.H. Unal, Y. Dufournet, and H.W.J. Russchenberg**, *Radar observations of ice particle growth along fall-streaks within mixed-phase clouds*, HD(CP)^2 conference - Understanding clouds and precipitation, Berlin, Germany, Poster (2016).

5. **L. Pfitzenmaier, Y. Dufournet, C.M.H. Unal, and H.W.J. Russchenberg**, *Radar observations of ice particle growth along fall-streaks within mixed-phase clouds*, 37^{th} Conference on Radar Meteorology, Norman, OK, United States of America, Talk, (2015).

4. **L. Pfitzenmaier, Y. Dufournet, C.M.H. Unal, H.W.J. Russchenberg, A. Myaghov, and P. Seifert**, *Effect of cloud microphysics on particle growth under mixed phase conditions*, European Geosciences Union, Vienna, Austria, Poster, (2015).

3. **L. Pfitzenmaier, Y. Dufournet, and H.W.J. Russchenberg**, *Ice particle growth processes within mixed-phase clouds*, TROPOF meeting, Roskilde, Denmark, Talk, (2014)

2. **L. Pfitzenmaier, Y. Dufournet, C.M.H. Unal, and H.W.J. Russchenberg**, Poster, *Influence of the liquid layer within mixed-phase clouds on radar observations*, 8^{th} European Conference on Radar in Meteorology and Hydrology, Garmisch-Parthenkirchen, Germany, Poster, (2014).

1. **L. Pfitzenmaier, Y. Dufournet, and H.W.J. Russchenberg**, *Separation of liquid and ice phase within mixed-phase clouds using combined radar and lidar measurements during HyMex*, 7^{th} HyMex workshop, Cassis, France, Poster, (2013).